Research and Development Technical Report

ECOM 66-G24-F

STUDIES OF EFFECTS OF BOUNDARY MODIFICATION IN PROBLEMS OF SMALL AREA METEOROLOGY

SECOND ANNUAL AND FINAL REPORT 1967-68

By

Heinz H. Lettau, Principal Investigator

Charles R. Stearns, Co-Investigator

April 1969

ECOM
UNITED STATES ARMY ELECTRONICS COMMAND
ATMOSPHERIC SCIENCES LABORATORY
FORT HUACHUCA, ARIZONA
Grant No. DA-AMC-28-043-66-G24
Department of Meteorology
University of Wisconsin, Madison

NOTICES

The citation of trade names and names of manufacturers in this report is not to be construed as official Government endorsement or approval of commercial products or services referenced herein.

The findings of this report are not to be construed as an official Department of Army position unless so designated by other authorized documents.

Destroy this report when it is no longer needed. Do not return it to the originator.

AD

Research and Development Technical Report

ECOM 66-G24-F

STUDIES OF EFFECTS OF BOUNDARY MODIFICATION IN PROBLEMS OF SMALL AREA METEOROLOGY

SECOND ANNUAL AND FINAL REPORT 1967-68

By

Heinz H. Lettau, Principal Investigator

Charles R. Stearns, Co-Investigator

April 1969

ECOM

UNITED STATES ARMY ELECTRONICS COMMAND
ATMOSPHERIC SCIENCES LABORATORY
FORT HUACHUCA, ARIZONA

Grant No. DA-AMC-28-043-66-G24
Department of Meteorology
University of Wisconsin, Madison

400-1.24

Scanner's note:

This page is blank.

TR ECOM 66-G24-F
April 1969

Reports Control Symbol
OSD-1366

STUDIES OF EFFECTS OF BOUNDARY MODIFICATION IN PROBLEMS OF SMALL AREA METEOROLOGY

Final Report

Grant No. DA-AMC-28-043-66-G24
DA Task No. 1T061102B53A-17

Prepared by

Heinz H. Lettau, Principal Investigator

Charles R. Stearns, Co-Investigator

Department of Meteorology, University of Wisconsin

Madison, Wisconsin

For

U.S. Army Electronics Command

Atmospheric Sciences Laboratory

Fort Huachuca, Arizona

Scanner's note:

This page is blank.

TABLE OF CONTENTS

Scanner's note:

This page is blank.

EVAPOTRANSPIRATION CLIMATONOMY
(New approach to numerical prediction of monthly evapotranspiration, runoff, and soil moisture storage)

H. Lettau
University of Wisconsin at Madison

ABSTRACT:

The background and development of a theoretical method to solve the water balance equation for land areas is discussed. A forcing function is considered which is essentially determined by the product of absorbed solar energy multiplied by monthly precipitation; the response function is soil moisture in its month-to-month variations. A very simple parameterization is provided by one nondimensional surface characteristic named the "evaporivity" (which measures the fraction of absorbed insolation utilized during the month in the vaporization of concurrent precipitation) and a characteristic lag-time-interval of the order of 2 to 3 months to express "delayed" evapotranspiration and runoff. The solution is obtained by a closed integration of the water balance equation (rather than employment of regression or correlation methods) and yields a coherent set of data on monthly evapotranspiration, runoff, levels of exchangeable soil moisture, and storage changes. For verification, area averages for the central plains and the eastern region of North America are calculated and compared with several years of actual data analyzed and evaluated by Rasmusson (1968). In spite of simplifying tentative assumptions used in the model calculation, the agreement between predicted and observed data is improved in comparison with results of the earlier prediction methods discussed by Rasmusson (1968).

1. Introductory Remarks

By choosing the term "climatonomy," I want to indicate a study of man's physical environment which is significantly more numerically-theoretically oriented than conventional climatology. Etymologically, a parallel can be drawn to a similar distinction between two other branches of atmospheric science, namely "aeronomy" versus "aerology"; the more recently created term aeronomy implies a physical-mathematical approach to problems of the upper atmosphere in contrast to the more empirical-statistical

methods of conventional aerology. Originally, the word "climatonomy" was coined for my presentation at the 1954 meetings of the American Geophysical Union at Washington, D.C. In his "Review of Climatology 1951-1955" H. Landsberg (1957) recognized the new term. An etymological explanation and a redefinition was recently provided under the title "Shortwave Radiation Climatonomy," by H. and K. Lettau (1969). It was proposed to use the term "climatonomy" if the existing temporal and spatial variations of basic climatic elements, at any planetary surface, are investigated and explained by a mathematical model which is general enough to permit numerical predictions of climate modification and changes. Characteristic of this approach are theoretical solutions in the form of precisely defined "response functions" or "output cycles" as a physical consequence of a mathematically defined "forcing function," or "energy input cycles" into the environmental system. The "impedances" of the two-layer environmental system (including lowest atmosphere and uppermost submedium or soil strata) will be determined by the nature of forced cycles of those physical processes (and their parameterization) which establish the budget requirements of mass, momentum, and energy at the earth/air interface.

For the climate of any planet, the primary forcing function is insolation, given by the composite of the various cycles (annual to diurnal, including higher harmonics) of solar radiation absorbed by the unit area of a region at the earth's surface. The primary response function is the composite of corresponding cycles of local air and ground temperatures. The physical relationship between forcing and response cycles follows from the transformations of absorbed solar energy which generate also the fluxes that constitute the energy balance of the earth/air interface. These fluxes include terrestrial (longwave) radiation, latent energy, and sensible heat, the latter being conducted into both air and submedium.

Longwave radiation and fluxes of sensible heat are relatively straightforwardly coupled with the temperature field on both sides of the earth/air interface; the "partial impedances" contributed by cycles of these fluxes to the total system shall be discussed elsewhere. The previously published "Shortwave Radiation Climatonomy" dealt with a parameterization of the forcing function. The present "Evapotranspiration Climatonomy" is concerned with the indirect coupling between local forcing function and the flux of latent heat in connection with the moisture budget of a continental area. Without precipitation there could be neither soil moisture nor evapotranspiration, nor runoff in stream channels, just as there would be no warmth on a planet without insolation from the central sun. With this philosophy it appears logical to develop evapotranspiration climatonomy under due consideration of the composite of the two coexisting forcing functions, namely: (i) insolation, and (ii) precipitation; or more poetically: "qualities of sunshine and of rain." From the viewpoint of local climate, the two processes can be considered as relatively independent of each

other, both representing external "input," even though from a general circulation viewpoint the two are interdependent. Such interdependency will be incorporated into a more universal climatonomy in a later phase of a continuing development.

With local precipitation as input, and soil moisture variations as output, it is necessary to take into account the two major depleting processes of runoff and evapotranspiration; logically this requires consideration of the conservation equation for mass of water-substance in the local column of subsoil. In the course of climatonomical lines of thought, an apparently novel approach to the classical problem of predicting seasonal trends (by monthly-mean values) of evapotranspiration, runoff and storage was developed. The procedure is explained in the following sections. However, it should be emphasized that the present first communication on this subject is restricted to the discussion of a simplified mathematical model which applies best for relatively large land areas or watersheds, and not for the small scale of the microclimate of a site or a field. Correspondingly, the discussion of relatively short periods (diurnal variations and their harmonics or even day-to-day variations, or the characteristic features of a hydrograph describing case studies of a single precipitation event) is postponed. The present discussion will be restricted to monthly averages representing essentially the annual course of hydro-meteorological processes. The rigorous derivation of a functional relationship between response and forcing function will be taken as establishing the justification for the somewhat arbitrary title: "Evapotranspiration Climatonomy."

2. List of Symbols, and Basic Equations

For conciseness, the notations to be used for establishing the numerical model of evapotranspiration climatonomy will be grouped genetically as follows:

2.1 Physical (universal) constants and parameters

σ = Stefan-Boltzmann constant ($0.822 \cdot 10^{-10}$ ly min^{-1} deg^{-4})

ly = unit of one langley = 1 cal/cm^2

$\mathcal{L}$ = latent heat involved in phase changes of H_2O (for vaporization $\mathcal{L}$ = 597 cal/gram at 273K, linearly decreasing with temperature to 580 cal/gram at 303K; for sublimation, $\mathcal{L}$ = 677 cal/gram)

2.2 Dependent variables of primary importance for climatonomy

T = Kelvin temperatures at and near the ground surface

m = exchangeable moisture contained in a vertical column of soil (mm H_2O, or, alternately, gram H_2O per cm^2) and involved in the hydrologic cycle over land areas

2.3 Nondimensional characteristics of physical surface structure, of importance for climatonomic parameterization

a* = reflectivity (albedo) for shortwave (solar) radiation

ε = emissivity for longwave (terrestrial) radiation

e* = evaporivity due to insolation (see Section 4)

2.4 Energy fluxdensities (ly per unit of time) at ground level

G = global radiation = rate at which direct solar plus diffuse sky radiation is received by a horizontal cm^2 at ground level

a*G = reflected global radiation

$LW\uparrow = \varepsilon\sigma T^4$ = longwave radiation emitted by the ground surface

$LW\downarrow$ = longwave radiation received by the ground, emitted from overlying atmospheric layers (including dust and cloud strata)

$R = (1-a^*)G - LW\uparrow + LW\downarrow$ = net radiation at ground level

Q = vertical flux of sensible heat into the air, originating at ground level

S = vertical flux of sensible heat into the soil, originating at ground level

$\mathcal{L}E$ = vertical flux of latent heat into the air due to phase changes of H_2O substance

2.5 Mass flux densities of water substance (mm H_2O per unit of time)

P = precipitation of atmospheric H_2O intercepted by the ground surface

E = evapotranspiration, or vertical flux of H_2O-vapor into the air, originating at the ground surface (from bare soil and vegetation)

N = runoff, or rate at which water derived from P reaches stream channels and thus is discharged from the land area (watershed) under consideration

2.6 Characteristic ratios or nondimensionals of major importance for numerical modeling in climatonomy

A = Angstroem ratio = quotient of effective longwave radiation to that emitted at ground level

B = Bowen ratio = quotient of fluxes of sensible to latent heat into the air

C = Runoff ratio = quotient of runoff to precipitation

D = Dryness ratio = quotient of net radiation to heat-equivalent ($\mathcal{L}$P) of precipitation

The primary forcing function of planetary climatonomy is given by the cycles of effective shortwave radiation at ground level; that is, the rate at which solar energy (arriving directly along the solar beam as well as indirectly in the form of diffuse light from the sky) can be absorbed by the unit area of ground surface under investigation. This forcing function will be denoted by F(t) since it is a (cyclic) function of time (t); using the notation explained in Section 2.4,

$$F \equiv (1 - a^*)G = F(t). \qquad (1)$$

The problem of climatonomy is basically the following: For given cycles of F(t), what is the response function T(t)? The solution must be obtained with the aid of the surface energy balance equation, which (with the notation explained in 2.4 and using the Angstroem ratio as defined in 2.6) can be formulated as

$$F = A\varepsilon\sigma T^4 + Q + S + \mathcal{L}E. \qquad (2)$$

A first simplifying assumption is that "latent" heat refers only to phase changes of water substance; disregarded are photochemical reactions, such as photosynthesis in the chlorophyll-containing tissue of plants exposed to sunlight. A parameterization of such processes could be achieved but will not need to be discussed here.

The desired solution of equation (2) must express the response function in the form of predictable cycles of T(t). Obviously, only the long-wave radiation term contains explicitly temperature, although not linearly but as T^4. It shall be shown elsewhere that F-generated cycles of the two fluxes of sensible heat—that is to say, Q and S in equation (2)—contain T implicitly and thus can be related to cycles of F(t). The physical connection between T(t) and E(t), however, is relatively complicated. The introduction of the Bowen ratio (B) is helpful only if this B can be independently estimated, either as a constant or, if variable, as a defined function of energy input as well as of thermal response at the lower boundary of the atmosphere. An example for the latter possibility are the conditions at the sea/air interface where there is an unlimited supply of water substance so that the unique-valued dependency of saturation vapor pressure on temperature establishes the necessary link between E and Q in equation (2). A theory for evaporation estimates which utilizes Bowen ratios based on the slope of the saturation-pressure versus temperature curve has been proposed by Bryson and Kuhn (1962). However, for unsaturated land, the employment of the Bowen ratio will be meaningful only in terms of the climatic quasi-constants of annual averages. From month-to-month, also from day-to-day, the actual state of soil surface can fluctuate significantly between extremes of saturation and practically absolute desiccation, and the supply for supporting the evaporative flux in equation (2) must be replenished by precipitation (P). Thus, the Bowen ratio becomes a variable, dependent on preceding precipitation. For the climatonomy of land areas, it is logical that P(t) is taken into account as an additional forcing function while exchangeable soil moisture m(t) assumes the role of a response function in addition to T(t). The problem amounts to simultaneous solutions of equation (2) and the basic balance equation of the mass of water in the soil,

$$P = E + N + dm/dt. \qquad (3)$$

For convenience of writing, dm/dt in equation (3) is used to indicate the partial derivative with respect to time. Also, it must be remembered that m expresses a columnar or vertically integrated value of that part of soil moisture which is exchangeable and actively involved in the hydrologic cycle of the land area under consideration. The simultaneous solution of the two balance equations will be facilitated by the fact that E appears as a common term in (2) and (3).

3. Estimate of Annual Averages of Evapotranspiration and Runoff

Let an annual average be denoted by the overbar. For a continental region with a stable climate it follows that multi-annual means of soil storage terms of both heat and moisture must vanish; that is to say, $\bar{S} = \overline{dm/dt} = 0$. The characteristic ratios defined in 2.6, if formed as quotients of annual means, will be denoted by the asterisk,

$$B^* = \bar{Q}/\mathcal{L}\bar{E}; \qquad C^* = \bar{N}/\bar{P}; \qquad D^* = \bar{R}/\mathcal{L}\bar{P}. \tag{4}$$

The averaged equations (2) and (3), when solved for $\bar{E}$, yield, under consideration of (4):

$$\mathcal{L}\bar{E} = \bar{R} - \bar{Q} = \bar{R}/(1 + B^*), \tag{5}$$

$$\bar{E} = \bar{P} - \bar{N} = (1 - C^*)\bar{P}. \tag{6}$$

The objective is to calculate $\bar{E}$. It may appear paradoxical, but the logical first step is to eliminate $\bar{E}$ in equation (5) with the aid of equation (6), which produces a highly interesting relationship between three nondimensionals,

$$(1 + B^*)\cdot(1 - C^*) = D^*. \tag{7}$$

Equation (7) has general validity in all cases where S in equation (2), as well as dm/dt in equation (3), vanish simultaneously. It may appear noteworthy that equation (7) or an equivalent dimensionless expression has apparently not been considered explicitly in recent texts and monographs; this statement can be confirmed by checking the following list of distinguished references: the textbooks entitled Physical Climatology by Sellers (1965), also by Landsberg (1958); pertinent monographs by Budyko (1958), Gardner (1965), Thornthwaite and Hare (1965), Landsberg (1957), and Linsley (1951). The author would appreciate any information on possible previous uses of this explicit form of equation (7).

Budyko, in his impressively comprehensive study of world climates in energy and moisture balance terms, however, discusses in great detail his and other investigators' successful attempts to establish a semi-empirical relationship between the runoff ratio (C) and the "radiational index of dryness" which is identically the same as the ratio D defined in 2.6. Supported by the analysis of actual precipitation, runoff, and net radiation data from a considerable number of watersheds, several possible but similar interpolation formulas have been suggested. Mathematically simplest and reasonably representative appears to be the following, which is expressed in ratios defined by annual means:

$$C^* = 1 - \tanh D^* \qquad (8)$$

While equation (7) applies without restrictions only if S and dm/dt are sufficiently small, equation (8) cannot be used in climates where, due to possible negative value of the annual mean of net radiation, $D^* < 0$. Namely, C^* cannot exceed the value of unity which it would do in equation (8) for negative D^* because the hyperbolic tangent of a negative argument is negative. However, for all positive D^* (which is the norm and not the exception for world climates), equation (8) satisfies the two natural asymptotic conditions that C^* approaches unity in an extremely humid climate (where $\bar{E}$ would approach zero and D^* will be small due to excessive $\bar{P}$), while C^* approaches zero when D^* becomes large in an extremely arid climate (with $\bar{P}$ small and/or $\bar{R}$ large).

For positive D^* equation (8) can be combined with equation (7) which yields a unique-valued relationship between the three characteristic ratios B^*, C^*, and D^*, as exemplified by the following conjugate sets of triplets:

D^*:	0.00	0.20	0.50	0.70	0.80	0.90	1.00	1.50	2.00	3.00	5.000
C^*:	1.00	0.80	0.54	0.40	0.34	0.28	0.24	0.10	0.04	0.005	0.000
B^*:	0.00	0.01	0.08	0.16	0.20	0.26	0.31	0.66	1.07	2.01	4.000

Given one particular value, for example $C^* = 0.263$, there is no need for an interpolation between the numerical values tabulated, because each conjugate triplet can be calculated (with any desired accuracy) by the combination of the two original equations (7) and (8); in the above example of $C^* = 0.263$, any standard table of hyperbolic functions yields $D^* = 0.945$ whereupon $B^* = 0.282 = (D^* + C^* - 1)/(1 - C^*)$. To produce dimensional results (that is, the values of $\bar{N}$ and $\bar{E}$, in units of mm/month, or inches/year, etc.) it is necessary and sufficient that only one input must be provided in dimensional form (which will most likely be the annual total or mean of precipitation, $\bar{P}$), in addition to one nondimensional input (for example, C^*, but alternately the conjugate value of either B^*, or D^*).

For the special modeling under consideration, the input normally will be the annual averages of the two climatonomical forcing functions which are $\bar{P}$ and $\bar{F}$; or, in other words, the two quantitative measures of annual amounts of rain and sunshine. Such input requires first the estimation of mean net radiation $\bar{R}$. This problem can be solved by determining the annual mean of effective radiation, that is $\bar{F} - \bar{R}$; either by using surface emission of terrestrial radiation and a representative Angstroem ratio, or with the aid of calculation schemes like the Elsasser chart based on representative aerological data. After $\bar{R}$ has been determined, D^* follows from the given $\bar{P}$ whereupon equation (8) produces C^* and hence, $\bar{N}$ and $\bar{E}$. This is readily supplemented by B^* from equation (7) and by

$\bar{Q} = \bar{R}\, B^*/(1 + B^*)$. In summary, if the important relation (7) is valid, the estimate of a coherent set of data on annual evaporation, runoff, and sensible heat flux to the air does not require special parametrization, once a modeling relation like equation (8) has been established. This particular formula is distinguished by the fact that it does not contain any numerical coefficient; however, it appears desirable to test its validity by independent empirical evaluations.

4. Numerical Model for Calculation of Monthly Evapotranspiration, Runoff and Storage

The terms in equation (3) will be considered in physical units of mm(H_2O), per month, which implies that diurnal cycles are averaged out, leaving the annual variation as the main item of interest. As outlined before, the annual cycles of precipitation $P(t)$ and of absorbed insolation $F(t)$ represent the forcing functions, with soil moisture $m(t)$ the response function. A suitable model of climatonomy must express the role of the two depleting processes (evapotranspiration and runoff) as intermediate agents between forcing and response cycles, via water balance requirements.

For the diurnal course of hydro-meteorological processes, and for day-to-day variations between individual precipitation events (local storms), the details of the balance between runoff and infiltration, water retention in the soil, vertical movement of H_2O in the soil and to the plant roots, also percolation and drainage, constitute a highly complicated and sometimes confusing system, with significant feedback involved. A wealth of monographs and books has been published on these subjects; it may suffice here to make reference to the collected articles in Meteorological Monographs, Vol. 6, on "Agricultural Meteorology," published by the American Meteorological Society in 1965, and the large body of literature quoted there. With respect to detail of small-scale and short-period processes, the presently proposed "evapotranspiration climatonomy" may appear oversimplified and will not be a substitute for the special studies reported in the literature. Only within the stated limitations of applicability, and for meso- to-large scale hydro-meteorological processes the new model and its underlying philosophy may be found useful.

Let us assume that two parts contribute to the time series of monthly values of both E and N so that

$$E(t) = E'(t) + E''(t); \quad \text{also} \quad N(t) = N'(t) + N''(t). \qquad (9)$$

The two contributions E' and N' are thought to express a short-term, or a nearly immediate or direct response to the forcing function $P(t)$,

while the contributions E'' and N'' express a delayed response. Physically, this distinction implies that the processes denoted by E'' and N'' involve soil moisture which had been received by precipitation of previous months, while the processes denoted by E' and N' are supplied by concurrent precipitation which just has fallen during the same month. In still another alternate form it can be stated that the lag-time involved in the cycling of soil moisture will be less than one month between P(t) and N'(t), E'(t), but more than one or two months between P(t) and E''(t), N''(t).

First consider monthly means of runoff. Let us assume that delayed runoff (N'') varies in direct proportion to soil moisture (m), or

$$N''(t) = \overline{N''}\, m(t)/\bar{m}, \tag{10}$$

where, as before, the overbar denotes an annual average. Specification of the time series N'(t) offers problems. If there are occasions of saturated soil, or, flash floods in connection with unusually heavy rain fall in the region, it must be expected that N' should be significant. Normally N' will be small for sufficiently large land areas unless a monthly mean P-value exceeds a threshold intensity which will depend on the morphology of the basin. The larger the watershed, the smaller the probability that N' may be significant in comparison with N''. For the purpose of a preliminary study, let us disregard N' in comparison with N''; then N''(t) is practically the same as N(t), or N is given by equation (10).

Next, consider evapotranspiration for which the distinction between immediate (E') and delayed (E'') evapotranspiration has greater significance than for runoff. In analogy to equation (10), we assume for E'' a linear dependency on soil moisture so that

$$E''(t) = \overline{E''}\, m(t)/\bar{m}\,. \tag{11}$$

Summing equations (11) and (10) yields the defining equation for a new characteristic (dimensional) parameter

$$N'' + E'' = (\overline{N''} + \overline{E''})m/\bar{m} = m/t^*, \tag{12}$$

where $t^* = \bar{m}/(\overline{N''} + \overline{E''})$, denotes a characteristic time interval which is most conveniently expressed in units of months. The physical significance of t* follows from its definition which is based on annual mean values; t* can be interpreted as the characteristic "residence time" or "turn-over period" which is determined by the quotient of annual mean of exchangeable soil moisture divided by the sum of the combined annual rates of delayed runoff plus delayed evapotranspiration. This definition

suggests that t^* could be expected to be a time interval between 2 and 3 months.

As stated before, fundamental for climatonomy is the consideration of a precisely defined forcing function. This concept finds a special application for the estimation of "immediate" evapotranspiration $E'(t)$. Namely, let us assume that $E'(t)$ varies in direct proportion to $F.P$, that is the product of the two existing forcing functions, insolation $F(t)$ times precipitation $P(t)$. Physically this implies that without either sunshine or rain, there will be no "direct" evapotranspiration. For dimensional reasons we consider $1/\bar{F}$ as additional multiplier whereupon the model assumption requires the introduction of a new characteristic parameter which we propose to name the "evaporivity" e^* of the land surface considered. It enters as the numerical factor of proportionality in the following defining equation:

$$E'(t) = e^* PF/\bar{F}; \qquad \text{also,} \quad \bar{E'} = (\overline{e^*PF})/\bar{F}. \qquad (13)$$

Note that the above e^* is not the same as the "evaporability" which is a dimensional coefficient introduced by Budyko; reference is made to Thornthwaite and Hare (1965). According to the defining equation (13), the evaporivity e^* is a nondimensional measure of the capacity of land surfaces to utilize a portion of solar energy (absorbed during one month) for the evaporation of precipitation which has been received during the same month (or any other specified time interval). In many respects, e^* can be compared with the albedo of continental regions which like e^* is an empirical quantity. Note that e^* may or may not be independent of time or season. In an elementary manner it can be confirmed that $(\overline{PF})/(\bar{F}).(\bar{P})$ may be larger or smaller, or equal to unity; this fraction exceeds unity in a climate with summer rains, and is smaller than unity in a climate with winter rains. Since without irrigation $\bar{E}$ cannot exceed $\bar{P}$ it follows that evaporivity e^* is an always positive fraction which hardly ever will be closer to unity than about 0.8. Indeed, tentative evaluations have suggested that e^* will normally be between 0.4 and 0.8. Its definition suggests that for a given watershed, the evaporivity e^* should depend on the permeability of the soil, the lushness of vegetation cover, terrain slopes, etc. It will be relatively small for porous soils with "spongy" vegetation, and relatively large on paved or impervious featureless terrain. An example will be discussed in Section 5.

With the aid of the above parameterization, and equations (9) to (13), the basic budget equation (3) transforms into

$$P - E' - N' = E'' + N'' + dm'dt = m/t^* + dm/dt. \qquad (14)$$

After taking the annual average of all terms in equation (14), we subtract this average from the original equation (14), and introduce as a convenient abbreviation the symbol p' for the time series $p' = P - E' - N' - (\overline{P-E'-N'})$; this yields

$$p'(t) = (m - \bar{m})/t^* + d(m - \bar{m})/dt. \qquad (15)$$

Note that $\overline{p'} = 0$, and that the time series $p'(t)$ can be referred to as the reduced version of the "combined" forcing function; it follows from the given values of $P(t)$ and $F(t)$ when e^* is prescribed.

The ordinary differential equation (15) is solved by

$$m - \bar{m} = e^{-t/t^*}[\text{Const} + \int_0^t e^{t/t^*} p' \, dt], \qquad (16)$$

where "Const" indicates the integration constant. Note that for given t^* the integration can be performed numerically using any of the standard schemes; the integration constant is determined by the requirement that the "barred" value (that is, the annual mean) of the right-hand side must vanish for a stable climate. Equation (16) characterizes in an exemplary manner the philosophy of climatonomy; namely, a response function $m(t)$ is related to a precisely defined forcing function $p'(t)$, with the aid of a unique-valued equation under employment of mathematically prescribed parameters (in this case e^* and t^*).

The practical verification of the scheme of "soil moisture climatonomy" requires the following sequence of steps:

(i) Given $\bar{P}$, calculate annual averages $\bar{E}$ and $\bar{N}$ using procedures outlined in Section 3.

(ii) Assume numerical values for the evaporivity of the watershed under consideration; then, given F and P, calculate monthly values of $e^*PF/\bar{F} = E'$ (according to equation (13)), and obtain the annual mean $\overline{E'}$, whereupon $\overline{E''}$ follows as $\bar{E} - \overline{E'}$.

(iii) Either assume $N' = 0$ (hence, $\overline{N'} = 0$, as in the following example of application), or specify numerically which fraction of P (during months of maximum rainfall) can substitute an "immediate" runoff. This step must result in the annual average of N'' which tentatively is taken to equal $\bar{N}$ as derived in step (i).

(iv) Assume a numerical value for the soil moisture residence-time t^* and obtain the annual average $\bar{m}$ as $t^*.(\overline{E''} + \overline{N''})$, using equation (12).

(v) On the basis of monthly values for E'—as employed in step (ii)—and estimates of N'—as would follow from step (iii)—obtain the reduced forcing function, that is, the time-series p' in the form of monthly values of $P - E' - N' - \overline{(P-E'-N')}$, and perform numerically the integration prescribed by equation (16); then, establish the integration constant whereupon the time-series $m(t)$ is obtained with the aid of $\bar{m}$ as derived in step (iv).

(vi) Calculate the time-series dm/dt by subtracting (for each month) the value of m/t^* from $P - E' - N'$, or, alternately, subtract $(m-\bar{m})/t^*$ from p'.

(vii) Calculate the time-series of N'' and E'' with the aid of equations (10) and (11), using soil moisture m from the result of step (v) and the averages determined in steps (ii) and (iii).

(viii) Calculate the time-series E and N by adding E'' from step (vii) to E' from step (ii), and N' (if different from zero) to N'' from step (vii).

(ix) Finally, as a check, add the calculated monthly values of dm/dt, E and N together and compare the result with the original time-series $P(t)$. Agreement should be within tolerable rounding-off errors, in view of the basic balance equation (3).

5. Example of Application

As stated repeatedly, the model of evapotranspiration climatonomy, and the calculation of monthly-mean waterbalance terms will produce best results when applied to a continental region of sufficiently large extent. For the testing of calculations, it is desirable that for such an area the two forcing functions $P(t)$ and $F(t)$ are known, and observational data of all terms of the water balance (that is, monthly means of runoff, evapotranspiration, and storage) are independently available, to be compared with the calculated set of coherent time series of N, E and m. With respect to data availability and size of the continental area, the work by Rasmusson (1968) appears outstanding; this includes complete time series of monthly water balance terms averaged over several years for the central plains and eastern regions of North America; the area amounts to 64.10^5 km^2 and includes the watersheds of the Mississippi and St. Lawrence. Rasmusson's data are furthermore distinguished by the feature that monthly evapotranspiration has been evaluated as the vertically integrated divergence of atmospheric vapor transport by large scale air currents, utilizing the relative dense network of radiosonde stations of the region.

Monthly means of the forcing functions are summarized in Table 1. The precipitation values are taken from Table 4 in Rasmusson (1968), after being rounded off to the nearest mm/month. Global radiation for the region (G, ly/day) was estimated independently as a representative area-average, based on selected stations from the report by Löf, Duffie, and Smith (1966); this G-evaluation was performed by Mr. Linde and Mr. Ronberg, both graduate students at the Meteorology Department at Madison, Wisconsin. Albedo values for Rasmusson's region were estimated under consideration of seasonal snow cover conditions and the phenological cycle, essentially based on sample data provided for North America by Kung, Bryson and Lenschow (1964). The last two lines of Table 1 contain the results of straightforward calculations on the basis of the foregoing data.

Table 1. Central Plains and Eastern Region of North America. Monthly values and representative annual average of: Forcing function of precipitation (P, mm/mo); Global radiation (G, ly/day); Estimated surface albedo (a*, fraction); Solar forcing function (F = (1-a*).G, ly/day); Combined forcing function ($PF/\bar{F}$, mm/mo).

	Jan	Feb	Mar	Apr	May	Jun	Jul	Aug	Sep	Oct	Nov	Dec	Annual Mean
P	40	46	55	56	79	87	91	72	73	56	47	45	62
G	187	265	371	466	543	595	589	517	423	312	210	167	398
a*	.24	.28	.21	.19	.18	.17	.17	.17	.18	.19	.20	.22	.20
F	142	191	293	377	445	494	489	429	347	253	168	130	313
$PF/\bar{F}$	18	28	52	68	112	137	142	99	81	45	25	19	69

As the basis for comparison or testing of the model calculations, monthly means of observed water balance terms of the considered region according to Rasmusson (1968, Table 4) are summarized in Table 2. All values of evapotranspiration (E), runoff (N), soil moisture-storing (dm/dt), and soil moisture (m) were rounded off to the nearest mm/month or mm, and very slightly adjusted so that the sum of the first three lines in Table 2 equals the first line (P-values) in Table 1, in agreement with the balance equation (3). The fourth line of Table 2 represents a smooth time-series (dm/dt) obtained as a three-value-running mean of the original dm/dt data.

Table 2. Central Plains and Eastern Region of North America. Observed data after Rasmusson (1968) which constitute the water balance representative of the region. Monthly values and annual average of: Evapotranspiration (E, mm/mo); Runoff (N, mm/mo); Soil moisture storing (dm/dt, mm/mo); Smooth time-series of soil moisture storing ((dm/dt), mm/mo); Soil moisture (in mm H_2O) relative to an arbitrary reference level ($m - m_{Aug}$) where m_{Aug} is the undetermined minimum value occurring in August.

	Jan	Feb	Mar	Apr	May	Jun	Jul	Aug	Sep	Oct	Nov	Dec	Annual Mean
E :	23	12	25	40	63	80	93	73	50	40	29	22	46
N :	16	17	25	26	23	16	14	13	10	11	11	15	16
dm/dt :	1	17	5	-10	-7	-9	-16	-14	13	5	7	8	0
(dm/dt):	8	8	4	-4	-9	-11	-13	-8	1	8	7	5	0
$m-m_{Aug}$:	35	52	57	46	40	30	14	0	13	18	25	33	30

In a practical application of the concepts and developments of climatonomy, let us follow the steps outlined at the end of Section 4. In step (i), consider that for the region $\bar{P} = 62$ mm/month, according to Table 1. Among the various choices of supplementing this information on annual mean forcing function value, let us assume for brevity that the annual mean of stream discharge $\bar{N} = 16$ mm/month (from Table 2) is also known. Hence, the runoff ratio for the area equals $C^* = 16/62 = 0.26$, and with this information the empirical Budyko formula (8) yields a dryness ratio of $D^* = 0.96$ (since $\tanh 0.96 = 0.74 = 1 - 0.26$), whereupon the generally valid relation (7) results in a Bowen ratio $B^* = 0.30$ for the climate of this region. Knowing the set of ratios (B, C, D), a simple dimensional annual mean (such as $\bar{P} = 62$ mm/month, $\mathcal{L}\bar{P} = 117$ cal/day) yields the remainder of annual mean energy budget constituents: namely, net radiation as $\bar{R} = D^*\mathcal{L}\bar{P} = 112$ ly/day, flux of sensible heat into the air $\bar{Q} = B^*\bar{R}/(1+B^*) = 26$ ly/day, and heat equivalent of annual mean evaporation $\bar{R} - \bar{Q} = 86$ ly/day. The possible comparison of calculated values of $\bar{R}, \bar{Q}, \bar{E}$ with independently determined data for the region would permit us to test the validity of equation (8); this test will be outside the scope of our tentative study, and shall be performed elsewhere.

For step (ii), let us assume that the evaporivity of the region is uniform throughout the year and equals $e^* = 0.637$. Hence, with $(\overline{PF})/\bar{F} = 69$ mm/month (according to Table 1) it follows that the average "immediate" evapotranspiration has an annual average of $\bar{E}' = 44$ mm/month; for the above $\bar{E} = \bar{P} - \bar{N} = 46$ mm/month, only 2 mm/month remain for the annual average of delayed evapotranspiration $\bar{E}''$.

In step (iii), let us assume that for this continent-wide region, all runoff is of the "delayed" type. Hence, $N' = 0$ and the annual average $\overline{N''} = \overline{N} = 16$ mm/month, according to developments in step (i).

For step (iv), let us postulate that the characteristic residence time interval of soil moisture for the region equals $t^* = 3.0$ months. Consequently, with the sum of the annual averages of delayed processes $\overline{E''} + \overline{N''} = 2 + 16 = 18$ mm/month, the annual mean of exchangeable soil moisture of the region follows as $\overline{m} = 3.0 \times 18 = 54$ mm, or slightly more than two inches of water substance. The actual reservoir of groundwater is, of course, much deeper since by definition m includes only its exchanged portion.

Steps (i) to (iv) have involved primarily the calculation of annual averages, of energy and water budget constituents of the region. With the following steps we evaluate the time-series in the form of one set of values for each of the 12 months. Step (v) deals with the time-series E' (which for a month-to-month variation of e^* would have had to be calculated already in step (ii)), and with E' and P (and possibly N') the time-series p' is obtained. Results of these two calculations are summarized in the first two lines of Table 3. Then, the integration required in equation (16) is performed, which yields the time-series of $m - \overline{m}$, hence $(m - \overline{m})/t^*$, and also that of exchangeable soil moisture m; see lines three to five of Table 3. For this special example, the integration constant in equation (16) was determined to equal 16 mm H_2O.

Step (vi) is the calculation of the time-series dm/dt. Rather than approximating this partial derivative by finite differences of the time series m(t), we consider the balance equation (15) and obtain dm/dt for each month as p' minus $(m - \overline{m})/t^*$, that is the difference between lines two and five in Table 3. Values listed in the sixth line of Table 3 were calculated in this manner.

Employing values obtained in the first six steps, the following steps (vii) to (ix) yield in the straightforward manner outlined at the end of Section 4 the time-series of delayed runoff (N", which equals N for the special case that $N' = 0$), delayed evapotranspiration (E"), hence predicted evapotranspiration E as the sum $E' + E''$, and finally $N + E + dm/dt$, which is a "check-line" because it should agree (within tolerable rounding off errors of $\pm$ 1 mm/month) with the time series of precipitation (P) listed in Table 1. In summary, Table 3 contains all calculated results, that is the "output" derived with the aid of the model of climatonomy. Table 1 is a documentation of the forcing functions, that is, the "input"; Table 2, however, contains exclusively the results derived independently by Rasmusson (1968), that is, a complete set of observed data which can be used to test the results of the calculations.

Table 3. Results from Model of Evapotranspiration Climatonomy. Calculated monthly data (employing forcing functions and parameters for the central plains and eastern region of North America) of: "direct" evapotranspiration (E', mm/mo); reduced forcing function (p', mm/mo); exchangeable soil moisture (m, also its departure from annual average, $m-\bar{m})/t^*$, mm/mo); rate of soil moisture storing (dm/dt, mm/mo); runoff (N, mm/mo); delayed evapotranspiration (E'', mm/mo); evapotranspiration ($E = E' + E''$, mm/mo); sum of $E + N + dm/dt$ (mm/mo) as "checkline."

	Jan	Feb	Mar	Apr	May	Jun	Jul	Aug	Sep	Oct	Nov	Dec	Annual Mean
E'	12	18	33	43	71	87	90	63	52	29	16	12	44
p'	10	10	4	-5	-10	-18	-17	-9	3	9	13	15	0
$m-\bar{m}$	16	20	21	13	3	-11	-23	-27	-21	-9	3	14	0
m	70	74	75	67	57	43	31	27	33	45	57	68	54
$(m-\bar{m})/t^*$	5	7	7	4	1	-4	-8	-9	-7	-3	1	5	0
dm/dt	5	3	-3	-9	-11	-14	-9	0	10	12	12	10	0
N	21	22	22	20	17	13	9	8	10	13	17	20	16
E''	2	3	3	2	2	2	1	1	1	2	2	2	2
E	14	21	36	45	73	89	91	64	53	31	18	14	46
E+N+dm/dt	40	46	55	56	79	88	91	72	73	56	47	44	62

6. Critique, and Plans for Future Work

The set of data calculated with the model of climatonomy and summarized in Table 3 represents a first quantitative solution of the hydrologic balance, with a complete and simultaneous consideration of all terms of equation (3). Calculated are coherent sets of monthly means of area averages of evaporation E, runoff N, exchangeable soil moisture m, and monthly addition or removal from storage, dm/dt. The calculation is based on area averages of two forcing functions, precipitation P and absorbed solar energy F. The fact that all water balance terms are area averages for natural drainage boundaries (that is, river basins or watersheds) is fundamental to hydrology. Rasmusson analysed results (see Table 2) inviting a test by a comparison between corresponding quantities in Table 2 and Table 3. For a visual comparison it is self-suggestive to enter the calculated results from Table 3 into the various illustrations published by Rasmusson (1968), since these graphs contain already comparisons based on the evaluation of formulas and computation schemes proposed earlier by Budyko and also by Thornthwaite. By and large it will be found that the new results of "evapotranspiration climatonomy" appear to simulate relatively closely Rasmusson's curves. The agreement between observed and calculated time-series of the primary "response function" of soil moisture m(t), and also of

the dominating depletion process of evapotranspiration E(t), becomes even more satisfactory if the calculated E and m series are plotted with 1/2 month lagging relative to the observed time-series. This could indicate, along the lines of the discussion of immediate versus delayed processes in connection with equations (9), that the lag between $E^{I}(t)$ and the combined forcing function (P.F) is relatively small but finite, and not really equal to zero. A suggested lagtime of 1/2 month appears to be appropriate for the "quasi-immediate" processes. No changes in the concept of delayed processes, with a lagtime equal to the parameter t*, or 2.5 to 3 months, is necessary.

Incidentally, it should be mentioned that the particular choice of the pair of parameters (that is, t* = 3.0 months and e* = 0.637) was based on a preliminary analysis of Rasmusson's empirical data, in the light of climatonomic model concepts. This analysis showed that the model is not very sensitive to t*, where a variability of $\pm$ 20% can be tolerated; for e* a variability within about $\pm$ 5% seems to be insignificant. Conditions will be different for other watersheds. The surface characteristic e* will have to be evaluated for other river basins, where the water-balance is known, until a systematic classification according to morphology, soil structure and permeability, vegetation cover, freeze duration, etc., can be made. This procedure will yield classified listings of evaporivity data, comparable to tables presently available, and in general use, for surface reflectivity and emissivity of typical land surfaces. The present employment of a time-independent e*-value must also be considered as a tentative approximation. In reality, evaporivity at a locality will vary with snow cover, occurrence of partly frozen ground, and the phenological cycle of the growing season, etc. It should be remembered that surface albedo (see a* in Table 1) in temperate climates also has a significant annual course, and is nevertheless a useful and important surface parameter.

In the calculated annual course of soil moisture for the central plains and the eastern regions of North America, the maximum value in early spring as well as the minimum value in late summer appear to be quite realistically produced. The fact that calculated evaporation has nearly the opposite phase as soil moisture illustrates strikingly the dominating effect of "quasi-immediate" evapotranspiration E^{I}; the data also suggest that the efficiency of the process E^{I} is such that most of the rain water is recycled to the atmosphere within about two weeks. This, of course, is also evident from the ratio of annual averages, $\overline{E^{II}}/\overline{E^{I}} = 2/44$, while, naturally, the opposite is true for N'' and N^{I}, with N'' dominating. Since N^{I} is near to zero for the considered watershed, the calculated N parallels the time-series of m(t); the observed data in Table 2 show, indeed, that the maxima coincide, while the minimum value of N lags by one month that of the observed m-curve.

With respect to the "delayed" processes E" and N", proportionalities of the type of equations (10) and (11) are conventional in hydrology; usually, the restriction is imposed that the proportionality becomes invalid once the soil moisture approaches a state of saturation. This fact was not considered here but could be incorporated relatively easily. In this respect, likewise concerning the incorporation of month-to-month variations of evaporivity, the model of evapotranspiration climatonomy is rather flexible. Refinements will certainly be added in future applications and studies. At the present time, investigations are in progress on climatic data from regions where there are pronounced rainy seasons alternating with many months of dryness, including climates of the mediterraneantype (rainy winters) and of the monsoon character (rainy summer). Obviously, there will be significant differences in the cycle of the combined forcing function P.F for these two climates. As indicated in the introduction, the concept of climatonomy is rather broad and not restricted to a special model for the explanation of seasonal soil moisture trends in response to annual forcing cycles represented by the combined action of rain and sunshine. With the knowledge of how to deal basically with the annual variation of the water balance on a continental region, a new road is opened which will lead to a more representative climatonomic model including seasonal temperature trends. Progress in this direction has already been made, and shall be reported in due time. Apart from the problem of developing climatonomy in general, it can be hoped that the special model of evapotranspiration climatonomy may prove useful for the practical solution of presently existing shortcomings concerning the parameterization of air-land interaction, for numerical modeling of the general circulation of the atmosphere.

REFERENCES

Bryson, R. A., and P. M. Kuhn: "Some Regional Heat Budget Values for Northern Canada," Geographical Bulletin, No. 17, pp. 57-60, 1962.

Budyko, M. I.: "Translated Title: "The Heat Balance of the Earth's Surface," Translated by N. Stepanova, 259 pages, U.S. Weather Bureau, Washington, D.C., 1958.

Gardner, W. E.: "Rainfall, Runoff, and Return," Meteorol. Monographs, American Met. Soc., Vol. 6, No. 28, pp. 138-148, Boston, Mass., 1965.

Kung, E.C., R. A. Bryson, and D. H. Lenschow: "Study of Continental Surface Albedo on the Basis of Flight Measurements...over North America," Monthly Weather Review, Vol. 92, No. 12, pp. 543-546, 1964.

Landsberg, H. E.: "Review of Climatology 1951-1955," Meteorol. Monographs, Amer. Met. Soc., Vol. 3, No. 12, Boston, Mass., 1957.

Landsberg, H. E.: "Physical Climatology," 270 pp., Gray Printing Co., Inc., DuBois, Pa., 1958.

H. and K. Lettau: "Shortwave Radiation Climatonomy," Tellus, Vol. 21, pp. 1-15, 1969.

Linsley, R. K.: "The Hydrologic Cycle and its Relation to Meteorology," Compendium of Meteorology, Amer. Met. Soc., pp. 1048-1054, Boston, Mass., 1951.

Löf, G. O., J. A. Duffie, and C. O. Smith: "World Distribution of Solar Radiation," Univ. of Wisconsin Engineer. Exp. Sta., Solar Energy Lab., Report No. 21, Madison, Wis., 1966.

Rasmusson, E. M.: "Atmospheric Water Vapor Transport and the Water-balance of North America," Monthly Weather Review, Vol. 96, pp. 720-734, Washington, D.C., 1968.

Sellers, W.D.: Physical Climatology, 273 pp., Univ. of Chicago Press, Chicago, Ill., 1965.

Thornthwaite, C. W., and F. K. Hare: "The Loss of Water to the Air," Meteorol. Monographs, Amer. Met. Soc., Vol. 6, No. 28, pp. 163-180, 1965.

ESTIMATES OF VORTICITY, DIVERGENCE, AND VERTICAL VELOCITY IN A SURFACE LAYER*

G. L. Frederick, Jr.
Department of Meteorology
University of Wisconsin at Madison

ABSTRACT

The vertical relative vorticity, horizontal divergence, and resulting vertical velocity are estimated from data accumulated at Davis, California in the spring of 1967. Half-hour mean values of these quantities are determined at nine levels between the surface and 320 cm from wind information collected by a cup anemometer-wind vane system. The cups and vanes were mounted on three masts erected 100 m apart at the vertices of an equilateral triangle.

A detailed theoretical development of Gauss' Divergence Theorem and Stokes' Theorem leads to the Bellamy-Bennett computation technique. Primary results show that the horizontal divergence computed are not necessarily small in the surface layer as is often assumed for a micrometeorological site in flat surroundings.

1. Introduction

1.1 Purpose

Values of vorticity, divergence and vertical velocity are important terms to the meteorologist. Information about the average values of these terms is also of interest to the observing micrometeorologist, especially in the "surface layer" at a given site. It is most often assumed that these terms are negligible and few until now have even attempted to measure them. It is the purpose of this study to examine

*Part of this work was submitted to the University of Wisconsin in partial fulfillment of the requirements for the degree of Master of Science, with Professor C. Stearns as thesis advisor.

the results of an effort to measure these quantities on the micro-mesoscale in the "surface layer" over a carefully selected micrometeorological site. Unless otherwise specified in this paper the term divergence refers to the horizontal divergence of wind velocity, $\frac{\partial u}{\partial x} + \frac{\partial v}{\partial y}$, and vorticity will mean $\frac{\partial v}{\partial x} - \frac{\partial u}{\partial y}$, the relative horizontal vorticity about a vertical axis.

1.2 Site description and instrument layout

In the spring of 1967, under the sponsorship of the U.S. Army Electronics Command, Atmospheric Sciences Laboratory, Ft. Huachuca, Arizona, teams of researchers gathered together for the Cooperative Field Experiment at Davis, California. A group from the Department of Meteorology, University of Wisconsin participated in collecting micrometeorological profile data from 26 April to 5 May. It is with this data that the author made his calculations, although he did not personally participate in the experiment. A detailed description of the instrumentation, data collection techniques and data collected was done by Stearns and Dabberdt (1968). The objectives of the field experiment were to measure independently by several different systems the fluxes of momentum, sensible heat, and latent heat in the surface layer. Data was to be collected over several weeks of concentrated activity and a comparison of results between the systems was to be made.

The general layout of the measuring devices associated with this study is shown in Fig. 1.1. Masts 1, 2 and 3 lie at the vertices of an equilateral triangle whose sides are 100 m in length. The masts were 4 m high and supported vertical arrays of Thornthwaite cup anemometers (at levels 20, 40, 80, 120, 160, 200, 240, 280 and 320 cm from the ground) and wind direction vanes (at 40, 80, 160, 240 and 320 cm from April 26 to 28 and at 80, 160, 200, 240 and 320 cm from May 2 to 5) mounted on cross bars. The distance between vane and anemometer on each level was one meter and the cross bar was projected one meter from the mast. The masts were made of two inch aluminum pipe, supported on a base by four guy wires at the top, and could be rotated so that the sensors were generally directed into the wind. It was hoped that the construction would minimize the influence of the supporting structure on the wind measurements (Dabberdt, 1968).

Figure 1.2 shows the character of the surface in the region surrounding the experimental site. In the area enclosed by the three masts the surface was covered by fescue grass. A theodolite survey of the terrain showed that mast 2 was 8 cm higher than mast 1 and mast 3 was 28 cm higher than mast 1. If these measurements are characteristic of the field in general, the terrain slopes by 20 cm per 100 m from south to north. The possible effect of this slope will be discussed in section 3.4.

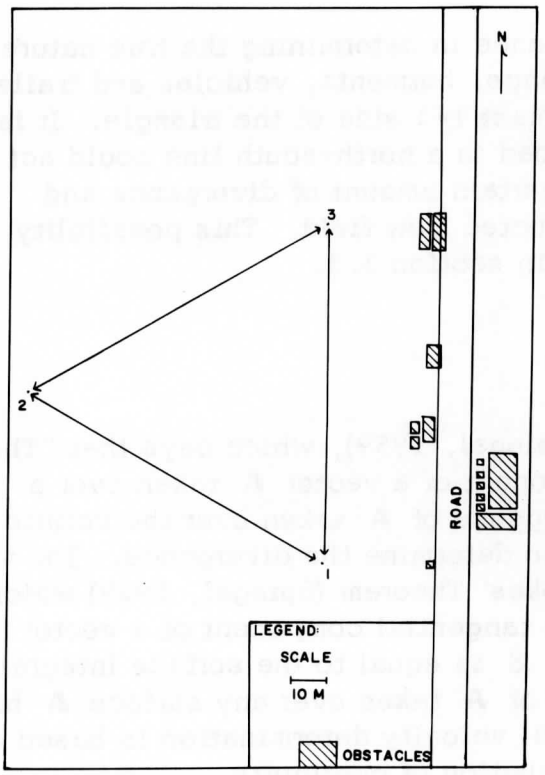

Fig. 1.1. The mast locations are shown in relation to each other as well as to artificial obstacles.

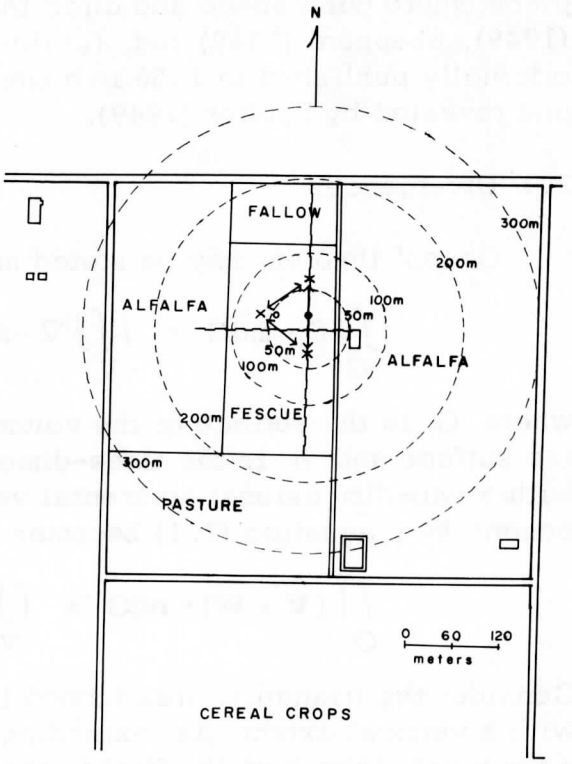

Fig. 1.2. The Davis field site general cropping pattern is shown.

Obstacles of possible consequence in determining the true nature of the wind flow consisted of buildings, hutments, vehicles and trailers some 20 to 30 m to the east of the mast 1-3 side of the triangle. It is possible that obstacles along the road in a north-south line could act as a barrier which would induce a certain amount of divergence and vorticity into the otherwise unobstructed flow field. This possibility will be discussed in greater detail in section 3.3.

2. Theory

Gauss' Divergence Theorem (Spiegel, 1959), which says that "The surface integral of the normal component of a vector $\mathbf{A}$ taken over a closed surface is equal to the divergence of $\mathbf{A}$ taken over the volume enclosed by the surface," is used to determine the divergence. The vorticity determination is based on Stokes' Theorem (Spiegel, 1959) which states that "The line integral of the tangential component of a vector A taken around a simple closed curve S is equal to the surface integral of the normal component of the curl of $\mathbf{A}$ taken over any surface $\mathbf{A}$ having S as its boundary. The vertical velocity determination is based on the divergence in a layer and the equation of continuity.

Gauss' and Stokes theorems have been applied to three points in a plane where wind speed and direction have been measured by Bellamy (1949), Sheppard (1949) and, for divergence only, by Bennett (1955) originally published in 1906 in a memoir to HM Stationary Office, MO174, and revealed by Poulter (1949).

2.1 Divergence

Gauss' theorem may be stated mathematically as

$$\iint_G \mathbf{A} \cdot \mathbf{n}\, dG = \iiint_V \nabla \cdot \mathbf{A}\, dV \qquad (2.1)$$

where G is the surface of the volume V, $\mathbf{n}$ is the unit vector normal to the surface and $\mathbf{A}$ is the three-dimensional velocity vector. Replacing $\mathbf{A}$ with a two-dimensional horizontal velocity vector $\mathbf{V}$ and a vertical component W, equation (2.1) becomes

$$\iint_G (\mathbf{V} + W) \cdot \mathbf{n}\, dG = \iiint_V \nabla \cdot (\mathbf{V} + W) dV. \qquad (2.2)$$

Consider the triangular area formed by the three masts at the Davis site with a vertical extent Δz extending from the surface to the first measurement level, then from the first to the second measurement level, and then successive layers to the top of the masts. Each layer forms a volume

over which the divergences will be determined, based on the wind measurement at the top of the layer and the assumption that the wind vector is uniform over the vertical distance Δz.

Equation (2.2) can be rewritten as

$$\iint_G (\mathbf{V} + \mathbf{w}) \cdot \mathbf{n} \, dG = \iint_{S\,z} \mathbf{V} \cdot \mathbf{n} \, ds \, dz + \iint_A \mathbf{W}_t \cdot \mathbf{n} \, dA - \iint_A \mathbf{W}_b \cdot \mathbf{n} \, dA \tag{2.3}$$

where S is the perimeter of the horizontal cross section of area A, w_t is the vertical velocity at the top of the volume, and w_b is the vertical velocity at the bottom of the volume.

Only three measurement points are available making it necessary to assume that $\mathbf{V} \cdot \mathbf{n}$ is independent of the size of the volume. Then equation (2.2) and (2.3) can be rewritten as

$$\Delta z \oint_S \mathbf{V} \cdot \mathbf{n} \, ds + (\bar{w}_t - \bar{w}_b) \iint dA = \overline{\nabla \cdot \mathbf{V}} \, \Delta z \iint_A dA + \frac{\partial \bar{W}}{\partial z} \Delta z \iint_A dA \tag{2.4}$$

assuming that

$$\frac{\bar{w}_t - \bar{w}_b}{\Delta z} = \frac{\partial \bar{w}}{\partial z}$$

we have that

$$\overline{DIV} = \overline{\nabla \cdot \mathbf{W}} = \int_S \frac{\mathbf{V} \cdot \mathbf{n} \, ds}{A} \tag{2.5}$$

where $\overline{DIV}$ is the horizontal divergence of velocity. It can be shown that

$$\overline{DIV} = \sum_{i=1}^{3} \frac{V_{ni}}{h_i} \tag{2.6}$$

where V_{ni} is the component of the wind speed at the i mast along the altitude h_i of the triangle and positive away from the centroid of the triangle.

2.2 Vorticity

Mathematically, Stokes' theorem is

$$\oint_S \mathbf{A} \cdot \mathbf{t} \, ds = \iint_A \mathbf{n} \cdot \bar{\nabla} \times \mathbf{A} \, dA \tag{2.7}$$

where $\mathbf{A}$ is the three-dimensional velocity vector, S is taken to be the

perimeter of a horizontal cross section of the triangular volume. The unit vector $\mathbf{t}$ is in the horizontal plane tangent to the curve S and unit vector $\mathbf{n}$ is in the vertical plane eliminating terms involving the vertical velocity and considering only the relative vorticity about a vertical axis.

The relative vorticity ξ is $\mathbf{n} \cdot \nabla \times \mathbf{A}$ and assumed independent of the area A, then (2.) can be written as

$$\oint_S \mathbf{V} \cdot \mathbf{t} ds = \xi \iint_A dA \tag{2.8}$$

$$\xi = \frac{\oint_S \mathbf{V} \cdot \mathbf{t} ds}{\iint_A dA} = \frac{\oint_S \mathbf{V} \cdot \mathbf{t} ds}{A} \tag{2.9}$$

Then for the three measurement points at each level it can be shown that

$$\xi = \sum_{i=1}^{3} \frac{V_{\rho i}}{h_i} \tag{2.10}$$

and $V_{\rho i}$ is the wind component normal to the altitude at mast i.

2.3 Vertical Velocity

The equation for conservation of mass in a volume is

$$\frac{\partial \rho}{\partial t} + \rho \nabla \cdot \mathbf{A} + \mathbf{A} \cdot \nabla \rho = 0 \tag{2.11}$$

where ρ density, t = time and ∇ the three-dimensional del operator. Assuming that $\partial\rho/\partial t$ and $\nabla\rho$ may be neglected (Fredericks, 1969), we have that

$$\nabla \cdot \mathbf{A} = \nabla \cdot \mathbf{V} + \frac{\partial w}{\partial z} = 0 \tag{2.12}$$

where $\nabla \cdot \mathbf{V}$ is the horizontal divergence and $\partial w/\partial z$ is the change of vertical velocity w with respect to height. Then

$$w = \int_0^z \frac{\partial w}{\partial z} dz = \int_0^z \nabla \cdot \mathbf{V} \, dz. \tag{2.13}$$

Assuming that $w = 0$ and $\nabla \cdot \mathbf{V} = 0$ at $z = 0$, we have that

$$w(z_2) = w_2(z_1) - \overline{\nabla_H \cdot \mathbf{V}} (z_2 - z_1) \tag{2.14}$$

where z_2 and z_1 are levels of measurement and

$$\overline{\nabla_H \cdot \mathbf{V}} = \frac{(\nabla \cdot \mathbf{V})_1 + (\nabla \cdot \mathbf{V})_2}{2} \tag{2.15}$$

the mean divergence in the layer z_1 to z_2.

A second method of determining the vertical velocity at the top of the volume was tried involving an assumption about the relationship of divergence to height. In this case it was assumed that the horizontal divergence, determined at the top level only, represented the mean divergence of the entire layer below it. This would mean that instead of equation (2.15) one would have:

$$\overline{\nabla_H \cdot \mathbf{V}} = (\nabla_H \cdot \mathbf{V})_{z_2} \tag{2.16}$$

Equation (2.14) then becomes:

$$w(z_0) = w(0) - \overline{\nabla_H \cdot \mathbf{V}} \cdot z_2 \tag{2.17}$$

where $w(0) = 0$.

3. Results

3.1 Computational Technique

The actual computations of divergence, vorticity and vertical velocity from the Davis, California data were carried out on the CDC 1604 computer of the University of Wisconsin Computing Center with funds provided by the U.S. Army Electronics Command, Ft. Huachuca, and on the IBM 1130 computer of the University of Wisconsin, Department of Astronomy, without charge. The data made available by Prof. C. R. Stearns at the time of these computations included simultaneous half-hour means of wind speed for nine levels, wind direction for five levels, and an average wind direction at each of the three masts. This latter quantity was simply a numerical average of the five vanes on the mast. Stearns and Dabberdt (1968) describe how these quantities were obtained and what correction factors, if any, were applied.

The wind speed measurements were not at exactly the same relative level on each mast. In other words, the nominal level of 320 cm was actually 320.8 cm on mast 1, 322.4 cm on mast 2, and 319.8 cm on mast 3. There were differences of similar magnitude at all other levels. It seemed desirable to extrapolate the speed as given at the true height above the ground to the respective common nominal level (20 cm, 40 cm,

80 cm, etc.) above the ground. By doing this, one would at least be calculating quantities for a plane parallel to the local surface. This plane is not necessarily perpendicular to gravity, but these effects can be taken into account.

In order to extrapolate the wind speed to the common levels mentioned above, the logarithmic profile law was assumed and applied in the following form:

$$V = V^{*}k^{-1} \log_e \left(\frac{z+z_0}{z_0}\right) \qquad (3.1)$$

Since the profiles had not been analyzed at the time of computation, a zero displacement height was assumed and a z_0 value of 1 cm was used. These two terms need to be known only in an approximate form for the extrapolation. The ratio of the speed (V_z) at a given level z to that at the nominal height h using the assumptions above produces the extrapolated value (V_h).

$$V_h = V_z \frac{\log_e (h+1)}{\log_e (z+1)} \qquad (3.2)$$

The extrapolated half-hour mean wind speed as determined from equation 3.2 was combined with the half-hour mean wind direction at each mast to represent the average wind vector. The direction used was the arithmetic average of the five vanes on each mast. It was assumed that all levels remained in the "surface layer" or "layer of quasi-constant stress" at all times. This also is probably a valid assumption, especially in the late afternoon-early evening periods where the winds were relatively strong and steady, and strong lapse or unstable conditions prevailed. It will be seen in section 3.2 that during these periods the divergence and vorticity calculations have the greatest reliability. Stearns and Dabberdt made a similar assumption about the wind direction when calibrating each vane. They found the average difference of the individual vanes from the mast average during certain selected unstable periods with strong winds, and corrected for the difference assuming it was a systematic instrument error.

3.2 Description of Results

Examples of actual results of the divergence, vertical velocity and vorticity calculations appear in Figs. 3.1 and 3.2. It is obvious that there are some periods when one would have more confidence in the measurements (and hence also the calculations) than at other times. In order to determine these time periods, certain criteria had to be established. These included considering the response thresholds of the anemometers and vanes. Stearns and Dabberdt (1968) estimated that

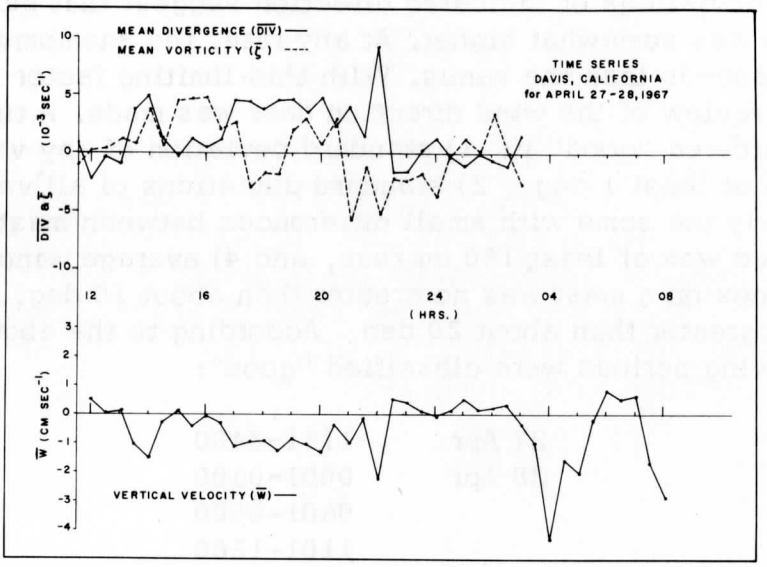

Fig. 3.1. The time series of mean divergence mean vertical velocity computed from the divergence and mean vorticity (broken line) at the 320 cm level for the period 27-28 April 1967 at Davis, California.

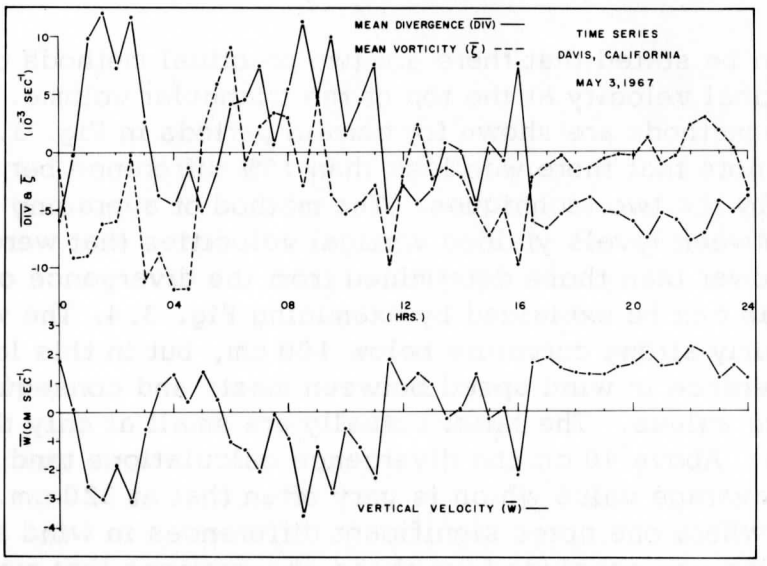

Fig. 3.2. Same as Fig. 3.3, but for 3 May.

the vanes began responding at a wind speed of about 1 m/sec. The standard deviations of indicated direction suggest that perhaps this threshold was somewhat higher. At any rate, the anemometers respond at lower speeds than the vanes. With this limiting factor in mind, a thorough review of the wind direction data was made. A time period was considered "good" if: 1) standard deviation of any vane on each mast was at least 1 deg., 2) standard deviations of all vanes on a mast were nearly the same with small differences between masts, 3) the wind speed was at least 150 cm/sec, and 4) average wind direction between vanes on a mast was no greater than about 10 deg., and between masts no greater than about 20 deg. According to the above criteria the following periods were classified "good":

27 Apr	1131-2400
28 Apr	0001-0300
	0601-0800
	1101-1200
2 May	1601-2400
3 May	1631-2400
4 May	0001-0200
	0931-1500
	1631-2400
5 May	0001-0530
	0701-1200

The rest of the time periods are considered unreliable for the purpose of computation of divergence and vorticity.

It can be stated that there are two practical methods of computing mean vertical velocity at the top of the triangular volume. The results of these two methods are shown for certain periods in Fig. 3.3. It is interesting to note that there was less than 15% difference between the results obtained by the two techniques. The method of averaging divergence values between levels yielded vertical velocities that were generally slightly lower than those determined from the divergence of the top level only. This can be explained by examining Fig. 3.4. The wind profiles exhibit fairly strong curvature below 100 cm, but in this layer there is little difference in wind speed between masts and consequently small divergence values. The latter actually are small at only the 20 and 40 cm levels. Above 40 cm the divergence calculations tend to oscillate about an average value which is very often that at 320 cm. This is also the layer where one notes significant differences in wind speed between masts. One can conclude from these observations that most of the divergence is occurring in the layer above 40 cm. The divergence at 320 cm is an overestimate for the entire layer due to the slight reduction of actual divergence below 40 cm. The two-layer average technique partly accounts for this reduction and thus yields more correct vertical velocities.

3.3 Obstacle Effects

Figures 3.5 and 3.6 show a plot of the divergence and vorticity values for the selected "good" periods of section 3.2 versus the wind direction of mast 1. There is some stratification of divergence with direction and the same can be said, but less emphatically, for vorticity. This suggests that there may have been some obstruction to the flow. Originally, the average wind direction at masts 2 and 3 were corrected for what was thought to be a systematic effect of obstacles (cars, trailers, buildings, etc.) in view of the observation that during strong, fairly steady wind conditions at these masts were nearly always a few degrees different. It was assumed that they should be about the same during these periods if the obstacles had not been there and the corrections were applied to do this.

It is difficult to say whether the procedure above was justifiable or not, because the unobstructed flow is not known. It is suggested that there should have been an adjustment of the wind speed as well as direction since both of these terms would be affected by the presence of obstacles. The author has no suggestions, however, about how this adjustment could or should be made. It is his conclusion, then, that the uncorrected divergence, vorticity and vertical velocity values are the only valid ones obtained from the measurements of this experiment. The "corrected" ones may be used for comparisons among themselves (as was done in section 3.2 with the two vertical velocity measurements, as well as in section 4.4) but cannot be represented at this time as the results of this study.

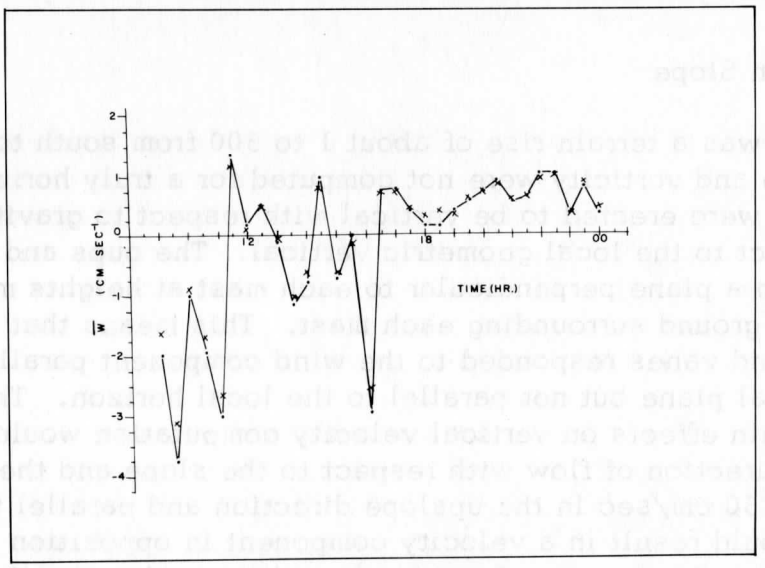

Fig. 3.3. A time series of vertical velocity at the 320 cm level. Two methods were used: 1) top divergence only (solid line), and 2) two-level divergence averages (shown by x's with no connecting line).

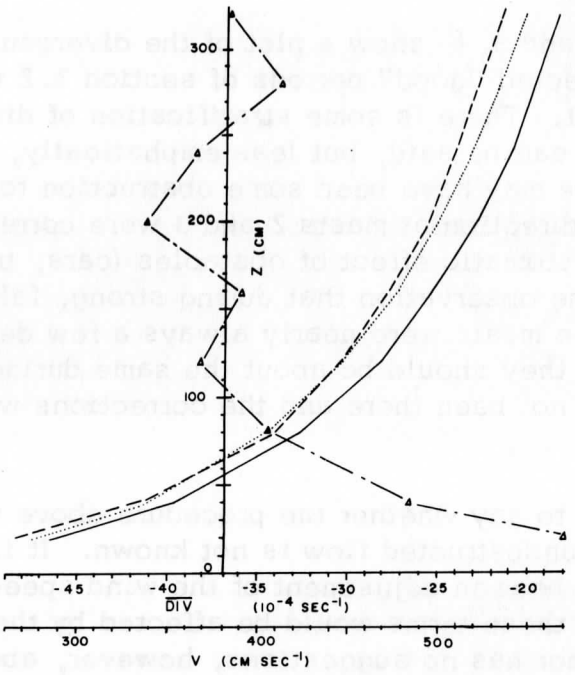

Fig. 3.4 . Vertical profiles of windspeed (V, solid line is mast 1, dashed line is mast 2, and dotted line is mast 3), and the resulting divergence (dash-dot line) for one-half hour period (1631-1700 May 4) which was representative of most other times.

3.4 Terrain Slope

There was a terrain rise of about 1 to 500 from south to north, thus divergence and vorticity were not computed for a truly horizontal plane. The masts were erected to be vertical with respect to gravity but not with respect to the local geometric vertical. The cups and vanes were arranged in a plane perpendicular to each mast at heights measured from solid ground surrounding each mast. This means that theoretically the cups and vanes responded to the wind component parallel to the geopotential plane but not parallel to the local horizon. The extent of these terrain effects on vertical velocity computation would depend upon the direction of flow with respect to the slope and the wind speed. A flow of 250 cm/sec in the upslope direction and parallel to the local horizon would result in a velocity component in opposition to gravity of 0.5 cm/sec. A correction for this effect has not been made in the final results.

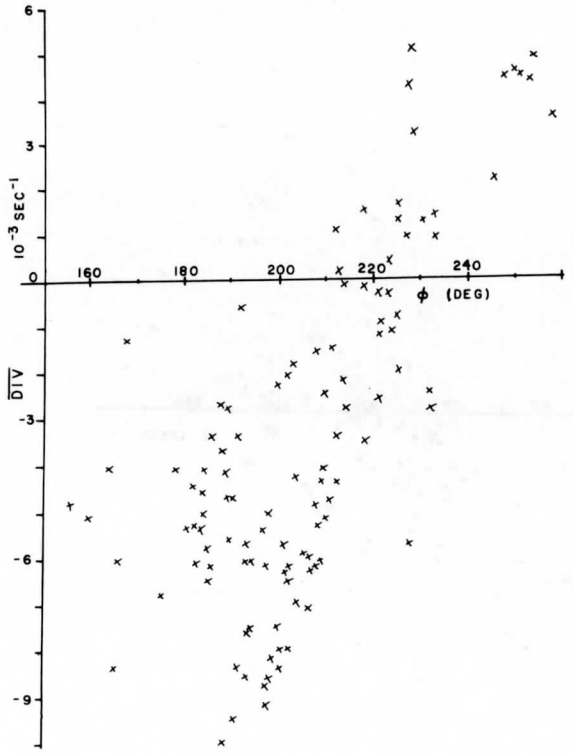

Fig. 3.5 . The divergence at 320 cm as a function of wind direction (ϕ) at mast 1.

4. Error Analysis

4.1 General Discussion

The calculation of divergence and vorticity from the actual wind measured at three or more points is sensitive to observational errors regardless of the size of the area involved. Panofsky (1951) and other authors have illustrated very cogently this point for divergence calculations. The sensitivity arises from the fact that the contributions by the horizontal wind components u and v are of the same order of magnitude regardless of the scale involved. This implies that in general $\frac{\partial u}{\partial x}$ over some finite distance is about the same magnitude and opposite in sign to $\frac{\partial v}{\partial y}$ over the same distance. Consequently, the mean divergence over the area involved is frequently one order of

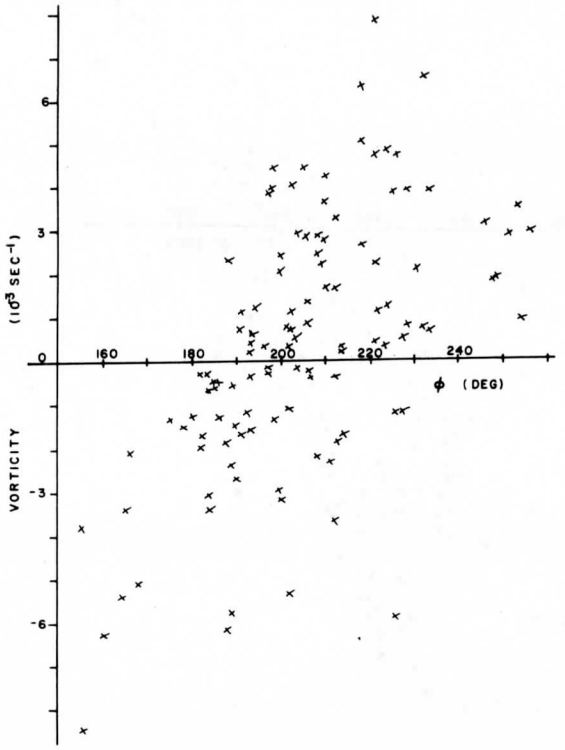

Fig. 3.6. The vorticity at 320 cm as a function of wind direction (ϕ) at mast 1.

magnitude less than the terms used to compute it. This latter magnitude is the same as the discrepancy involved in measuring those terms. The same line of reasoning holds true for vorticity calculations. This computation involves again a small difference of two large numbers. In general one could expect to find nearly 100% error because of discrepancies in raw wind data.

One should not dwell too long on this seemingly insurmountable barrier. The challenge is to attack it at the source of the trouble. That is, raw wind data should be improved. The Davis, California Field Experiment was an attempt to provide this kind of data for the meso-microscale. Table 4.1 shows measured and estimated discrepancies. There were certain times (especially light wind situations) where the data was not satisfactory. On the other hand, there were several extended periods where reliable data was obtained continuously to at least the accuracies indicated. It is to these latter periods that the forthcoming discussion is directed.

4.2 Measurement Errors

Measurement errors in divergence calculations can be attributed to three effects: (1) inaccuracy in measuring the horizontal wind speed with cup anemometers, (2) discrepancy in measuring the wind direction properly with vanes, and (3) inaccurate measurement of the horizontal and vertical dimensions of the triangular prism shaped volume studied. Each of these effects will be discussed separately and then a possible collective effect will be presented.

In Table 4.1, estimations of the measurement inaccuracies due to observational and instrument error are summarized. The discrepancy of $\pm$ 5 cm/sec for the wind speed was derived from an examination of the standard deviations of that quantity which were found during the calibration procedure. The error in wind direction was based on an estimate of how well one could align the vanes on a distant object of known bearing. Since the direction used for computations was an average of five vanes, it was assumed that the alignment error was $\pm$ 1 deg. The additional degree deviation comes from an estimate of the error in receiving the signal from the instrument. The discrepancy in the normal angle necessarily is the same as in the wind direction.

The inaccuracies shown for horizontal and vertical distances were subjective estimates of how well one can measure lengths. Deviations of these latter quantities only distort the shape of the triangular volume, and, probably do not alter the sense (sign) of the calculated quantities (divergence, vorticity, vertical velocity) but rather affect their magnitude somewhat.

Table 4.2 represents calculations of the error contributions of the various measured quantities to the resultant computations of this study. It is evident that even with the relatively small inaccuracies of observed quantities, a fairly large percentage error (170%) in divergence, vorticity, and vertical velocity results if all errors at the three masts were additive. The relatively best condition (57%) is based on the magnitude of the error in partial divergence (vorticity) at a single mast. It can be noted that the resultant errors due to direction effects show reduced discrepancies for the "worst" and "best" conditions. The "most probable" error (98%) was determined by computing the square root of the sum of the squares of the three partial divergence (vorticity) discrepancies.

Table 4.1

Measurement Inaccuracies

Item	Symbol	Order of Mag.	% Error	Mag. of Error
Wind Speed	V	300 cm/sec	1.7	5 cm/sec
Wind Direction	ϕ	200 deg	1.0	2 deg
Normal Angle	ϕ_n	45 deg	4.4	2 deg
Triangle Altitude	h	8660 cm	0.5	50 cm
Height	z	100 cm	1.0	1 cm

Table 4.2

Error Contributions

Item	Symbol	Order of Mag.	% Error	Mag. of ± Error
cos ϕ_n	cos ϕ_n	.707	3.5	.0247
Normal Speed Component	V cos ϕ_n	212 cm/sec	5.2	11 cm/sec
Parallel Speed Component	V sin ϕ_n	212 cm/sec	5.2	11 cm/sec
Partial Divergence	$\frac{V \cos \phi_n}{h}$	0.024 sec^{-1}	5.7	.00140 sec^{-1}
Partial Vorticity	$\frac{V \sin \phi_n}{h}$	0.024 sec^{-1}	5.7	.00140 sec^{-1}
Divergence and Vorticity (Worst)	$\frac{\overline{DIV}}{\bar{\zeta}}$	0.0024 sec^{-1}	170	.004200 sec^{-1}
Divergence and Vorticity (Best)	$\frac{\overline{DIV}}{\bar{\zeta}}$	0.0024 sec^{-1}	57	.001400 sec^{-1}
Normal Speec Component (Direction Effects Alone)	V cos ϕ_n	212 cm/sec	3.5	7.4 cm/sec
Partial Divergence (Direction Effects Alone)	$\frac{V \cos \phi_n}{h}$	0.024	3.5	.000857
Divergence (Worst) (Direction Effects Alone)	$\overline{\overline{DIV}}$	0.0024	105	.00257
Divergence (Best) (Direction Effects Alone)	$\overline{\overline{DIV}}$	0.0024	35	.000857
Divergence and Vorticity (Most probable)	$\frac{\overline{DIV}}{\bar{\zeta}}$	0.0024	98	.002400
Divergence (Most Probable) (Direction Effects Alone)	$\overline{\overline{DIV}}$	0.0024	61	.001500

4.3 Simplifying Assumptions Concerning Wind Direction

Two computations of divergence were made. The first used only the wind direction at tower 1 and assumed that the flow was unidirectional. The second computation came from a consideration of the mean wind speed and direction at all three towers. The resulting vertical velocities (computed in the same manner for each scheme) were compared and some revealing disparities noted (see Fig. 4.1). As previously indicated, the late afternoon and early evening periods are the most reliable from the standpoint of steadiness of wind direction and general agreement of the same between masts. Even though these conditions prevailed at these times, there still was little agreement in vertical velocity. In fact, there were times when the two schemes showed opposite trends. One might argue that such differences could be attributed to the errors in alignment of the vanes and that the more vanes one used the greater were his chances for error. This would suggest that the vertical velocities obtained from the unidirectional scheme are representative of the true physical conditions. Even if this were true, one should not be led to this conclusion on the basis of the unidirectional results. It still remains that horizontal divergence is obtained from the variations of the horizontal wind vector (with emphasis on the word vector). One must consider spatial variations of both speed and direction as a single and inseparable entity. In fact, in order to keep from being misled one should avoid speaking of "speed divergence" apart from "direction divergence."

5. Conclusions

5.1 A Future Approach

The cup anemometer-wind vane system was used in the Davis experiment for representing the mean vector. Statements of MacCready (1966) and Bernstein (1967) suggest that there could be significant errors in divergence and vorticity estimates using this system. Such, however, is not the case. The cup anemometer yields:

$$V = \sqrt{u^2 + v^2} \tag{5.1}$$

where V is the speed from the cup and u and v are cartesian components of V. If it is now assumed that u is the true vector component, v is the crosswind component which provides the overestimation of vector speed. The mean cup speed can then be represented as:

$$\overline{V} = \overline{u\sqrt{1 + \frac{v^2}{u^2}}} \tag{5.2}$$

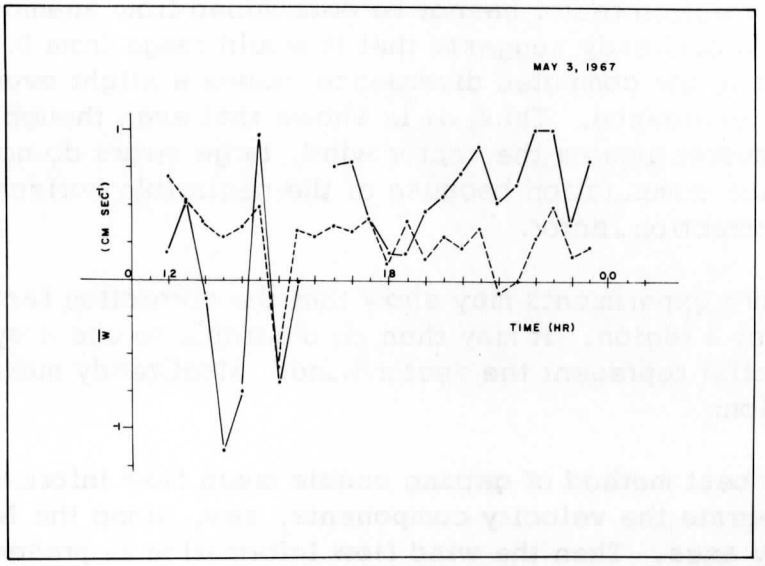

Fig. 4.1. The time series of vertical velocity ($\bar{w}$) at 320 cm (computed from top level divergence only) is shown for two cases on 3 May: 1) Mast 1 wind direction used at all masts (solid line), and 2) Individual mast direction used (broken line).

Neglecting products with perturbations 5.2 reduces to:

$$\bar{V} \approx \bar{u}(1 + C) \tag{5.3}$$

where the correction factor C is:

$$C = \sqrt{1 + \frac{\overline{v^2}}{\overline{u^2}}} - 1 \tag{5.4}$$

The horizontal divergence would require a differentiation of 5.3 with respect to x.

$$\frac{\partial \bar{V}}{\partial x} = \frac{\partial \bar{u}}{\partial x}(1 + C) + \bar{u}\frac{\partial C}{\partial x} \tag{5.5}$$

where $\frac{\partial \bar{V}}{\partial x}$ is computed and $\frac{\partial \bar{u}}{\partial x}$ is actual divergence. Anemoclinometer data collected simultaneously with the anemometer-vane values of this experiment and provided by Professor C. B. Tanner, Department of Soils, University of Wisconsin, shows that variations in the correction factor at the Davis site were of the order 10^{-3} per 100 m. This would cause

the term $\bar{u}\frac{\partial C}{\partial x}$ to be negligible in comparison with other terms in 5.5 which are several orders of magnitude larger. The absolute magnitude of the correction factor cannot be determined from anemoclinometer data but MacCready suggests that it would range from 0.0 to +0.1. This would make the computed divergence values a slight overestimation of the true divergence. Thus, it is shown that even though the cup-vane system overestimates the vector wind, large errors do not enter in the divergence computation because of the negligible horizontal variation of the correction factor.

Future experiments may show that the correction factor is not negligible over a region. It may then be desirable to use a system which would better represent the vector wind. MacCready makes the following suggestion:

> The best method of getting usable mean flow information is to integrate the velocity components, say, along the N-S and E-W axes. Then the wind flow information is presented as a vector. This eliminates the error inherent in trying to average speed along an average direction.

This could be accomplished by using a u-v propeller anemometer. Alignment problems would still exist but a true wind vector would be obtained. Three of these instruments could be placed at the vertices of a triangle such that one horizontal arm is directed along the altitude and the other perpendicular to it. Once this system were aligned it would remain fixed, whereas the vane system might tend to change its alignment calibration. An additional feature of the u-v system is that the output could easily be converted to partial vorticity and partial divergence with the aid of a small on-site computer.

5.2 Concluding Remarks

The Cooperative Field Experiment at Davis, California provided a significant first opportunity to measure small scale divergence and vorticity in the earth's surface layer. The system contained errors, but the experience gained represents valuable information for future experiments. It is clearly the vector wind which is of interest here and steps should be taken to insure that this is the quantity which is measured. One should also consider expanding the array of measurement points. This would give some idea of the linearity of the flow—a basic assumption in the Bellamy-Bennett technique. A nonlinear flow can be handled by the technique, as mentioned in section 4.3, if the nature of the nonlinearity is known. The addition of more measuring

points would also make it possible to try mathematical schemes for estimating divergence such as has been done by Fischer (1962). He represented the observed winds as mathematical functions of space. The divergence is then computed by taking the space derivatives of the wind functions.

If one were going out to specifically measure the divergence and vorticity in the surface layer and were not particularly interested in the spatial variation of vertical wind profiles, he would not need to measure at as many levels as was done at Davis. A single measurement in the one to four meter range would yield a good first approximation to the desired quantities. This point is illustrated in section 3.2 and in Figs. 3.3 and 3.4.

Future investigators might do well to insure that artificial obstructions are not as close to the measurement site as in this experiment. The sensors of course also obstruct the flow but with the present state of the art one can only hope to minimize their effects. Results of this study have shown that the mean vertical velocity in a surface layer is not necessarily zero, and the next logical step is to examine the effects of this finding on the momentum budget and also on the structure of the vertical wind profile.

REFERENCES

1. Bellamy, J. C. (1949). "Objective Calculations of Divergence, Vertical Velocity, and Vorticity." Bull. Am. Met. Soc., 30, pp. 45-49.

2. Bennett, G. T. (1955). "Calculation of the 'Dilitation' of Area from Simultaneous Wind Records at Three Neighboring Stations." Selected Meteorological Papers of Sir Napier-Shaw, MacDonald (London, 1955), pp. 130-131.

3. Bernstein, A. B. (1967). "A note on the Use of Cup Anemometers in Wind Profile Experiments." J. of Appl. Meteor., 6, pp. 280-286.

4. Dabberdt, W. F. (1968). "Tower-Induced Errors in Wind Profile Measurements." J. of Appl. Meteor., 7, pp. 359-366.

5. Fischer, G. (1962). "Uber die horizontale Stromungsdivergenz im Zusammenhang Mit Temperatur- und Oruckanderungen im jet-stream-Feld." Beitr. Physik d. Atm., 35, pp. 108-125.

6. Haltiner and Martin (1967). "Vorticity and Circulation, ch. 20." Dynamical and Physical Meteorology, McGraw-Hill, New York.

7. Lettau, H. H. (1967). "Essay on the Aerodynamic Roughness of the Site of 'MiMeEx' at Davis, Calif., 1967." Unpublished Paper.

8. MacCready, P. B. (1966). "Mean Wind Measurements in Turbulence." J. of Appl. Meteor., 5, pp. 219-225.

9. Panofsky, H. A. (1951). "Large-Scale Vertical Velocity and Divergence." Compendium of Meteorology, Am. Met. Soc., Boston, pp. 639-646.

10. Poulter, R. M. (1949). "Correspondence." Bull. of Am. Met. Soc., 30, p. 297.

11. Schmidt, P. J. (1965). "An Investigation of Polynomial Filtering of Vertical Wind Profile and the Objective Computation of Kinematic Divergence and Vertical Motion." M.S. Thesis, Univ. of Wisconsin, Madison, Wis.

12. Shaw, Sir N. (1955). Selected Meteorological Papers, MacDonald, London.

13. Sheppard, P. A. (1949). "Large Scale Vertical Motion in the Atmosphere." Quart. J. Roy. Met. Soc., 75, pp. 188-192.

14. Stearns, C. R. and Dabberdt, W. F. (1968). "Collecting and Processing of Micrometeorological Data for the Spring, 1967, Cooperative Field Experiment at Davis, California." Final Report, Contract No. DAA DO 4-67-C-0117, US Army Electronic Proving Ground, Ft. Huachuca, Ariz.

THERMAL RESPONSE OF A PLANT CANOPY TO DRIFTING CLOUD SHADOWS*

John Lambert
Department of Meteorology
University of Wisconsin at Madison

ABSTRACT

An investigation of the thermal response of a Sumac canopy to solar radiation pulses induced by drifting cloud shadows (with periods between less than one to more than ten minutes) is described. General interpretation of the observed data is given in terms of energy fluxes with respect to the canopy layer. Additional micrometeorological observations of the canopy during a 24-hour period of clear weather are also included. An approach is presented for the expression of surface temperature variations in terms of time spectra variations of a radiation forcing function and the physical and thermal properties of the surface.

1. Introduction

Surface temperature fluctuations of a body may often be related to fluctuations of the radiant energy incident upon the body. Thermal response has been defined by Lettau (1959) as the ratio of the surface temperature amplitude to the amplitude of the radiation forcing function. The initial presentation of the thermal response theory (Lettau, 1951) described the temperature distribution in terms of net radiation, the thermal parameters of the air and the underlying medium, and the nature of the interface between the two. A method for the experimental investigation of the theory was given which was subsequently tested with respect to several different surface types.

A first series of controlled shading experiments was carried out by Lienesch (1961) on a mown, grass-covered surface, but the results were inconclusive. Similar shading experiments were performed first by Federer (1962) on a concrete surface, and then by Turner (1962) on the

---

*Part of this work was submitted to the University of Wisconsin in partial fulfillment of the requirements for the degree of Master of Science, with Professor H. Lettau as thesis advisor.

ice of Lake Mendota at Madison. The present study is a series of shading experiments under natural conditions with restricted control. The surface in this study is a plant canopy; that is, the actively transpiring portion of a dense grouping of plants, so that the underlying soil can be considered only as a remote portion of the environment.

Many investigators have determined individual leaf temperatures; a partial list includes Watson (1934), Curtis (1936), Wallace and Clum (1938), Gates (1964), Linacre (1964) and Knoerr and Gay (1965). Temperatures of leaves in response to light intensity variations have been measured by Shull (1936), Ansari and Loomis (1959), and Gates (1963), among others. Generally, sunlit leaf temperatures remain above air temperature when the latter is less than about 30 C. When the air temperature is above this value the leaves tend to be slightly cooler than the surrounding air due to transpiration. The time lag of leaf temperature behind changes in radiant intensity have been observed to be between one and three minutes, depending on the mass and moisture content of the leaf.

The study of the thermal response of a canopy is an observation of an assembly of leaves in their natural positions, which also includes energy exchange of the leaves with one another. A canopy of Smooth Sumac, Rhus glabra, was selected for the study because of its relatively uniform, well-defined nature and obvious similitude to a model forest. Also, the canopy chosen was 1.5 to 2 m above the ground, which made the installation of micrometeorological instruments in this miniature version relatively easy as compared with the prototype forest.

In contrast to earlier work by Lienesch and Turner, the shading and unshading of the canopy was provided by nature by drift of isolated cumulus clouds. Duration of cloud shading ranged from less than ten seconds to about twelve minutes, usually at quite irregular intervals. Light reflected from approaching clouds and the indefinite cloud margins caused departures from the square waves of solar radiation induced in previous shading experiments. These irregularities were a disadvantage, but artificially shading a large enough area of canopy would have been difficult and impractical.

2. Description of Site

The Sumac stand was located on the Grady Tract of University of Wisconsin arboretum; Fig. 1 is a map of the area also showing instrument placement. The site was on a low, level ridge which was oriented N 34 W, with the terrain sloping 3% to the northeast and 6% to the southwest. The underlying soil was a Wyocena series, loamy fine sand.

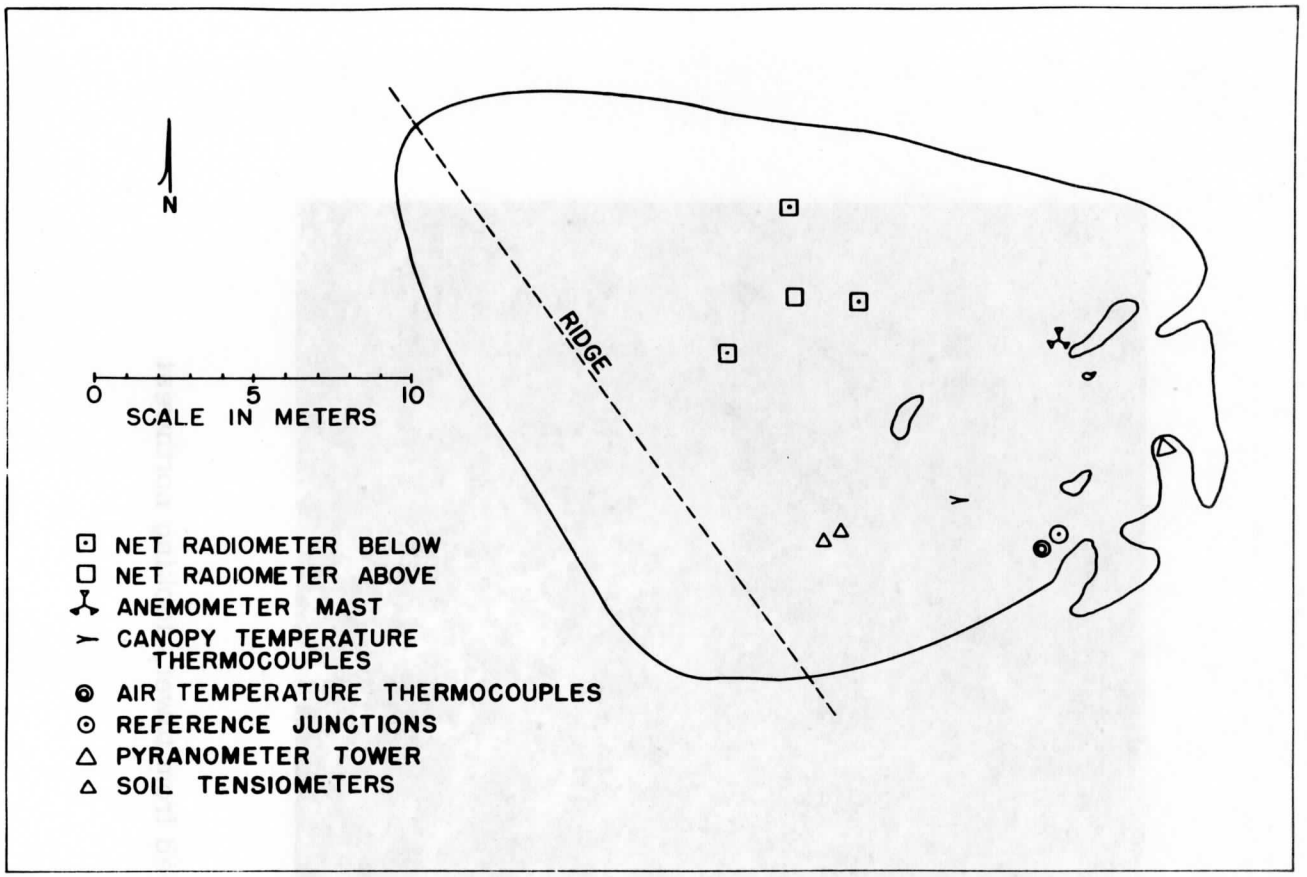

Fig. 1. Sumac stand, showing location of instruments

The tallest Sumac trees were on the ridge, the height of the canopy decreasing to the southwest but sloping more gently to the northeast. The upper surface of the canopy was about 2.1 m above the ground in the area of the radiometers, 1.8 m at the wind mast, and 1.6 m at the air temperature mast. Thus the portion of the canopy under observation sloped N 83 E at about 8%. The vertical thickness of the canopy was about 20 cm in all parts of the stand, and the degree of closure about 75% (see Figs. 3 and 4). The only irregularities were slight undulations and occasional holes, as indicated on the map and in Fig. 2. The stand margin was delineated only by a lesser density of plants and more holes in the canopy. Tall grass of about 30 cm height covered most of the ground surface, with only a few scattered honeysuckle and smaller sumac plants between this and the canopy.

Fig. 2. Sumac stand, as viewed from tower, looking northwest

Fig. 3. Cross-sectional view of Sumac canopy

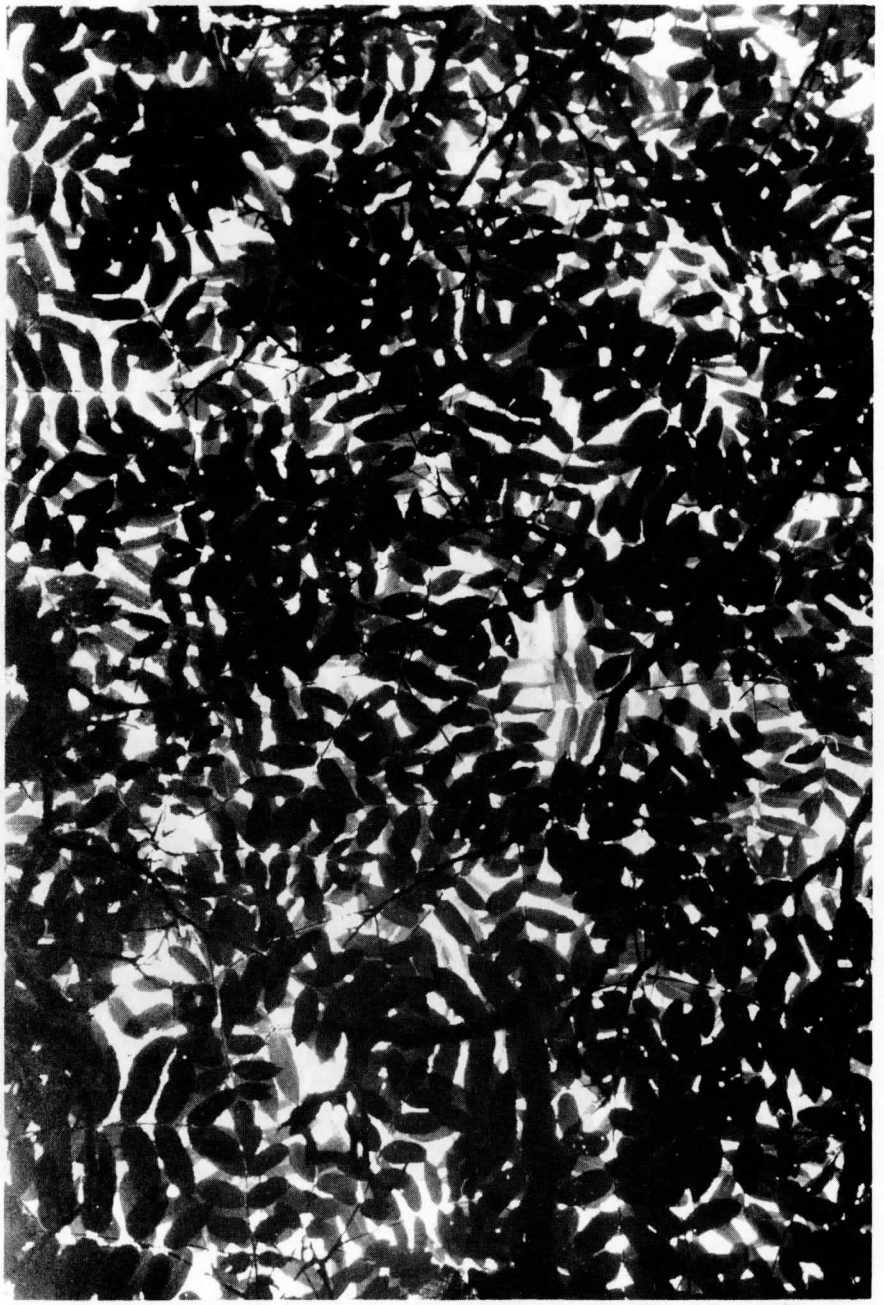

Fig. 4. Sumac canopy from below, looking vertically upward

3. Instrumentation

3.1 Temperature Measurements

Fine wire thermocouples were threaded into leaves at the top and at the bottom of the canopy. At each level two junctions in different leaves were connected in series to space-average variations in leaf orientation. The thermojunctions were made by electroplating copper onto about 50 cm of a 1 m length of #40 gauge constantan wire. Installation of a thermocouple consisted of threading the constantan end of the wire through holes pricked in two adjacent veins on the underside of a leaf. The wire was pulled through until the thermojunction was placed between the veins, which held the wire against the leaf. Some radiation heating may have been incurred by the light transmitted by the leaves, but it was considered negligible. The thermocouple signals were recorded continuously on a Honeywell Visicorder Oscillograph.

Ventilated, shielded, 10-junction thermopiles were arranged at four levels above the canopy and at one point below to measure the air temperature differences between these levels. Similar 2-junction thermopiles served to measure independently (as a check) the temperature differences of the highest and the lowest levels, relative to a reference temperature. The nominal heights of the thermopiles above the average canopy were 29, 48, 83 and 146 cm, the upper limit being the height of the mast and the accuracy being limited by uncertainties in an estimate of the true canopy height. The construction and operation of the thermopiles are discussed by Super (1964). The time constants of the units were of the order of three minutes.

The reference for all thermocouples was the soil temperature at 40 cm depth. A platinum resistance thermometer was held in close thermal contact with the thermopile reference units by wrapping 1 mm diameter copper wire tightly around all of them. Each of the thermopile signals was recorded every 15 seconds and the resistance thermometer signal was recorded once each minute.

3.2 Radiation Measurements

A silicon solar cell and an Eppley pyranometer were mounted on top of a six-meter tower at the edge of the stand. The short time constant of the solar cell (less than one millisecond) provided instantaneous radiant intensity values. The 10-junction Eppley unit served as a check with respect to radiant intensity.

A ventilated net radiometer of the type described by Suomi, Franssila and Islitzer (1954) was supported by a pole 70 cm above the middle of the canopy and three more were positioned below the canopy in the same area to obtain the average net radiation at this level. The radiometer signals were handled on the second channel of the digital printer and were recorded once every 15 seconds.

3.3 Wind Measurements

A mast to measure a vertical profile of the air movement across the canopy was equipped with anemometers of the light weight type manufactured by Thornthwaite Associates, Inc. One of them was below the canopy 75 cm from the ground, and five other anemometers were at nominal heights of about 17, 57, 97, 137 and 177 cm above the canopy. Counting mechanisms were read and recorded at intervals of from nine to thirty-five minutes.

3.4 Moisture Measurements

Soil tensiometers made by the Irrometer Company of Riverside, California were installed early (late May, 1966) so they would be in satisfactory contact with the soil. They were placed at depths of 25 cm and 50 cm to give a general indication of the relative availability of soil moisture to the plants. The values of the vacuum gauges were recorded each day at about noon.

Wet bulb depressions were obtained at the two lowest air temperature measurement levels, that is, above and below the canopy. The design of these units is described by Super (1964). The wet bulb depressions were recorded once each minute by the same system that handled the thermopile signals.

4. Observational Data

4.1 Data Collection

On 20 July, 1966 conditions were favorable for the development of cumulus clouds. Data were recorded during two observation intervals; one of thirty-seven minutes from 1043 to 1120 CST, and another two hundred and four minute interval from 1203 to 1527 CST. Favorable conditions occurred again on 2 August, observations were made for forty-four minutes starting at 0907 CST, and forty-three minutes from 1001 until 1044 CST. This produced data on micrometeorological effects of cloud shadings during four separate intervals. Table 1 shows the

meteorological similarities and differences of the intervals during which data were collected. A sample of the data collected during cloud passage is illustrated in Fig. 5.

Table 1. Meteorological data during the four observation periods. c = amount of sky cover (in all cases cumulus); Z = height (m) of cloud base (both c and Z from recordings at the nearest USWB Station, Truax Field, Madison); G = global radiation (ly/min); T_{146} = air temperature (°C) at 146 cm; RH = relative humidity (%) at 29 cm; V_m = wind speed (cm/sec) averaged for all profile levels.

Date	CST	c	Z	G	T_{146}	RH	V_m
8-2-66	0907 to 0951	1/10	900	1.28	19.0	60	134
8-2-66	1001 to 1044	1/10	900	1.45	19.7	61	157
7-20-66	1043 to 1120	3/10	1200	1.57	20.0	49	139
7-20-66	1203 to 1527	3/10	1300	1.49	21.1	44	104

4.2 Radiation

The records show that one hundred thirteen cloud shadings occurred during the experiment. However, the solar cell recorded many radiation fluctuations which were not readily discernible to the human eye. As a cloud approached, the light reflected from its side would increase the total global radiation by about 0.05 to 0.1 ly/min before the cloud shaded the canopy. Under the cloud, light was still being reflected from the cloud edges, and this reflected intensity would first decrease and then increase as the trailing edge of the shadow approached. Global radiation was reduced by the cloud to about twenty to thirty percent of its unshaded intensity. All of these fluctuations produced deviations from an ideal square wave of global radiation, but they could be analyzed adequately.

Similar to global radiation, the net radiation above the canopy was reduced under a cloud to about five to fifteen percent of its unshaded intensity. The net radiation beneath the canopy varied relatively the most. Although the average of three sensors was used, the spatial structure of the canopy caused additional, short-time extreme

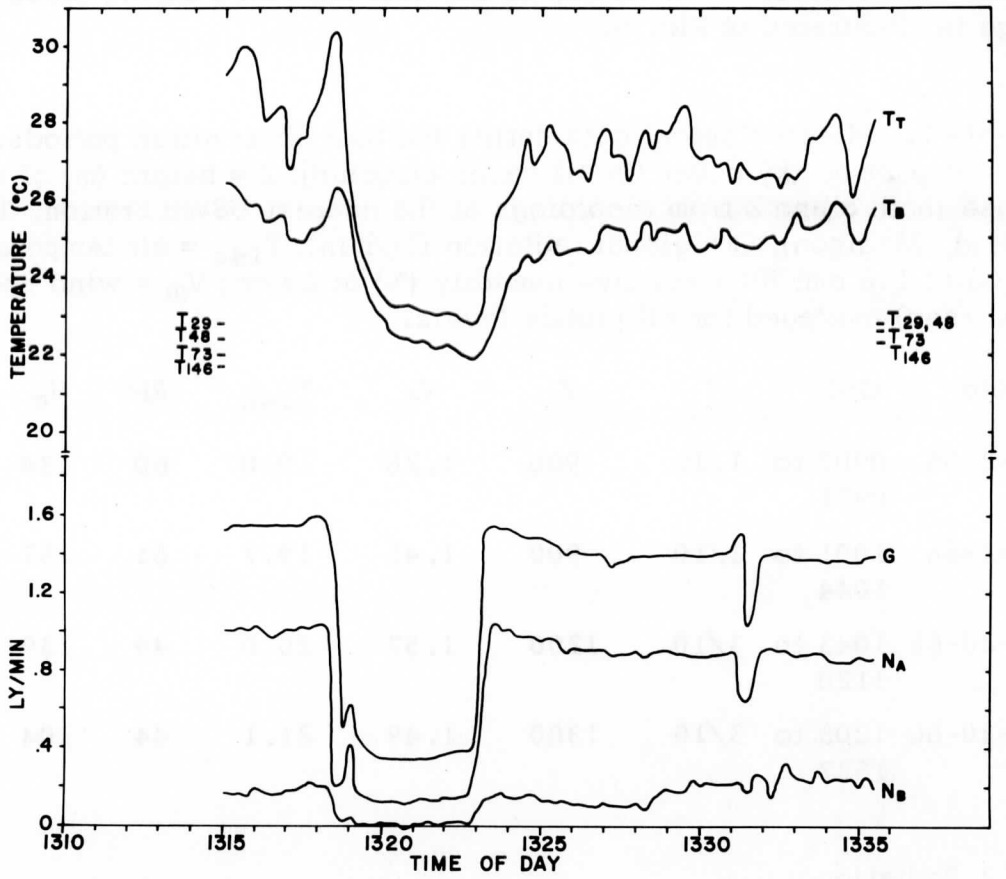

Fig. 5. Data sequence, 20 July 1966. T_T and T_B temperature at top and bottom of canopy, G = global radiation, N_A and N_B net radiation above and below canopy.

fluctuations. For example, within sunflecks, nearly full intensity solar beam radiation was added to long-wave radiation from a hemisphere of leaves, which were warmer than clouds or clear sky. In the unshaded condition, the net radiation beneath the canopy generally amounted to about ten to fifteen percent of the same measurement above the canopy. The difference between these two measurements approximated the radiant energy flux density intercepted by the canopy.

4.3 Wind

No attempt was made to observe fluctuations in wind speed of shorter periods than the time averages of from nine to thirty-five minutes mentioned earlier. The horizontal extent of the canopy was too limited to establish

an equilibrium wind profile. It was expected initially that the wind measurements would only result in a relative indication of the air flow across the canopy, and that this could then be generally related to the transport of sensible or latent heat to or from the canopy.

4.4 Canopy Temperature

Under sunlit conditions, both top and bottom canopy temperatures were above ambient air temperature, the upper leaves being warmest. Shading by a cloud reduced the canopy-air temperature differences (at both the top and bottom) by about half for the 20 July shadings, and actually reversed sign on 2 August. The temperature gradient from top to bottom of the canopy reacted in a similar manner. On 2 August the clouds were smaller and more widely scattered than on 20 July. When a small cloud shades the canopy, there remains a significant portion of clear sky to which the canopy radiates. In addition, higher wind speeds on 2 August may have aided in the depression of canopy temperatures below air temperature by increased transfer of latent heat.

Sensible heat transfer from the canopy also seemed to be directly influenced by wind speed, as would be expected from theory. Even though the wind speeds were not recorded continuously, it was found that gustiness was distinctly related to the sunlit canopy temperature. Whenever a gust came along, the canopy temperatures dropped, but under shaded conditions the lowered canopy temperatures showed no such reaction, probably because of the decreased canopy-air temperature differences.

4.5 Air Temperature

Contrary to initial expectation, the air temperature about one and one-half meters above the canopy did not tend to remain fairly constant through all of the shading periods. In spite of their time constants of about three minutes, the air temperature sensors indicated significant changes even for two and three minute shadings. From the sunlit lapse conditions, shading changed the vertical temperatore profile toward the isothermal, and for longer periods even produced inversion conditions. This can have resulted from the great horizontal extent of the shaded area and the tendency for cooled air to move along beneath the shading cloud.

The air temperature below the canopy seemed to behave also contrary to expectations. With sunlit conditions, instead of being cooler under the canopy, it was one to two degrees warmer than above the canopy. Also, at night (see Fig. 8), the air below the canopy was

cooler than even the first level above. There seem to be two factors at work. First, due to incomplete canopy closure the energy exchange was not all taking place at the canopy surface (see section 5.2); that is, radiation heating and cooling of the soil surface was significant. And secondly, the sumac stand margins were sufficiently closed to limit air flow through the stand and prevent mixing, thus creating the extreme air temperatures for the stand.

4.6 Moisture

The soil tensiometers were read at about noon on every day the stand was visited. Continuity between the readings permitted interpolation of missing data except on days following precipitation. The time sequences of the tensiometer readings from the two depths are illustrated in Fig. 6. Here the ordinate is in relative units of tension; thus, low readings indicate ready availability of moisture. Also included on this graph are the daily totals of precipitation at Truax Field.

As the soil moisture was gradually depleted during the period preceding 10 July, the remaining moisture was being held at high tensions. On two occasions the air seal on the 25 cm tensiometer was broken by the tension, and several sumac trees on the stand border wilted and died abruptly during this period. When precipitation did come, there was a seven day lag of soil moisture replenishment at 50 cm behind that at 25 cm.

Generally, both the relative and absolute humidities were higher beneath the canopy than above it. This can be attributed to the reduced air motion beneath the canopy and reduction in transport of water vapor away from the canopy. Even considering the different time of day, the atmospheric moisture appeared to be greater on 2 August than on 20 July, and this may have had some effect on the thermal response of the canopy.

5. Diurnal Cycle

During a twenty-four hour period of generally clear weather, readings were taken during a fifteen minute interval every two hours beginning at 0700 CST on 30 July. Aside from yielding a low frequency value for the thermal response relations, some results are of general interest. The radiation and temperature sequences appear in Figs. 7 and 8. Not included in the graph is global radiation measured by the Eppley pyranometer. It showed higher values than the solar cell in the morning and lower values in the afternoon and attained peak values about an hour earlier than either the solar cell or the net radiometer; both facts indicate that the Eppley was somewhat out of level toward the east.

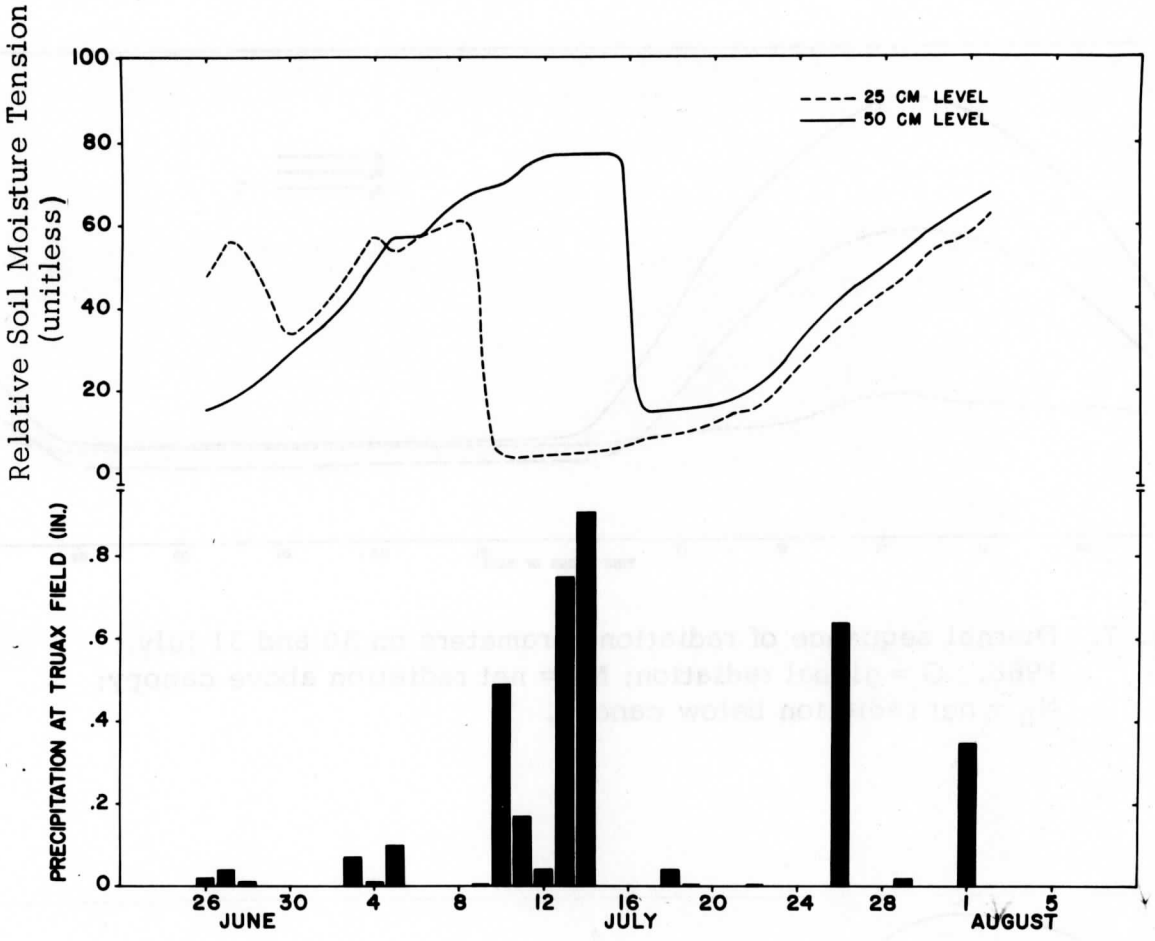

Fig. 6. Soil moisture tension and precipitation records.

The net radiation above and below the canopy reversed sign simultaneously at 1750 and 0540, in a rather abrupt reversal of the net heat exchange of the canopy. This coincided closely with the reversal of the air temperature profile.

The canopy temperatures reached a peak before noon, suggesting a strong coupling to radiation since the canopy was "out of level" toward the east. Even though the canopy temperatures decreased after noon, the air continued to be heated until the canopy cooled below air temperature. Note the temporary increase in canopy temperatures and air temperature at 29 cm in the middle of the night. This was associated with an increase in wind speed at this time, and hence greater mixing and conduction of heat to the canopy.

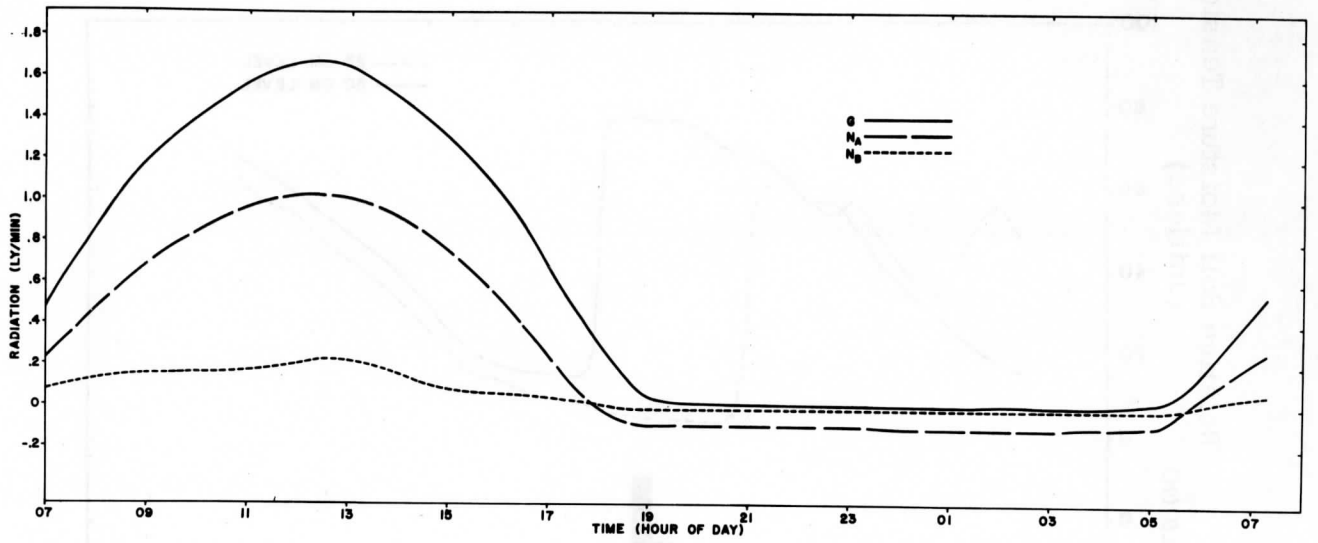

Fig. 7. Diurnal sequence of radiation parameters on 30 and 31 July, 1966. G = global radiation; N_A = net radiation above canopy; N_B = net radiation below canopy.

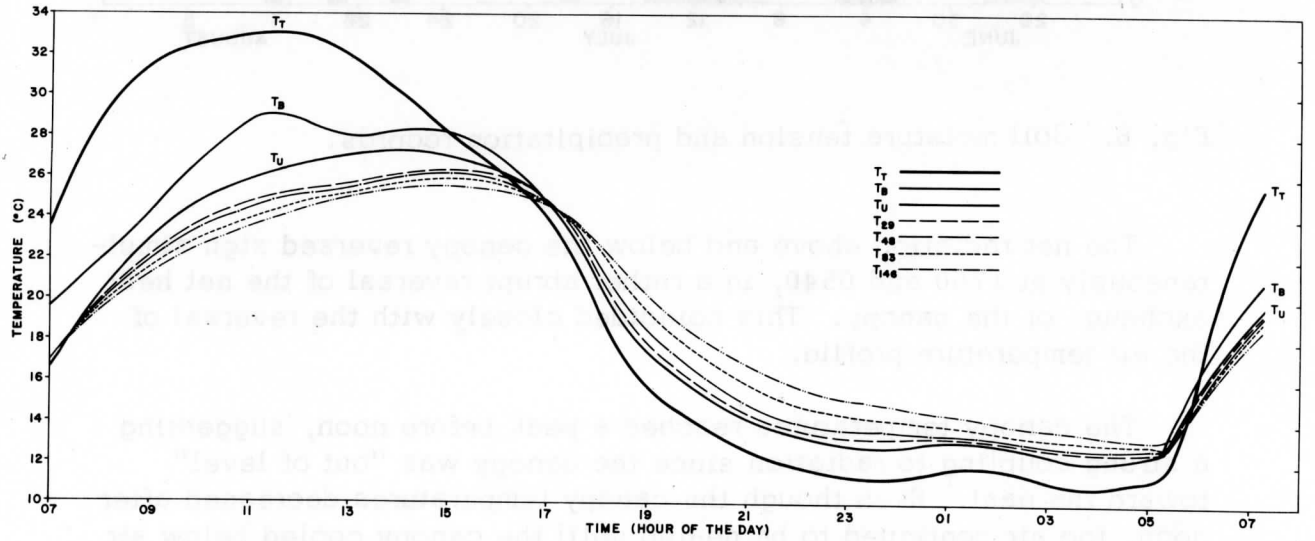

Fig. 8. Diurnal sequence of canopy and air temperatures on 30 and 31 July, 1966.

6. Analysis of Data

6.1 Amplitudes, from Variance Spectra

Spectral analysis was used to estimate the amplitudes of the radiation and canopy temperature fluctuations associated with the variable cloud shading periods. The spectral analysis interpolates between the actual cloud shading periods and produces amplitudes of many intermediate periods; it also extrapolates the data to longer periods, with an associated decrease in reliability. The four observation intervals were analyzed separately, which helped to bring deficiencies in some of the data to light. Only relatively short period shadings occurred on 2 August and during the first interval on 20 July. In fact, on 2 August only one shading exceeded a minute. The analysis indicated that the data from short shading periods could not be extended to longer periods, so only data from the long observation interval on 20 July, 1966 were used to discuss canopy thermal responses. Additional data from the diurnal cycle provided amplitudes for the diurnal (1440-minute) period. Computed were amplitudes of global radiation as measured by the solar cell, net radiation above the canopy and canopy temperature.

6.2 Thermal Response

Thermal response of the canopy surface was defined in section 1.1. Amplitude ratios were computed as a function first of global radiation and then of net radiation above the canopy. Graphical plots of observed thermal response of the canopy top surface relative to global radiation, and also relative to net radiation, are presented in Fig. 9.

As might be expected, the canopy surface temperature responds more closely to net radiation than to global radiation. This is partly due to the larger amplitude of the global radiation, since a decrease in net radiation caused by a cloud shading represents not only a decrease in global radiation but also includes both reflected global radiation and outgoing longwave radiation (decreased surface temperature). Furthermore, there can be an increase in incoming longwave radiation (if the cloud base is relatively "warm"). For longer periods the radiation emitted from the surface decreases further, the cloud may be larger, so the difference in response is dependent upon the length of shading period.

7. Conclusions and Comments

The dependency of the canopy surface temperature response (to either global or net radiation cycles) upon shading period has implications with respect to the canopy's energy budget. As shading periods are shortened

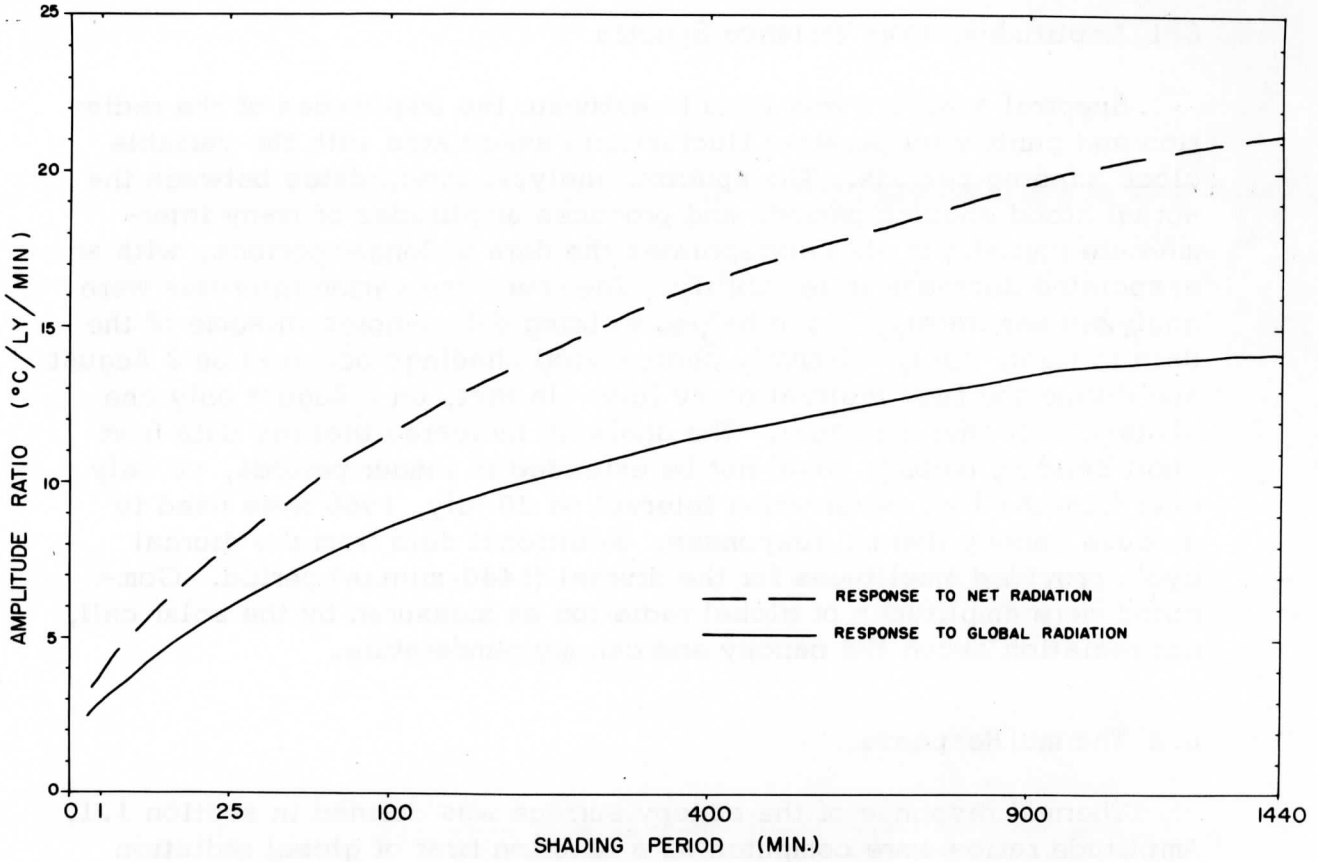

Fig. 9. Thermal response of the canopy surface to global radiation and net radiation for afternoon observations of 20 July 1966.

the temperature amplitude is decreased. Due to limited heat storage in the canopy, its thermal properties become increasingly important in the thermal response at the higher frequency radiation oscillations. For longer shading periods the sensible heat stored in the canopy becomes negligible and the canopy acts simply as an interface where the net radiation is transformed into latent and sensible heating of the atmosphere. For these longer periods the rate at which the latent and sensible heat can be transferred away from the canopy is critical. The intensity of over-all air motion is an important factor in this respect, and equally important is the aerodynamical surface roughness as determined by the structure of the vegetative canopy.

The potential for representing energy budgets of various vegetation types in terms of thermal response curves such as Fig. 9 is obvious. One difficulty is lack of precise definition of height of temperature

measurements relative to the canopy. Energy absorption and transformation is occurring through a layer of canopy. However, extinction coefficients based on spectral properties and arrangements of leaves in the canopy could partially account for this discrepancy. In addition, a radiative surface temperature measured by an infrared thermometer from some standard position (i.e., the vertical) could be used even though it might not refer to the same level at which energy is absorbed. Thus, for any given vegetative surface one could characterize the thermal response and energy budget on the basis of spectral and thermal properties of the leaves and their vertical and horizontal distributions in the canopy, provided that appropriate soil and soil moisture data could be obtained.

Acknowledgments

Appreciation is extended to the following people associated with the Meteorology Department at the University of Wisconsin: John C. Turner for his advice and criticism during the planning stages of the research; Professor Charles R. Stearns for his assistance in the construction and maintenance of instruments; and especially Professor Heinz H. Lettau for overseeing the research work and offering guidance or criticism when needed. The conscientious work of Mary Beth Schumacher in data handling, Donald Perry in drafting, and Russell Johnson in instrument maintenance is acknowledged.

References

Ansari, H. Q., and W. E. Loomis, Leaf Temperature, Amer. J. Bot. 46: 713-717, 1959.

Brun, W. A., Rhythmic Stomatal Opening Responses of Banana Leaves, Phy. Plant. 15: 623-630, 1962.

Curtis, O. F., Leaf Temperatures and the Cooling by Radiation, Plant Phys. 11: 343-364, 1936.

Evans, L. T. (Ed.), Environmental Control of Plant Growth, Academic Press, London-New York, 1963.

Federer, C. A., Thermal Response of a Dry Surface to Shading Cycles of Short Period, Masters Thesis (Soils), University of Wisconsin, 1962.

Gates, D. M., Leaf Temperature and Transpiration, Agron. J. 56: 273-277, 1964.

Gates, D. M., Leaf Temperature and Energy Exchange, Archiv. fur Meteor., Geophy., and Bioclim. 12(2), 1963.

Gates, D. M., W. M. Hiesey, H. W. Milner, and M. A. Nobs, Temperature of Mimulus Leaves in Natural Environments and in a Controlled Chamber, Dept. of Plant Biology, Carnegie Institution.

Knoerr, K. R., and L. W. Gay, Tree Leaf Energy Balance, Ecology 45: Winter 1965, pp. 17-24.

Lettau, H., Theory of Surface Temperature and Heat-Transfer Oscillations Near a Level Ground Surface, Am. Geophys. Union Trans. 32: 189, 1951.

Lettau, H., Research Problems in Micrometeorology, Task 65-58-0026, prepared under contract DA-36-039-SC-80063 (USAEPG), University of Wisconsin, 1959.

Lienesch, James H., Experimental Investigation of the Thermal Response of the Air-Soil System to Controlled Radiation Pulses, Master's Thesis, Dept. of Meteor., University of Wisconsin, 1961.

Linacre, E. T., A Note on a Feature of Leaf and Air Temperature, Agric. Meteor., 1: 66-72, 1964.

Rasche, K., Heat Transfer Between the Plant and the Environment, Amer. Rev. Plant Phys. 11: 111-126, 1960.

Shull, C. A., Rate of Adjustment of Leaf Temperatures to Incident Radiation, Plant Phys. 11: 181-188, 1936.

Suomi, V. E., M. Franssila, and N. F. Islitzer, An Improved Net-Radiation Instrument, J. Meteor. 11: 276-282, 1954.

Super, A. B., A Study of Small Scale Air Mass Modification Over Lake Mendota, Masters Thesis (Meteorology), University of Wisconsin, 1964.

Turner, J. C., A Thermal Response Experiment of Lake Ice, Masters Thesis (Meteorology), Univ. of Wisconsin, 1963.

Van Wijk, W. R., W. R. Derksen, and H. Goedkopp, Turbulent Heat Exchange in the Air Near the Ground, Physica, 25: 1259-1270, 1959.

Wallace, R. H. and H. H. Clum, Leaf Temperatures, Amer. J. Bot. 25: 83-97, 1938.

Watson, A. N., Thermal Emissivity and Plant Temperatures, Amer. J. Bot. 21: 605-609.

Wolpert, A., Heat Transfer Analysis of Factors Affecting Plant Leaf Temperature, Plant Phys., 37: 113-120, 1962.

Scanner's note:

This page is blank.

THERMAL RESPONSE OF A CONCRETE SLAB TO CONTROLLED DAYTIME AND NIGHTTIME CYCLES OF RADIATION*

John Colin Turner
Department of Meteorology
University of Wisconsin at Madison

ABSTRACT:

In a micrometeorological field experimentation, artificial radiation cycling was produced by sun shadings as well as a grid of heat lamps. By appropriately varying the lamp voltages, incident radiation could be controlled to resemble a simple sinusoidal curve.

A concrete slab (75 feet by 50 feet) was used in which heat flow sensors were installed to a depth of 12 cm, and measurements of air temperatures (to a height of 6 cm), net radiation and solar radiation, as well as wind speeds (to a height of 150 cm), were made.

Radiation pulses with periods ranging from 5 to 40 minutes were induced. Data were collected on 9 field experiments, 4 by day and 5 by night. The forcing functions and the response functions (surface temperature, heat fluxes into the air and concrete) were harmonically analyzed.

Within measurement uncertainties which are discussed, measured thermal response agreed with that predicted by the theory developed by Lettau.

1. Introduction

This work is the latest in a series of studies (Lienesch (1961), Federer (1962), Turner (1963), and Lambert (1967)) at the University

*This work is an extract from the thesis submitted to the University of Wisconsin in partial fulfillment of the requirements for the Ph. D. degree, with Professor Lettau as advisor.

of Wisconsin concerned with the field measurement of the thermal response of ground/air interfaces. The theoretical basis was provided in two papers by Lettau (1951, 1952). Lettau's model, as set forth in those papers, was an attempt to predict the temperature response of a ground/air interface in terms of both some basic thermal and aerodynamic properties of the media and the frequency-amplitude properties of the net radiation forcing function.

At that time, Lettau referred to such predictive attempts as constituting a "synthetic climatology." Recently (unpublished class notes, 1960's) he has used the term climatonomy instead. In this field, he would include the quantitative explanation (response functions) of other climatic elements as well as that of the primary element—temperature.

In a paper in 1959, Lettau suggested that semicontrolled field experiments might be possible for the testing of his model, and for the determination of the thermal admittance of the ground. The thermal admittance of a heat-conducting medium is given by $\mu = (\lambda C)^{\frac{1}{2}}$ (cal cm^{-2} det C^{-1} $min^{-\frac{1}{2}}$), where λ is the thermal conductivity and C is the volumetric heat capacity. Priestley (1959, p. 99) uses the term "conductive capacity" for the same quantity, and both terms are usefully descriptive. A knowledge of effective thermal admittances is basic to a quantitative explanation of local climates. The greater the thermal admittance of the underlying medium, for example, the less will be the surface temperature response to the same heat flux changes.

Lettau proposed that natural surfaces be subjected, by means of movable sunshades, during the mid-day hours on cloudless days, to controlled step functions of radiation. Frequency cycles in the range 1 cycle/min to 1 cycle/hour are more useful for estimating effective thermal admittance than the natural geophysical cycles (day and year). The shorter the cycle, the greater the proportion of the radiant energy forcing function which enters and leaves the ground. This is a consequence of the height dependence of the eddy diffusivity (for heat, K_H) of the air (e.g., see Van Wijk, 1963, p. 124).

In the present paper, another way of inducing a radiation forcing function will be examined as well; heat lamps directed at the ground surface. To avoid complicating factors such as evaporation and physical inhomogeneities, a large slab of concrete will represent the ground, the same block as was used by Federer (1962).

It was decided to examine the practicability of nocturnal experimentation, using heat lamps above the surface as the source of the forcing function. Days which are cloudless for the several hours around

noon are infrequent in Wisconsin. In addition, artificial illumination provides the possibility of using a forcing function which is close to sinusoidal, rather than the step-function which necessarily results from day-time experimentaion.

2. Description of the Experiments

2.1 Site of Experiments

The experiments were carried out at the Arlington Experimental Farm of the University of Wisconsin. Federer has fully described the site in his thesis (1962), and the reader is referred to that work for more details. The slab of concrete measures 75 feet east-west by 50 feet north-south, and is about 6 inches thick, resting on 6 inches of gravel.

In the summer of 1962, after Federer's work was completed, I added new sensors to the concrete. The central one-meter square of the central ten foot square of concrete was removed and newly constructed sensors were installed.

To secure a uniform albedo for the concrete surface, the whole block was given a coat of "Thoroseal" ("pearl grey") in mid-summer of 1965, before any of the runs to be described later were made. "Thoroseal" is a filler and sealer, used to protect concrete surfaces. It is applied like paint or a thin plaster to the concrete. One month after the coating was applied, the albedo of the surface was measured near noon on a cloudless day by successively directing the Kipp pyranometer (appropriately levelled in each case) at the sky and at the concrete. The mean value of four such comparisons was 43 percent, with extremes of 44 percent and 41 percent.

2.2 Instruments

I measured temperature and heat flow using copper-constantan thermocouples of four junctions each between the following twelve levels: .1, .5, 1, 1.5, 2, 3, 4, 5, 6, 7, 8 and 12 cm.

I measured air temperature also by thermocouple methods. To secure representative profiles of air temperature, it was necessary to make measurements close to the surface, in the lowest few cm. I made a very light framework of plexiglass, carrying a thermopile of ten junctions to measure a delta T over a vertical distance of five cm. Additionally, a three-junction thermopile was mounted at the lower level, to measure absolute temperature via a reference bath. The plexiglass frame was covered by a minimal radiation shield of sheet aluminum;

and the whole unit could be raised or lowered at the end of a horizontally swinging arm, about 1.5 m long. The swinging arm was activated by an electric motor drive. Because of the simple design of the mechanism, the speed of horizontal travel was not constant; the arc of motion (length about 110 cm) was traversed in about two seconds in one direction and four seconds in the other. The mean ventilation rate was therefore about 35 cm/sec.

Dr. Tanner of the Department of Soils supplied a single net radiometer of the forced-ventilation (Suomi) type. The sensing plate of this instrument was mounted at a height of 34 cm. I used the same mounting system as Federer. During the daytime measurement runs, a Kipp and Zonen pyranometer ("solarimeter") was mounted on a small wooden stand, to bring it to the same height as the net radiometer.

Thornthwaite three-cup anemometers were used to measure wind profiles. I had available 2 four-anemometer masts. On some runs eight anemometers, on other runs only four anemometers on one mast were available.

When the two masts were in operation, one was placed close to the other sensors (1 - 2m away) and the other was put further away (3 - 4 m) but having about the same length of wind fetch across the concrete surface. The aim was to use the more distant mast as an approximate control.

On the more distant mast, nominal heights of the anemometers were 21, 41, 81 and 161 cm. On the nearer mast, heights were 11, 31, 71 and 151 cm. On the occasion of each run, however, heights of each sensor above the local concrete surface were measured. The actual heights were usually within $\pm$ 1 cm of the nominal height.

2.3 Experimental Control of the Radiation Forcing Function

A four-legged framework on wheels provided the basis for both daytime and nighttime control of the forcing function. During the day, the frame which was a square with sides ten feet long was covered with a tarpaulin to shade the surface, and at night it supported lamps directed at the surface. I made the frame and its legs from 16-gauge angled and predrilled steel, which comes in ten-foot lengths. The frame was about two meters above the surface.

In daytime use, I positioned the frame so the shadow from its tarpaulin was on the sensors, with as much upwind fetch as possible inside the shadow. All the runs were made sufficiently far into autumn

to allow placement such that the sensors had open sky and not the tarpaulin directly above them. During unshaded half-periods, the framework was pushed to one side or downwind.

In nighttime use, the tarpaulin was removed and twenty 120 volt, 250 watt reflector infrared lamps were added to sockets on the underside of the framework. The front surfaces of the lamps were about 179 cm above the concrete surface. A 220 volt input, 5000 watt variable transformer supplied power to the lamps which were connected in parallel pairs.

I measured, on one night only, a relationship between net radiation and voltage for net radiometer and lamps in normal placement. This relationship can only be approximate because of such variables as surface temperature, radiation from the sky and aging properties of the lamps. Slight hysteresis effect was present, perhaps depending on the direction of voltage change.

For the present work, however, no effort was made to take the variables into account. The calibration curve was used to construct graphically a step function of voltages, approximating a sinusoidal function (shown in Fig. 1). The time intervals for the application of particular voltages were adjusted proportionally to the total length of the period which was being imposed. Output of the lamps was such that an amplitude of about 0.15 ly/min net radiation was obtainable in each cycle. Even the rough and ready method I have described here was capable of producing forcing functions which usually had 95% or more of their variance in the first harmonic.

2.4 Recording of Data

The signals from sensors within the concrete were led via a 24-position, one rpm stepping switch to a Honeywell Accudata II DC amplifier, and then to a Hewlett-Packard 405CR DC digital voltmeter. The voltmeter was read by a Hewlett-Packard 561B digital printer, which produced a printed paper strip.

The particular combination of equipment which is listed above has been developed as a system by C. R. Stearns over the past 7 - 8 years. In that time it has been used, for instance, by Super (1964), Hamilton (1965) and Lambert (1967). For technical details, the reader is referred to Stearns (1962).

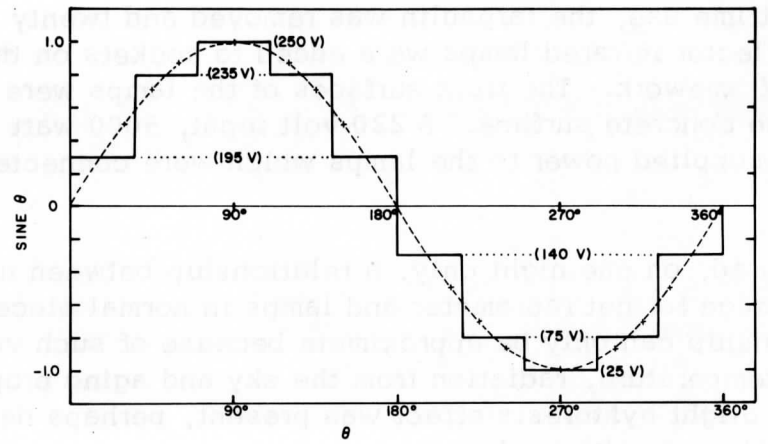

Fig. 1. Theoretical sine curve (dashed line) and the step function of net radiation which was constructed to approximate it.

2.5 Description of the Experimental Runs

Five runs were made in the 1964 season and nine in the 1965 season. Only the data from the 1965 season have been examined for this thesis, because a preliminary examination showed that data from 1964 were inferior in some respects. The 1965 runs extended from August 23 to November 4. Four were done in the daytime, five at night. Two of the daytime runs included natural shadings by fairweather cumulus clouds, but this aspect of the data has not been examined for the thesis. On all other occasions, night and day, the sky was cloudless.

3. Analysis of Data

3.1 Parameters

In Section 2.1, it was mentioned that surface albedo values of 0.43 were determined. To compute the outgoing longwave radiation, a value for the emissivity of concrete was required. Data in the literature are conflicting (e.g., Brooks, 1959, vs. Holden and Greenland, 1951), and the value of 0.98 obtained by Federer (1962) was finally used. Aerodynamic surface roughness z_0 for the concrete was estimated to equal 0.010 cm.

It remained to determine u^*, the other aerodynamic parameter of Lettau's models. My lowest anemometer was at about 11 cm, providing a favorable height:fetch ratio for the expected minimum fetch of 10 m. Presumably too, this anemometer was close enough to the surface for the wind profile to be close to the simple logarithmic form regardless of whether conditions were adiabatic or diabatic.

I calculated u^* for all the runs using equation (3.1.1), with $z_0 = 0.01$ cm and $z = 11$ cm nominal height (varying slightly from run to run). u^*, as calculated, ranged from 2 cm/sec to 34 cm/sec for the nine runs, in each case averaged over periods varying from 5 to 29 minutes.

For values of u^* as low as 2 cm/sec we must inquire whether or not flow might be called "smooth." Sutton (1953, p. 82) following Nikuradse, list the following criteria:

$$\text{Smooth flow: } \frac{u^* z_0}{\nu} < 0.13$$

$$\text{Fully-rough flow: } \frac{u^* z_0}{\nu} > 2.5$$

where ν is the kinematic viscosity of air. At 10 degrees C, for instance, ν is 0.14 cm^2/sec (Smithsonian Meteorological Tables, 1958). Thus, for $u^* = 2$ cm/sec and $z_0 = 0.01$ cm,

$$\frac{u^* z_0}{\nu} \approx .14 .$$

To achieve fully-rough flow with the given surface roughness parameter, a u^* of 35 cm/sec would be required, according to Nikuradse's second criterion. However, Nikuradse's results were obtained under laboratory conditions. In my field situation, air passing across the smooth surface of the concrete has had a very recent history of passage across the much rougher nearby grass, and might be expected to retain some turbulence properties. Accordingly, it seems reasonable to accept some relaxation of the criteria, and I shall assume that fully rough flow prevails.

There was every expectation that the concrete would behave as a homogeneous conductor of heat. Accordingly, an analysis was performed to test this hypothesis.

For a homogeneous conductor (e.g. see Van Wijk) 1963) straight-line relationships obtain between both the natural logarithm of the amplitude of the i^{th} harmonic versus depth, and the phase angle of the i^{th}

harmonic versus depth. Lettau (1954, and in Dalrymple, et al., 1963) has elaborated on this treatment and shown that for a homogeneous conductor, a direct plot of the natural logarithm of the amplitude versus the phase angle of the same amplitude should yield a straight line with a 1:1 slope. Such a plot has been made for the first harmonic of the 20 minute periods for Runs 2 and 7, including eight depths (0.1 cm to 5 cm) for Run 2 and seven depths (0.1 cm to 4 cm) for Run 7.

It seems valid to conclude from inspection of the diagram that at least in the top few cm the concrete behaved as a homogeneous conductor. From Lettau's development (Dalrymple, et al., 1963), we obtain the thermal diffusivity, K, to be 0.0117 cm^2/sec (0.702 cm^2/min).

By definition $K \equiv \lambda/C$. An inspection of values of λ and C for concrete in the literature (e.g., Ingersoll, 1948; Carslaw and Jaeger, 1959) suggests that C is somewhat more conservative than λ. Federer (1962) found the following values for K, C and λ using a method for K similar to the one I have used, and C and λ ultimately from the calibration factor for his heat flux plate at 7 cm:

K: 0.674 cm^2/min

C: 0.50 $cal/cm^3/deg\ C$

λ: 0.337 cam/cm/min/deg C

By regarding the C for the concrete used in my experiments as being the same as that used in Federer's (a value which is close to the mean of the values quoted in the two works mentioned above) namely 0.50 $cal/cm^3/deg\ C$, and accepting my estimate for K (0.702 cm^2/min) λ is calculated to be 0.351 $cal/cm/min/deg_1 C$ (0.00584 cal/cm/sec/deg C) and μ is 0.419 $cal/cm^2/deg\ C/min^{\frac{1}{2}}$ (0.0540 $cal/cm^2/deg\ C/sec^{\frac{1}{2}}$).

3.2 Calculation of Heatflux

In practice, the temperature integral method is often combined with a flux plate, the former measuring storage changes in those layers above the plate. Tanner (1963) provides a critical summary of the three methods of estimating soil heat flux density. After some preliminary examination, I decided to use two methods to calculate B_0 for the runs in the form

$$B_0 = -\lambda \left(\frac{\Delta T}{\Delta z}\right)_{0 \text{ to } 1 \text{ cm}}$$

and the temperature integral-flux plate combination:

$$B_0 = \left(\begin{matrix}\text{change in heat storage} \\ \text{in the top } \frac{1}{2} \text{ cm}\end{matrix}\right) + \left(\begin{matrix}\text{heat flux plate} \\ \text{at } \frac{1}{2} \text{ cm}\end{matrix}\right)$$

Values for λ and C as discussed earlier in this section were used, together with the sand bath calibration factor for the 0.5 cm flux plate.

The results of computations for two representative 20 minute periods are given in Figs. 2 and 3. Net radiation values are included for comparison. All in all, the combination method appears to give results which best connect with the net radiation patterns. For instance, the spikes shown between half-periods in the combination method's results in Fig. 2 seem reasonable physically, since surface temperatures change very rapidly at those times. Theory indicates that for periods as short as 20 minutes at a concrete surface, more than 90% of the forcing function should be partitioned towards heating the concrete. Harmonic analysis of the data in the two figures yields the results summarized in Table 1. Flux plate data alone were not analyzed.

Table 1. Results of harmonic analysis of B_0 data from two sample 20 minute periods, Runs 4 and 8.

		Run 4	Run 8
R_0	Amplitude first harmonic (ly/min)	0.273	0.152
	Relative variance first harmonic (%)	81	97
B_0	by temperature gradient method		
	Amplitude first harmonic (ly/min)	0.202	0.156
	Relative variance first harmonic (%)	87	98
	R_0 phase - B_0 phase (radians)	-0.234	-0.237
	$\Delta B_0 / \Delta R_0$	0.74	1.03
B_0	by temperature integral method		
	Amplitude first harmonic (ly/min)	0.223	0.192
	Relative variance first harmonic (%)	81	80
	R_0 phase - B_0 phase (radians)	-0.237	-0.161
	$\Delta B_0 / \Delta R_0$	0.82	1.26

It seems that both methods can overestimate B_0, as well as provide phase angles which are slightly greater than that of the forcing function instead of slightly less as theory predicts (and diurnal measurements confirm).

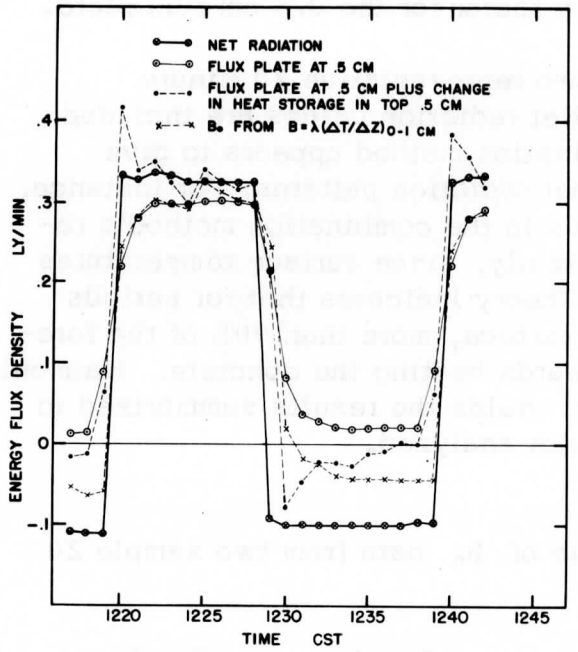

Fig. 2. Results from three methods of estimating B_0, compared with R_0, during the third 20 minute period of Run 4 (daytime).

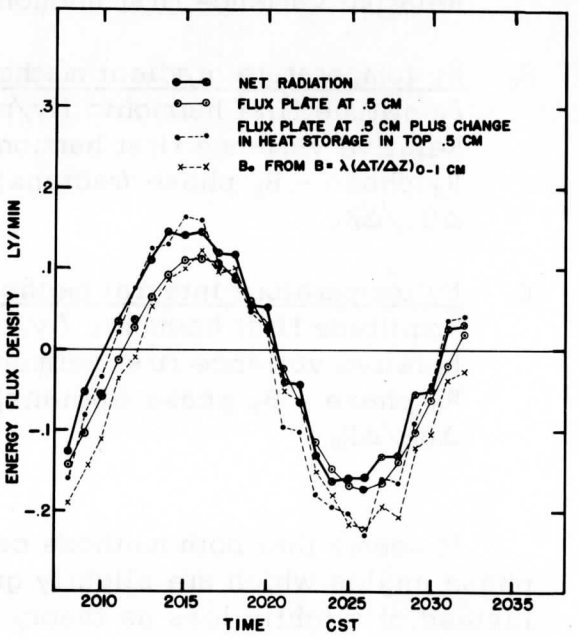

Fig. 3. Results from three methods of estimating B_0, compared with R_0, during the third 20 minute period of Run 8 (nighttime). Period extends from 20.10 to 20.29 CST.

3.3 Experimental Results Compared with Theory

In Figs. 4 and 5 are plotted the data obtained for two representative runs—Runs 2 and 7, respectively. Particular emphasis was placed on 10 and 20 minute periods during the experiments, it being felt that their length was short enough to be convenient for several repetitions, and yet long enough so that the lamps or shade did not need to be handled too often. With very short periods, too, a minute-by-minute sampling system, such as the one I used, is too infrequent to adequately record the information.

For a complete listing of the results, reference is made to the original thesis manuscript of the author. Surface temperature (T_0) values were corrected for long term trends before being analyzed.

We seek to compare field measurements with model predictions. The thermal responses are our prime concern, but other amplitude ratios as well as phase angle differences are also of interest. For Lettau's older and newer model (Section 1.2), we used a computer program to obtain numerical values for all the ratios and phase differences of interest. The volumetric heat capacity of the air was held at 0.0003 cal/cm^3/deg C. The thermal admittance of the slab was set at 0.419 cal/cm^2/deg C/min$^{\frac{1}{2}}$. The period was varied from 40 minutes to 5 minutes in 5-minute steps and the adiabatic mixing velocity from 34 cm/sec to 2 cm/sec (the extremes encountered in the nine runs) in 1 cm/sec steps. For each of the combinations of the independent variables, a computation of the various amplitude ratios (e.g., $\Delta T_0/\Delta R_0$, $\Delta A_0/\Delta R_0$, $\Delta T_0/\Delta B_0$) and phase angle differences was printed out. The mean surface temperature was an independent variable varying from about 0 to 28°C during the nine runs.

The two models yield very similar predictions for the circumstances of these experiments, as we see by inspecting Figs. 6 and 7. In contrast with the strong influence of frequency on thermal response, the influence of u^* is weak, while that of surface temperature is almost negligible.

The observations have been grouped according to the prevailing u^*. While scatter is considerable, a clear gradation according to u^* is discernible. Generally the higher u^* values refer to daytime runs. The lowest five points for the 20 minute period are all from Run 3. They are all that there is of Run 3, and are in such wide disagreement with all other values that there must be a strong suspicion that there was an error in their measurement or computation. However, I have not been able to find such an error.

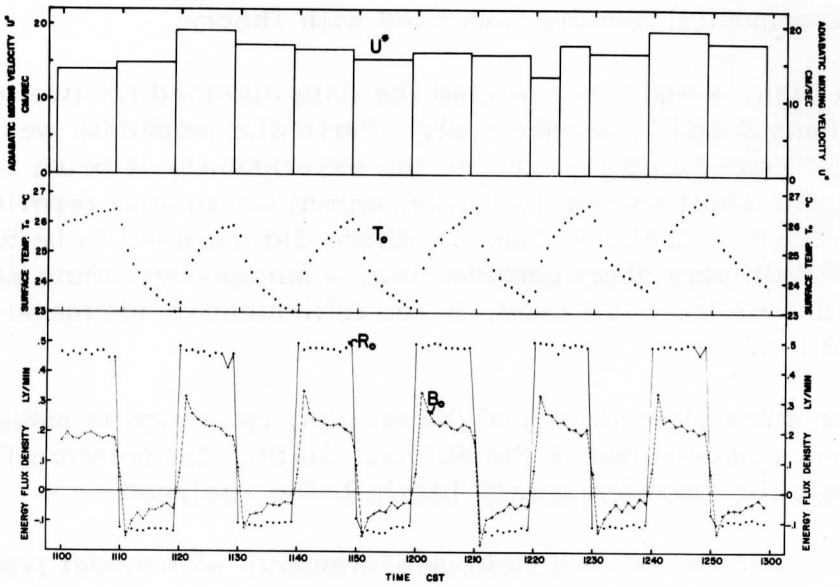

Fig. 4. Data plotted for Run 2, Sept. 2, 1965; six 20 minute periods. A_0 by eddy diffusion measurement was not available. B_0 here was obtained by the combination temperature integral-flux plate method.

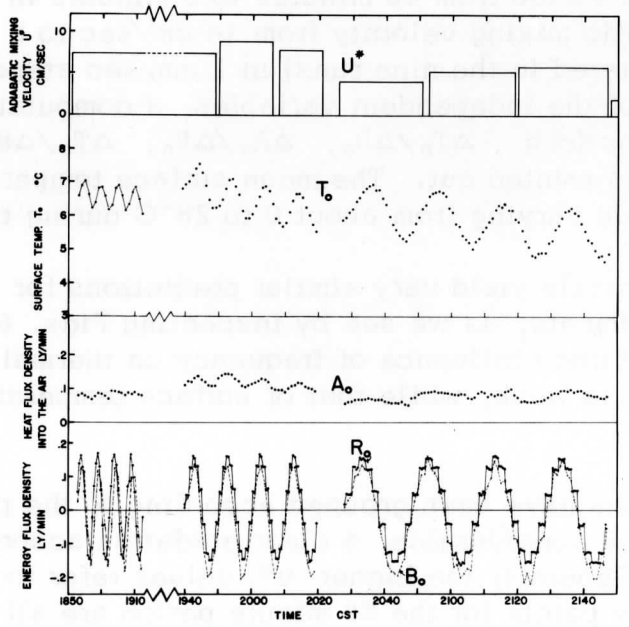

Fig. 5a. (Continued on following page) Data plotted for Run 7, night of Oct. 27-28, 1965. Sequence of periods (in minutes) was: 5-5-5-5, 10-10-10-10, 20-20-20-20, 40-40-40 and 5-5-5-5. A_0 obtained by eddy diffusion equation, B_0 by combination temperature integral-flux plate method.

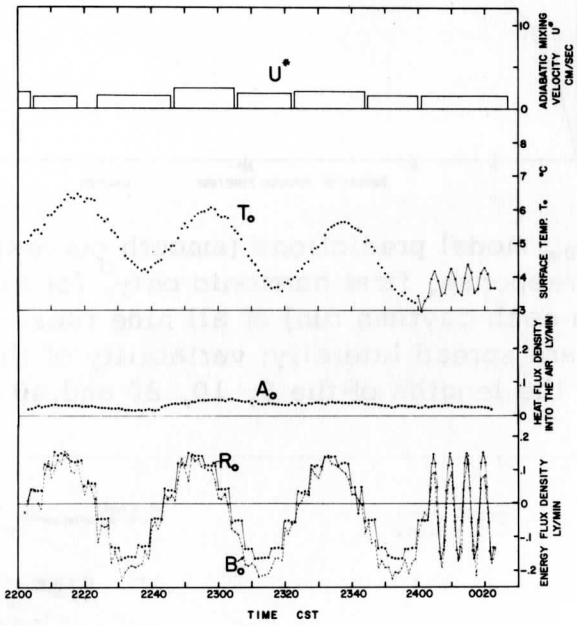

Fig. 5b. (Continued from previous page) 40 minute periods and final 5 minute periods for Run 7.

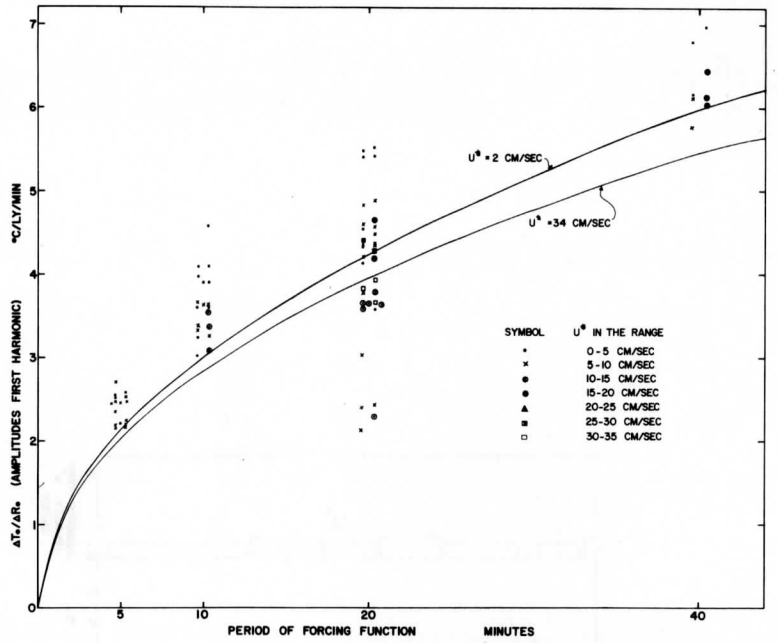

Fig. 6. Based on R_0, model predictions (smooth curves) and observed values of thermal response, first harmonic only, for all periods (except the first one in each daytime run) of all nine runs. For greater clarity, the points are spread laterally; variability of that amount is not implied for the lengths of the 5, 10, 20 and 40 minute runs.

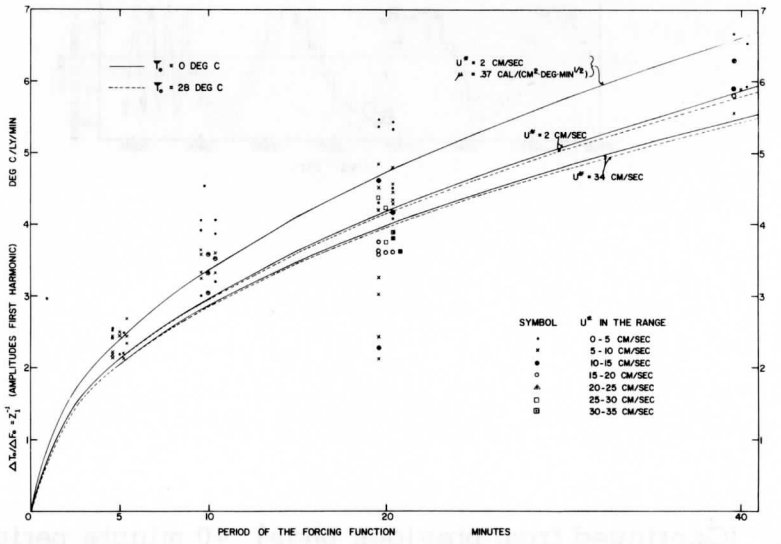

Fig. 7. Based on F_0, model predictions (smooth curves) and observed values of thermal response, first harmonic only, for all periods (except the first one in each daytime run) of all nine runs. The upper smooth curve is for a thermal admittance which is 12% less than was first estimated, in an effort to get a better fit for the data.

The observed points seem to center above the envelope of u^* extremes, suggesting that the originally estimated thermal admittance was too high. Accordingly, after inspection of the graph, a thermal admittance reduced by 12% (0.368 cal/cm^2/deg C/min$^{\frac{1}{2}}$) was used to compute the upper curve in Fig. 7 and a somewhat better fit was obtained. Unfortunately, I cannot be sure enough of a value of μ for the concrete to be able to point definitely to a real departure between observed and predicted values. There are also uncertainties in the measurement of T_0 and R_0, especially the latter, but it is unlikely that they would cause a systematic day and night error of at least 10%. All in all, I propose as a working hypothesis that the originally estimated μ for the concrete was too high by about 10%.

Theory predicts that as the period gets smaller the amplitude ratios $\Delta_i B_0 / \Delta_i R_0$ and $\Delta_i B_0 / \Delta_i F_0$ increase and approach unity. For a 5 minute period and the general range of conditions encountered in these experiments, both ratios are predicted greater than 0.97. But we see that

$$\Delta_i T_0 / \Delta_i B_0 = \frac{1}{\mu (n_i)^{\frac{1}{2}}}$$

Thus, for short periods,

$$\frac{\Delta_i T_0}{\Delta_i R_0} \approx \frac{1}{\mu (n_i)^{\frac{1}{2}}} \quad \text{and} \quad \frac{\Delta_i T_0}{\Delta_i F_0} \approx \frac{1}{\mu (n_i)^{\frac{1}{2}}}$$

and by measuring the thermal response of a surface we can estimate its thermal admittance. Herein lies the possible practical value of short-period shading experiments.

In the case of my data for the five-minute period, where

$$\overline{\left(\frac{\Delta_1 T_0}{\Delta_1 F_0} \right)} \approx 2.3^\circ \text{C/ly/min},$$

μ works out to be about 0.39 cal/cm^2/deg C/min$^{\frac{1}{2}}$.

4. Conclusions and Recommendations

The pattern of thermal response versus period which is predicted by theory was substantially confirmed by observational data. It is likely that the thermal admittance of the concrete was about 10% lower than originally estimated. The presence of a close array of sensors mounted in a plastic framework might well have somewhat distorted the thermal behavior of the concrete.

The data show considerable variability even when classified according to the prevailing u^*. We should note that the u^*'s were averages, obtained over 10 - 29 minutes; any variations in the wind speed within such an interval would produce noise in such measured quantities as T_0 and A_0. There is some suggestion that at very low wind speeds the actual thermal response is greater than theory predicts (but, of course, one of Lettau's restrictions in his first model was that very light winds be excluded).

There are, of course, always uncertainties in measurements of T_0 and R_0, especially so in my R_0 data because they are uncorrected for sensor displacement above the surface. The two models are so close in their predictions of thermal response that it does not seem possible to obtain sufficiently good field experimental data to be able to critically compare their performances in this respect.

Agreement between theory and observation for other amplitude ratios and for phase angle differences (all being referred to either R_0 or F_0) was poor. The data were so irregular that one must, in the first instance, suspect their quality rather than the basis of the theories. Measurement of heat fluxes is always more difficult than measurement of temperature alone. In any future work along these lines, more elaborate means of measuring A_0 and B_0 than I used will certainly be required. The accurate in situ calibration of ground heat flux plates, for instance, is an unsolved problem in micrometeorology. The best approach seems to be via calibration with the temperature-integral method, which itself requires accurate data for the volumetric heat capacity, which in turn is often depth-dependent.

References

Brooks, F. A. (1959). An Introduction to Physical Microclimatology, University of California, Davis, California.

Carslaw, H. S. and J. C. Jaeger (1959). Conduction of Heat in Solids, 2nd ed. Oxford University Press, Oxford, England.

Dalrymple, Paul C., H. H. Lettau and Sarah H. Wollaston (1963). South Pole Micrometeorology Program, Part II: Data Analysis, Technical Report ES-7, Quartermaster R & E Center, Natick, Mass.

Federer, C. A. (1962). Thermal Response of a Dry Surface to Shading Cycles of Short Period, Master's Thesis (Soils), University of Wisconsin, Madison, Wis.

Hamilton, H. L. (1965). Measurements of Infrared Radiation Divergence and Temperature Profiles Near an Air-Water Interface, Final Report, Contract DA-36-039-AMC-00878(E), DA Task IVO-14501-B53A-08, USAERDA, Fort Huachuca, Arizona, University of Wisconsin, pp. 209-259.

Holden, T. S. and J. J. Greenland (1951). The Coefficients of Solar Absorptivity and Low Temperature Emissivity of Various Materials, A Review of the Literature, CSIRO (Australia), Division of Building Research, Report R. 6.

Ingersoll, L. R., O. Zobel and A. Ingersoll (1948). Heat Conduction, McGraw-Hill (rev. ed., 1954, Univ. of Wisconsin, Madison, Wis.)

Lambert, J. L. (1967). The Experimental Investigation of the Thermal Response of a Sumac Canopy, Master's Thesis (Meteorology), University of Wisconsin, Madison, Wis.

Lettau, H. H. (1951). Theory of Surface-Temperature and Heat-Transfer Oscillations Near a Level Ground Surface, Transactions, Amer. Geophysical Union, Vol. 35, No. 1, pp. 121-132.

Lettau, H. H. (1952). Synthetic Climatology, Berichte des Deutschen Wetterdientstes, No. 38, pp. 127-136, Bad Kissingen, Germany.

Lettau, H. H. (1954). Improved Models of Thermal Diffusion in the Soil, Transactions, Amer. Geophysical Union, Vol. 35, No. 1, pp. 121-132.

Lettau, H. H. (1959). A Review of Research Problems in Micrometeorology, Final Report, Contract DA-36-039-SC-80063, Task 65-58-0026, USAEPG, Fort Huachuca, Arizona, University of Wisconsin, Madison, Wis.

Lettau, H. H. (1962). Notes on Theoretical Models of Profile Structure in the Diabatic Surface Layer, Final Report, Contract DA-36-039-SC-80282, USAEPG, Fort Huachuca, Arizona, University of Wisconsin, Madison, Wis., pp. 195-226.

Lettau, H. H. (1966). Problems of Micrometeorological Measurements, Proceedings of a CSIRO Symposium on "The Collection and Processing of Field Data," Canberra 1966; Interscience Pub., J. Wiley, New York, 1967.

Lienesch, J. H. (1961). Experimental Investigation of the Thermal Response of the Air-Soil System to Controlled Radiation Pulses, Annual Report, Contract DA-36-039-SC-80282, USAEPG, Fort Huachuca, Arizona, University of Wisconsin, Madison, Wis., pp. 5-26.

Priestley, C. H. B. (1959). Turbulent Transfer in the Lower Atmosphere, University of Chicago, Chicago, Ill.

Smithsonian Meteorological Tables, 6th rev. ed. (1958). Smithsonian Institution, Washington, D. C.

Stearns, C. R. (1962). Micrometeorological Installation on Lake Mendota, Final Report, Contract DA-36-039-SC-80282, USAEPG, Fort Huachuca, Arizona, University of Wisconsin, Madison, Wis., pp. 7-45.

Stearns, C. R. (1967). Micrometeorological Studies in the Coastal Desert of Southern Peru, PhD Thesis (Meteorology), University of Wisconsin, Madison, Wis.

Super, A. B. (1964). Preliminary Results of Air Mass Modification Study over Lake Mendota, Annual Report, Contract DA-36-039-AMC-00878, DA Task 1-A-0-11001-B-021-08, USAERDA, Fort Huachuca, Arizona, University of Wisconsin, Madison, Wis., pp. 1-21.

Sutton, O. G. (1953). Micrometeorology, McGraw-Hill, New York.

Tanner, C. B. (1963). Basic Instrumentation and Measurements for Plant Environment and Micrometeorology, Soils Bulletin 6, University of Wisconsin, Madison, Wis.

Turner, J. C. (1963). A Thermal Response Experiment on Lake Ice, Master's Thesis (Meteorology), University of Wisconsin, Madison, Wis.

van Wijk, W. R., ed. (1963). Physics of Plant Environment, North-Holland, Amsterdam (distr. Interscience, New York).

van Wijk, W. R. (1964). Two New Methods for the Determination of the Thermal Properties of the Soil Near the Surface, Physica, Vol. 30, pp. 387-388.

Scanner's note:

This page is blank.

TOPOGRAPHIC INFLUENCE ON TORNADO TRACKS AND FREQUENCIES IN WISCONSIN AND ARKANSAS

R. G. Gallimore, Jr., and H. Lettau
Department of Meteorology
University of Wisconsin at Madison

ABSTRACT:

It has been known for some time that tornadoes appear less frequent in mountainous terrain. Furthermore, spatial variations in tornado formation might also be related to surface temperature, as indicated by empirical studies by Kuhn, Darkow and Suomi (1958). The terrain of Arkansas, and the terrain and surface temperature of Wisconsin were investigated by the use of spectral analysis along "strips" of about 100 miles selected on the basis of available tornado statistics. Terrain roughness in scales of 1 to 10 kilometers appear critical to tornado formation and pathlength. Results concerning surface temperature effects on tornadoes are inconclusive. It was found that irregular surface temperature variations in scales from 0.5 to 5 kilometers dominate the spectrum. Dependences on moisture and cloudiness are also noted.

1. Introduction

This study concerns a possible relationship between tornado frequency and topography, as well as the thermal structure of the earth/air interface. Specifically, the distribution of tornadoes in Wisconsin and Arkansas was studied to test the assumption that topography is a significant factor. Detailed information on tornado frequencies can be found in the literature (Flora, 1953). The overriding conclusion is that the seasonal variation of tornado outbreaks depends primarily on the progression of the seasonal storm track. A reduction of frequencies in northern Arkansas and Missouri may indicate suppression by the Ozark, Boston and Ouachita Mountains. Correspond-

ing relationships can be detected by considering detailed tornado and topographic maps like those prepared for Wisconsin by Burley and Waite (1965).

One difficulty with such comparisons, however, must be considered. Namely, tornadoes are reported by people and the lower population in mountain regions may offer partial explanation for a small number of reported tornadoes. Reduced horizontal visibility and less efficient communication in forested, mountainous or hilly areas is an additional factor. Nevertheless, tornadoes leave their marks on the ground for a number of years and many of these will eventually be detected. In this study it is assumed that topography has a real influence which overrides that of a low population density.

2. Arkansas Tornadoes

2.1 Regional and Seasonal Variations of Tornadoes in Arkansas

Since Arkansas has interesting regional variations in tornado development, this state was chosen for a preliminary study of possible terrain effects. Maps published by Asp (1956) and reproduced in Lettau (1967) suggest that there are two distinct tornado "alleys" and two belts with considerably lower frequencies which will be referred to as "shunted" regions. The southern alley lies in the flat Gulf coastal plain while the north-central alley lies in the Arkansas River Valley. The two shunted belts are the Ozark and Boston Ranges located north of the Arkansas River valley and the Ouachita Mountains located in the west central area. Figures 1 and 2 illustrate the typical terrain of these different regions.

2.2 Method of Investigation

2.2.1 Terrain Spectra—The main problem of this study was to obtain a quantitative measure of the specific difference between the alleys and shunted belts. Five strips were chosen in the prevailing direction (or close to it) of the tornado paths. Three of these strips covered the main tornado alleys and the two others the shunted regions. These strips which varied in length from 120-200 miles were then placed on a topographic map of Arkansas (1 to 500,000) with 250 foot contour intervals. Terrain heights were read along these strips at one mile intervals. Portions of three of the resulting terrain profiles are illustrated in Figs. 1 and 2.

The total variance of terrain heights is a significant statistical, numerical parameter for each strip. Spectral analyses of the height-data show the relative contributions of different wavelengths or wave-

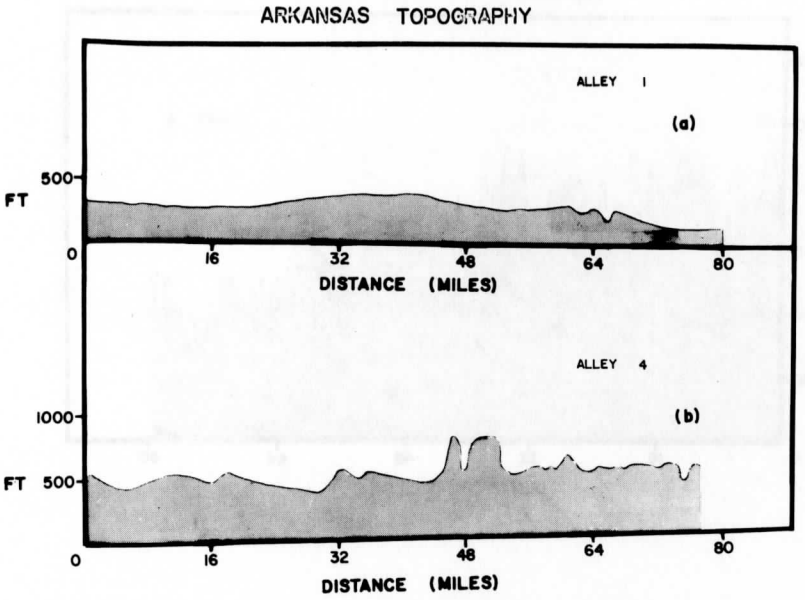

Fig. 1. Terrain profiles in Arkansas tornado alleys. Top profile in Gulf Coastal Plain and bottom profile in Arkansas River Valley.

numbers to the total variance. In order to compare the spectral densities of each strip, estimates were normalized. The range of wavelengths covered in this treatment was 2 to 34 miles (corresponding to wavenumbers from 0.5 to 0.029 cy/mile). A total of 17 lags was used. Aliasing was not a problem in the short wavelengths since height values were smoothed by interpolation between the generously spaced contour intervals. In fact, too much smoothing may have resulted since resolution was not optimum, particularly in the coastal plain.

The results of this spectral analysis will be labeled "Zones 1 to 5" from south to north. Zones 1, 2 and 4 are tornado alleys and Zones 3 and 5 the shunted belts. Figures 1 and 2 illustrate the terrain profiles of Zones 1, 4 and 5, respectively.

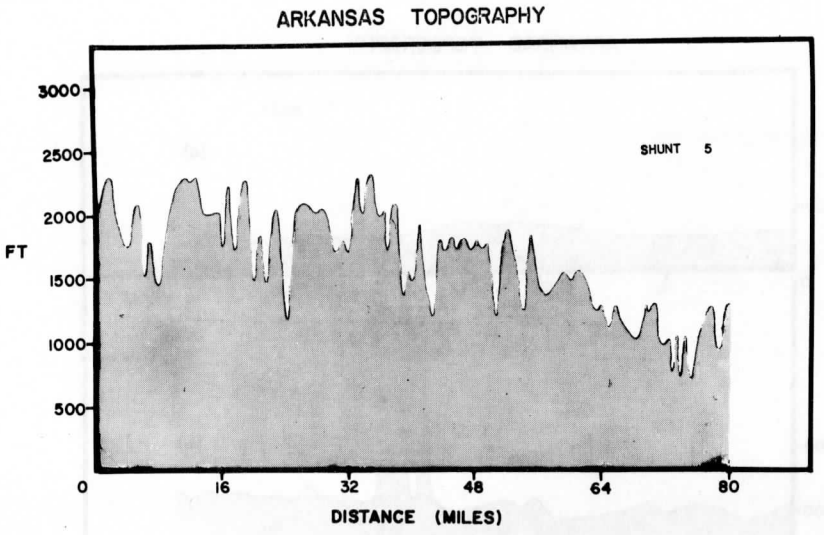

Fig. 2. Terrain profile in Arkansas "shunt region," located north of Arkansas River Valley in the Ozark and Boston Ranges.

2.2.2 Results and Conclusions of Spectral Analysis—The results were plotted on a log-log diagram, with the ordinate being the spectral densities (p) and the abscissa being the wavenumber (k) or correspondingly the wavelength (1/k). In Fig. 3, the spectral densities for tornado alleys can be compared with that for shunted belts. The averages were computed by an arithmetical mean of the log of the estimates. The individual and averaged variances corresponding to Fig. 3 are summarized in Table 1. Averaged standard deviations for shunted belts and alleys are shown in the legend of Fig. 3.

The three spectral graphs of Zones 1, 4 and 5 show significant difference. Although Zones 1 and 4 are in tornado alleys, they exhibit some difference in their spectra. The variances of Zones 1 and 2 are low in comparison with Zone 4 but the shunted belts show substantially higher values. In the smaller wavenumbers (upwards of 10 to 15 mile wavelengths) of Zone 4 the terrain is more like that of Zone 1 while for larger wavenumbers it is more like Zone 5 with more variance than Zone 1.

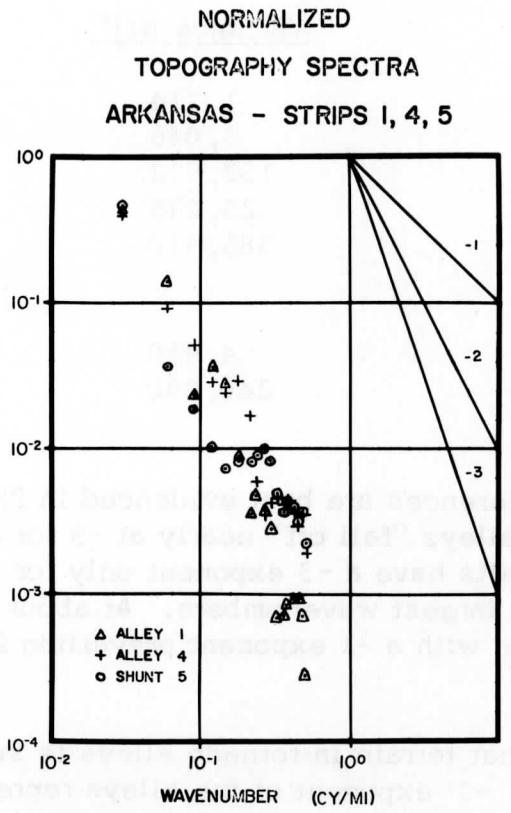

Fig. 3. Normalized spectral plots of Arkansas terrain separately averaged for "tornado alleys" and "shunt regions." Comparative slope lines are indicated in upper right corner. Averaged standard deviations are given in legend. (Averages were computed by averaging the log of the spectral estimates.)

A significant characteristic of a spectrum is the exponent: $n = + d \log p / d \log k$. Its overall numerical value in Zone 4 is near -2 while for Zone 5 it is close to -1 for large wavenumbers and near -3 for small wavenumbers. Zone 1 has a very pronounced exponent of -3 in medium and small wavenumbers. It is apparent that similar tornado alleys may have different terrain characteristics; reference can also be made to the discussion in Lettau (1967, p. 5-7).

Table 1. Variance and Mean of Terrain Height in Arkansas for Tornado Alleys and Shunted Zones. Variance averages were computed logarithmically.

Zone	Variance $(ft)^2$	Mean (ft)
Alley 1	1,714	208
Alley 2	3,046	257
Shunt 3	152,932	660
Alley 4	23,645	489
Shunt 5	386,910	1,387
Averaged Zones		
1, 2, 4 - Alleys:	4,930	318
3, 5 - Shunts:	240,000	1,024

The general differences are best evidenced in Fig. 3; the terrain spectra for tornado alleys "fall off" nearly at -3 for all wavenumbers while the shunted belts have a -3 exponent only for small wavenumbers and possibly for the largest wavenumbers. At about 10 mile wavelength the two plots diverge with a -1 exponent prevailing for the shunted belts.

It is apparent that terrain in tornado alleys is smoother than in shunt regions. The -3 exponent of the alleys represents a rapid decrease in hill size and a correspondingly small change in hill steepness with increasing wavenumbers. This contrasts with the -1 exponent of the shunted belts where a relatively small change in hill size corresponds with a rapid increase in hill steepness for increasing wavenumbers. This suggests that near 10 mile wavelengths, tornadoes frequently are inhibited from either sustaining themselves or possibly even developing. In the overlapping case for a -2 exponent (Zone 4), the terrain does not appear "rough" enough to affect tornadoes. The -3 exponent represents uniform "waviness" and hence not truly a roughness in the aerodynamic sense.

3. Wisconsin Investigation

3.1 Tornado Statistics

3.1.1. The Tornado Season—Quite different from that of Arkansas, main tornado activity in Wisconsin occurs from March to September with peak intensity in May and June, and a secondary peak in September. The most destructive and longest tracked tornadoes occur in the months of

April, May and June. During the secondary peak of September, a southwesterly flow similar to that of Spring appears. In fact, out of 52 severe tornadoes (according to criteria of Burley and Waite, 1965), 42 occurred during September and the Spring months. About 83% of all Wisconsin tornadoes arrive from azimuths between west and south. In July and August, however, many of these storms arrive from the northwest, probably in connection with the frequent northwesterly flow aloft during middle summer. Since the overall synoptic pattern is weak during the summer, the resulting tornadoes are less intense and usually have short tracks.

This study will consider tornadoes which are outstanding with respect to both pathlengths and intensity. This probably biases the data by eliminating a significant portion of the population. Additional bias may have resulted from the fact that the overall number of reported tornadoes has nearly doubled in the last 10 years of a 50 year record.

3.1.2 Distribution of Tornadoes—In Wisconsin the relation between terrain and tornado frequency is not as clear cut as in Arkansas. Fig. 4 shows the number of tornadoes by county from 1916-1964. Tornadoes are of relatively high frequency in most west-central counties, but no distinct north-south variation exists. In some summer situations, extreme eastern counties may be "saved" by cool air off Lake Michigan. Tornado frequency increases towards the west to a maximum in central Iowa. In addition to weather factors, the typically flat or gently rolling, unforested farmland of central and western Iowa which is essentially open plowed fields in the spring probably offers both a relatively smooth and heat absorbing surface favorable for tornado formation, while eastern Iowa and Wisconsin's southwestern counties with forested hills, bluffs and deep river valleys as well as occasional flat ridges seem to reduce tornado activity.

The distribution of outstanding Wisconsin tornadoes particularly the long tracked ones suggests two "alleys"—the rather pronounced "west central alley" and the secondary "southern alley." This west central alley is an extension of the region of large frequency of tornadoes in south central Minnesota. The incidence of tornadoes may be less affected by Wisconsin's unglaciated area than is the ability of these storms to sustain themselves over long distances. In Arkansas, however, there is a significant reduction of tornado incidence in the shunted regions.

3.1.3 Seasonal Migration of Tornado Alleys—The two alleys of Wisconsin appear at different times of the spring season. Monthly information (see Tornado Occurrences in the United States) shows most of the southern alley tornadoes occur in April and May, while

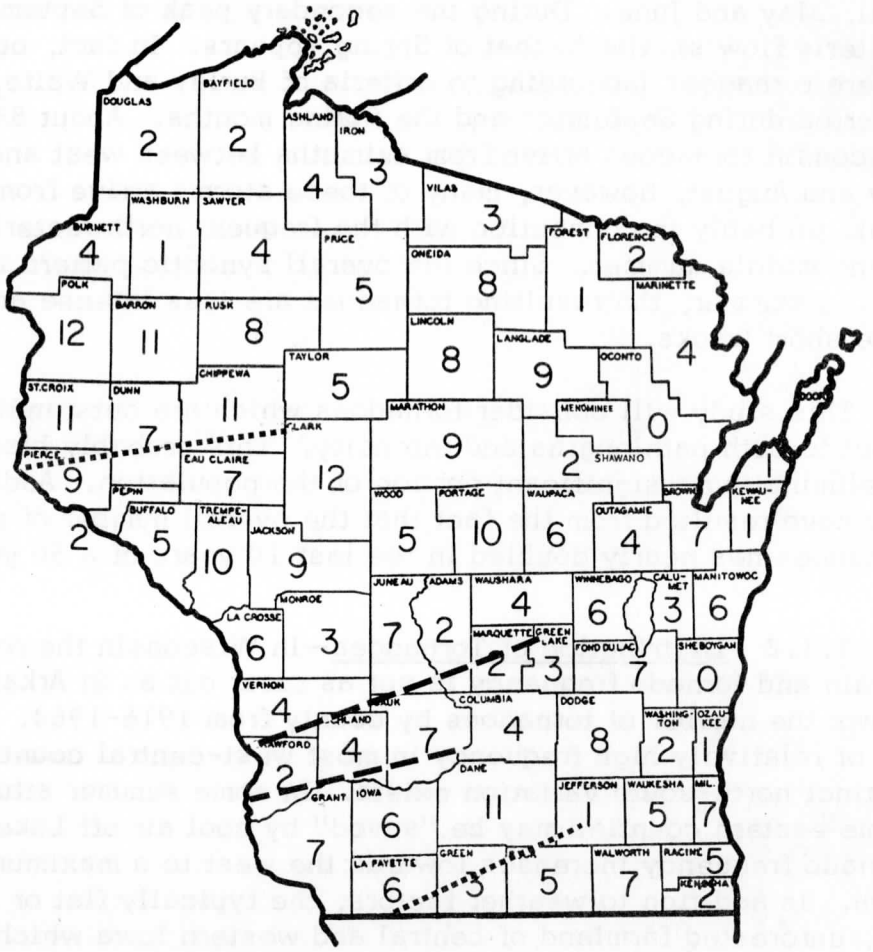

Fig. 4. Number of reported tornadoes by county, 1916-1964 (after Burley and Waite, 1965). Superimposed lines (short dashes for "alleys" A and D, and long dash for "shunted areas" B and C) indicate paths chosen for investigation.

the west central alley is most often frequented in June. In June there is a simultaneous jump in tornado activity in both southern Minnesota and west central Wisconsin. This region of Minnesota is flat open farmland, much like that of central Iowa.

July and August tornadoes seem to show no "alleying," and often move in a southeasterly direction. Unfortunately, July, August and September have too few tornadoes which prohibits further discussion of topographical effects in this direction.

3.1.4 Effects of Population Density—A large majority of Wisconsinites live in the eastern part of the state which contrasts with the higher frequency of tornadoes in the western half of the state. However, a low population density in central Wisconsin prevails just south of the main tornado alley. This sparsely populated area surrounds the forested region including many cranberry bogs just east of the hills near the Mississippi River. Consequently, the lower population in areas between the two alleys requires some qualifying of any terrain-tornado alley relations.

3.2 Method of Study—Topography

3.2.1 Data Collection—Four topographic profiles were chosen. Two of them followed the tornado alleys and the remaining two were in the region of relatively low tornado frequency. All of these strips extended into adjacent states to the west. The profiles were labeled A, B, C and D from south to north; A and D represent tornado alleys while C and B are in the shunted belt. Table 2 gives the geographic locations of these four strips.

Table 2. Geographic Statistical Data of Topographic Profiles in Wisconsin.

Strip	Endpoints	Length (miles)	Variance $(ft)^2$	Mean (ft)
A (Alley)	Anamosa, Iowa - Fort Atkinson, Wisconsin	138	9,036	899
B (Shunt)	West Union, Iowa - Lake Wisconsin	123	24,785	911
C (Shunt)	Decorah, Iowa - Princeton, Wisconsin	141	44,036	1010
D (Alley)	Farmington, Minnesota - Stanley, Wisconsin	121	13,197	963

Initially it was planned to use a radioaltimeter (type AN/APN-22) in a Cessna 310 twin engine aircraft (the same plane employed in previous work at the University of Wisconsin Department of Meteorology—see Lenschow and Dutton (1964)), but the available system was found unworkable. Consequently, the study of terrain profile structure was based on topographic maps. The airplane, however, was useful to measure profiles of surface temperature along the same strips.

Bolometric sampling of surface temperature was done every second which corresponds to one sample every 1/20 of a mile. To ensure comparable detail, terrain heights were taken from 7.5 minute (scale 1 to 62,500) Geological Survey Quadrangles. Because these maps are often only planimetric, a large portion of Wisconsin's shunted belt could not be analyzed. The contour intervals on the topographic quadrangles proved satisfactory for readings at intervals of 1/20 mile. The actual horizontal increment used was 247 feet, or about 79 meters.

3.2.2 Terrain Profiles—For an illustration of terrain structure, heights were plotted in Figs. 5 and 6 every 4,940 feet. As can be seen from Table 2, the variance of height in the shunt region exceeds that of the tornado alleys, but the difference is less pronounced than in Arkansas. Moreover, the variance along the shunted Strip B in Wisconsin is about the same as that of the Arkansas River tornado alley. The location of Strip B appears to be on the fringe of the tornado alley represented by Strip A. If the frequency of tornadoes reported in Wisconsin would be equal to that in Arkansas, Strip B might possibly not be considered typical of a shunted belt. The results of spectral analysis (presented later) bear this out to some degree. Strip C appears more representative of Wisconsin's rugged unglaciated area as well as better centered in a shunted belt than Strip B. However, the terrain variation in this shunted zone is far less than in Arkansas. The fact that some active tornadoes do indeed track over this area does imply a weaker relation between shunted belts and terrain roughness than is apparent in Arkansas.

The terrain height profiles show some interesting features. Different from the other profiles, D has relatively larger height variation in very long wavelengths. This implies that "Alley D" is relatively smoother than the other strips at short and medium wavelengths. The flat terrain west of the Wisconsin portion of D coincides with a notorious region of tornado activity during June.

3.2.3 Terrain Slope—Figure 7 illustrates profiles of terrain slope averaged over 5.6 miles, for strips A, B, C and D. The positive sign is used when terrain rises towards the east. The "Shunt Strips" B and C show considerable oscillation between positive and negative values and both have a large negative mean. C shows a gradual downslope to the east while slope values of B are more like that of A but with higher amplitude. While A has a small average downslope, D has mean upslope due to the terrain rise east of the Mississippi River and that east of the Chippewa River.

Figure 7 suggests that tornadoes tend to shy away from varying slopage, i.e., terrain roughness, and downslope. The positive relation of

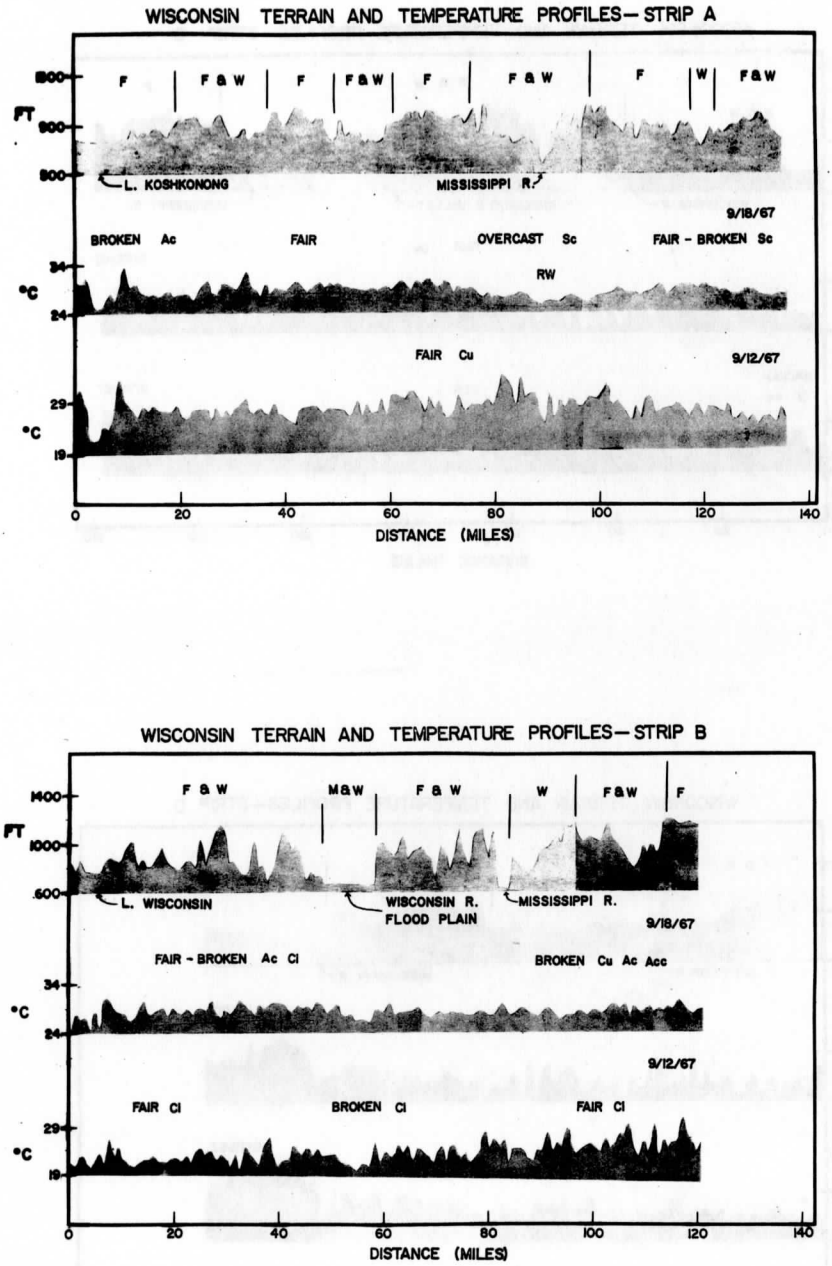

Fig. 5. Terrain and surface temperature profiles of September 12 and 18, 1967, for Wisconsin Strips A and B (top is A). A few landmarks and a general description of the characteristic surface and sky conditions is also given. (Note M = marshland, F = open field and farmland, and W = woodland.)

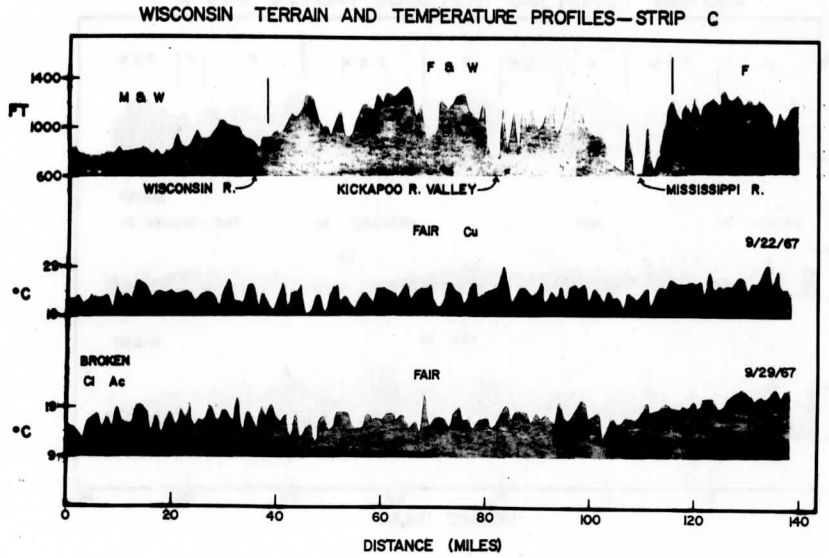

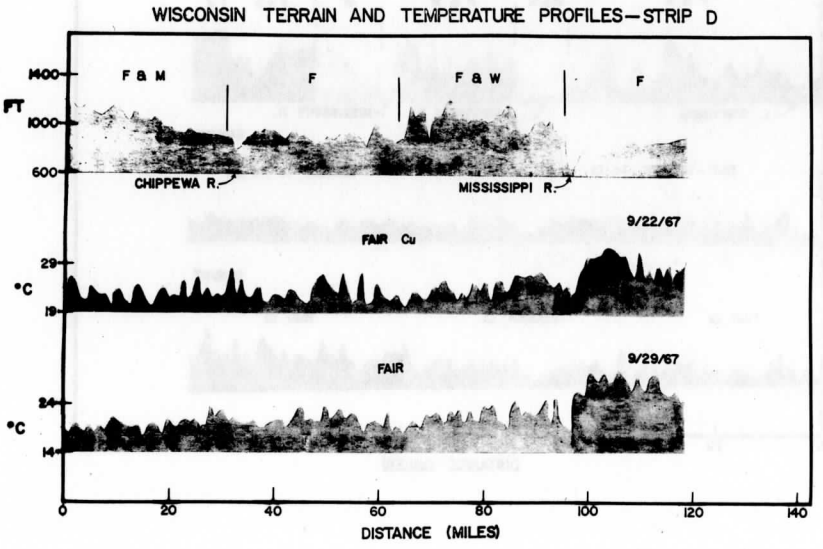

Fig. 6. Terrain and surface temperature profiles of September 22 and 29, 1967, for Wisconsin strips C and D (Top is C). A few landmarks and a general description of the characteristic surface and sky condition is also given. Note: M = marshland, F = open field and farmland, and W = woodland.

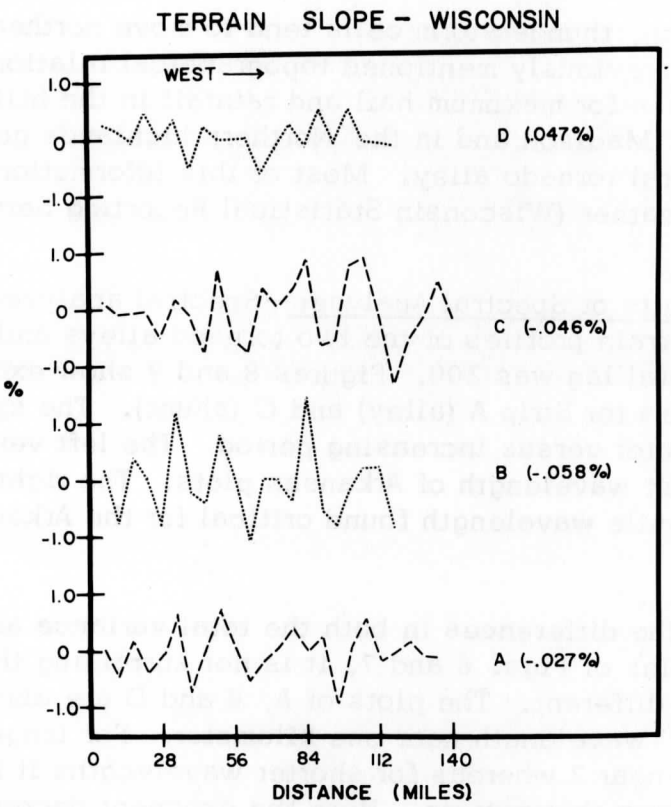

Fig. 7. Wisconsin terrain slope for Strips A, B, C and D given in percentage (positive for upsloping to the east) over 5.6 miles. The mean slope is indicated to the right of the corresponding strip.

tornado frequency with upslopes toward the East may further be enhanced by middle and late afternoon heating.

If the above conclusions are acceptable, tornado frequencies depend on somewhat different mechanisms than other convective phenomena. Hail and heavy rainfall are also known to be dependent on terrain slope, elevation, roughness and woodlands. Hail intensity not only appears positively related to upslope, but, differently from tornadoes, is positively related to downslope, roughness and woodlands (Stout (1962)). Stout noted the relation with downslope may be due to a release of hail by decreased positive vertical motion and lateral divergence.

Rainfall patterns show a similar relationship except that downslopes likely reduce convective instabilities and hence reduce thunderstorm rainfall.

During spring, thunderstorm cells tend to move northeasterly which, considering the previously mentioned topographical relations, appears to be the main reason for maximum hail and rainfall in the hilly areas west and northwest of Madison and in the Northern highlands generally north of the west central tornado alley. Most of this information can be found in Wisconsin Weather (Wisconsin Statistical Reporting Service, 1967).

3.2.4 Results of Spectral Analyses—Spectral analyses were performed on the terrain profiles of the two tornado alleys and two shunt regions. The total lag was 200. Figures 8 and 9 show examples of individual spectra for Strip A (alley) and C (shunt). The spectra were plotted by computer versus increasing period. The left vertical line indicates the Nyquist wavelength of Arkansas plots. The right vertical line is along the 10 mile wavelength found critical for the Arkansas shunted belts.

In view of the differences in both the total variance and the structure of the profiles of Figs. 6 and 7, it is not surprising that the spectral graphs are also different. The plots of A, B and D are almost identical with a "critical" wavelength near one kilometer. For longer wavelengths the exponent is near 2 whereas for shorter wavelengths it is close to 3. Strip C differs from this pattern. Here the exponent decreases continuously for decreasing wavelengths starting near 2 and gradually changes to zero for wavelengths less than one kilometer. Short wavelengths contribute more variance in C than in A, B and D.

In the 2 to 20 mile wavelength band, the spectra for A, B and D were similar in nature to that of the Arkansas River Valley which has a total variance reasonably close to these 3 strips. The exponent is about 2. In marked contrast, C has a spectral variance in this band much like the shunted belts of Arkansas. Its total variance, however, is considerably smaller than either of these belts but larger than the other Wisconsin strips. Due to the difference in contour interval size for the Arkansas and Wisconsin study, we cannot say how realistic this comparison is.

Spectral estimates for the two tornado alleys and the two shunted strips were separately averaged and are illustrated in Fig. 10. Since the B spectrum resembles more that of A than C, averaging B with C yields a plot which possibly is not representative of the shunted belt of Wisconsin. A better choice for the location of a shunted strip would probably have run from La Crosse into northern Juneau and Adams counties, but topographic maps were not available for this region.

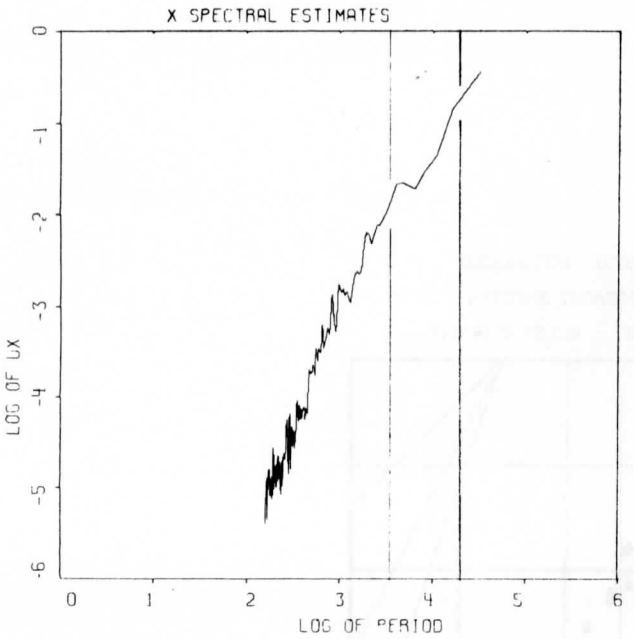

Fig. 8. Normalized terrain spectrum of Wisconsin, Strip A (tornado alley). Vertical lines represent 2-10 mile spectral band covered in Arkansas spectral analysis.

Fig. 9. Normalized terrain spectrum of Wisconsin, Strip C (shunt). Vertical lines represent 2-10 mile spectral band covered in Arkansas spectral analysis.

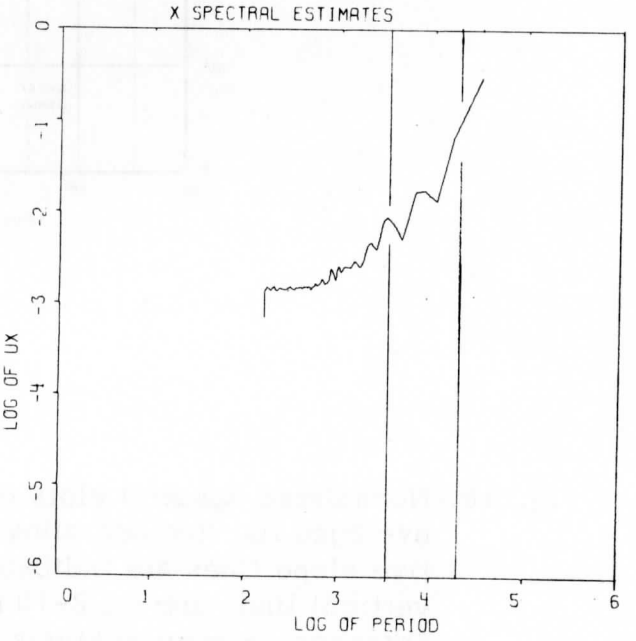

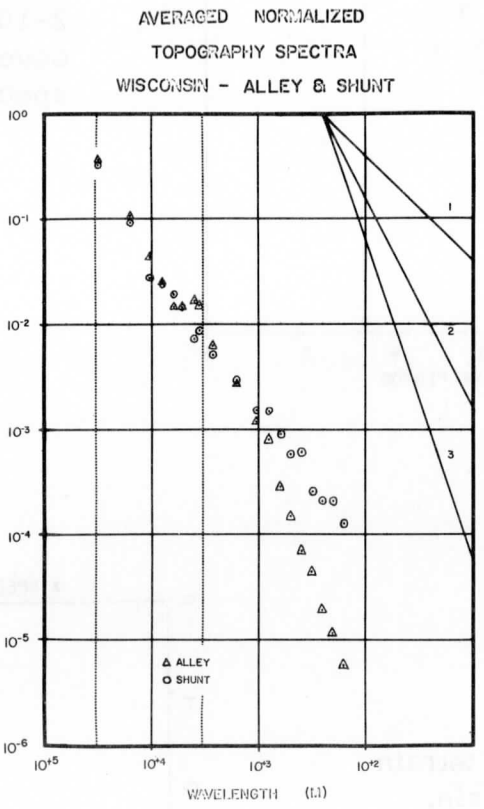

Fig. 10. Normalized spectral plots of Wisconsin terrain separately averaged for "tornado alleys" and "shunt regions." Comparative slope lines are indicated in upper right corner. The two vertical lines are the 2-10 mile wavelength band covered in Arkansas spectral analysis. (Averages were computed by averaging the log of the spectral estimates.)

A discontinuity in the spectra appeared at a wavelength of about one kilometer. The exponent is near 1 for the shunted belt and near 3 for the alleys. For longer wavelengths, including the 2 to 20 mile wavelength band, both graphs suggest an exponent of 2. Referring back to Section 2.2.2, the exponent of 1 implies increasing hill steepness and fairly uniform hill size with decreasing wavelength while an exponent of 3 indicates a more uniform hill steepness with decreasing wavelength. The fact that the split appeared near one kilometer instead of around 10 miles (found critical for Arkansas) could be the result of more detailed data collection in Wisconsin.

The near-zero exponent for short wavelengths (< 1 km) of C suggest rapid steepening of slope with decreasing base length of the hills. It would be interesting to know if this is typical of other shunted areas like those of Arkansas. Furthermore, a critical wavelength around 10 miles is of the scale of thunderstorms. On the other hand, a critical wavelength near one kilometer is of the order of tornado size. This might suggest that only tornadoes and not thunderstorms are significantly affected by topography in Wisconsin.

3.3 Surface Temperature

3.3.1 Instrumentation—Surface temperature was measured along the four terrain profiles shown in Fig. 4 with the aid of a Barnes IT-3 Infrared Thermometer or Bolometer mounted in the baggage section of a Cessna 310 twin engine aircraft. This bolometer has a 3° field of view corresponding to a circle of about 15.7 meter radius at 300 meters above the ground. The measurement technique is the same as described by Lenschow and Dutton (1964).

Before each flight, a pre-check of the system was made with water baths of varying temperatures. Check flights over Lake Mendota were also included on the day of a run. This was done to insure proper functioning of the instruments when airborne. Sometimes the bolometer indicated a fictitious rise of about 1° C of the Lake Mendota temperature after considerable time in the air but such discrepancies were judged insignificant. Although all instruments were shock mounted, some vibrational noise still occurred and the filter was used to remove it for spectral analysis of the temperature data. The use of this filter, however, introduced some additional problems that will be discussed later.

3.3.2 Measurement of Surface Temperature from an Airplane—According to Stefan-Boltzman's law, radiation emitted by a surface depends on both its emissivity and its temperature. Since emissivity varies over different surfaces, errors will be introduced regardless of the accuracy of the calibration. An 8% change in emissivity corresponds

to about a 6° C change in measured surface temperature (Lenschow and Dutton, 1964). Except in dry sandy areas, variations as large as 8% in emissivity are not likely in Wisconsin.

Radiation entering a bolometer depends on the radiation emitted by the environment when the emissivity of the surface is not unity. For the bolometer used, the radiometer filter was an 8 to 14 micron passband with nearly zero response outside. Square band pass filters between 8 and 14 microns vary little with temperature. For the type of surfaces encountered in Wisconsin, the emissivity was assumed nearly constant for all wavelengths in the band pass of the filter. Errors resulting from this assumption can be reduced if the surrounding radiation is as small as possible. Using the conditions listed above, Tanner and Fuchs (1966) showed that the equivalent black body temperature departs from the actual surface temperature by less than 1° C for Sudan grass ($\varepsilon = 0.976$) and alfalfa ($\varepsilon = 0.977$). However, Lorenz (1966) noted that for an emissivity of 0.925, the difference could be as large as 3.5° C. In general, the apparent surface temperature is sufficiently close to the actual radiation surface temperature provided the bolometer is not located far above the ground. Lenschow found the measured radiative temperature to be within 3.5° C of the actual surface temperature when the surface and air temperatures for an isothermal layer 300 meters thick differed by 20° C. This estimate was based on typical optical depths of water vapor and CO_2 for later summer and early fall. Menon (1967) also discussed surface temperature corrections for flights over Lake Michigan and Lake Superior. He found that errors of $\pm$ 0.5° C can be expected without corrections at 300 meter heights.

Table 3 summarizes the results of the calibration flight over Lake Mendota on August 21, 1967; a comparison of bolometric water temperature (T_b) with the lake temperature measured from a boat (T_w) showed a difference of about 0.5° C at 300 meters. The dew point was relatively high. As expected, the measured temperature decreases with height.

It should be pointed out that the bolometer "sees" an area (for our flights) of about 776 m^2. It records an average radiation temperature over this area that tends to be larger than the true area mean surface temperature. Lenschow and Dutton (1964) discuss this problem and found such errors to be less than 1° C which was considered tolerable for this investigation.

3.3.3 Data Collection—The total Visicorder temperature trace was read (for the same number of points as the terrain height data) by a specially designed chart reader and automatically punched on data cards, and transformed into surface temperature with the aid of a linear equation.

Table 3. Results of Bolometric Flight over Lake Mendota on August 21, 1967. T_a is the air temperature measured from airplane, T_b is bolometric water temperature, T_w is water temperature measured from a boat. Simultaneous recordings at Truax Field showed a dry-bulb temperature of 21° C and a dew point of 15° C.

Height (ft.)	T_w	T_b	T_a
0	21	-	-
500	-	22	23
1000	-	21.5	22
1500	-	21	20.5

3.3.4 Effects of Soil Moisture, Sky Condition and Wind on Surface Temperature. Of a total of 14 flights, five (4 near noon and one at dawn) were over strips A and B, two were over strip C near noon, and two were over strip D in the early afternoon. Table 4 lists the resulting means and variances as well as the time and date of each flight. It should be noted that the effect of the 5-sec filter is to reduce the variance but not to alter the mean of the actual surface temperature series. Temperature profiles were included in Figs. 5 and 6 together with the general characteristics of the terrain "landmarks" and sky conditions.

The day-to-day variation in surface temperature is due to changes in insolation (which depends on cloudiness, season, latitude, etc.), albedo, emissivity, wind (speed and prevailing direction), thermal admittance of the soil, and air temperature and moisture gradients. Significant daily (and diurnal) variations in some of these parameters occur even when the same air mass prevails over a region for several days. The days chosen to measure the surface temperature were selected with the intent to isolate some of the dominant parameters. Tables 5, 6 and 7 provide information on precipitation, air temperature, wind and total insolation for the days and regions.

The difference between moist and dry surface conditions is illustrated by comparing the profiles of September 12 and 18 for Strips A and B. Due to preceding rainy days, the overall variation on the 18th is relatively small. Reduced insolation due to overcast cloudiness also will significantly damp out temperature variability. In general, flights were scheduled only when cloudiness was expected to be light, but, unfortunately, in view of the oncoming of autumn, this requirement was often relaxed. The flight of September 18 over Strip A was under heavy cloudiness and showed reduced surface temperature. Several examples—notably October 5 of Strip A, September 12 of Strip B and September 18 of Strip A—illustrate how periods of overcast cloudiness can induce long "trending" in the surface temperature record.

Table 4. Mean temperature and variance (deg C) from bolometric flight over the four "Strips" in Wisconsin indicated on Fig. 4

Date 1967	STRIP A		STRIP B		STRIP C		STRIP D	
Sept. 11	10:50-11:38	23.1 ± 3.9						
12	12:47-1:35	27.8 ± 3.9	10:40-11:25	24.7 ± 5.4				
18	1:14-2:03	27.3 ± 2.0	2:27-3:11	27.6 ± 1.1				
21			11:34-12:13	25.3 ± 0.9				
22					11:44-12:34	23.6 ± 3.3	2:43-3:25	24.3 ± 8.7
29					11:41-12:32	17.3 ± 4.5	2:12-2:52	22.3 ± 10.6
Oct. 2			12:28-1:14	27.3 ± 3.3				
3			6:36-7:26	15.7 ± 1.9				
5	6:36-7:10	13.1 ± 2.2						
5	12:24-1:11	22.8 ± 1.9						

Table 5. Averaged Maximum Air Temperature for Three Climatological Stations (see Table 7) located near respective strips.

Date 1967	Strip A (°C)	Strip B (°C)	Strip C (°C)	Strip D (°C)
Sept. 11	21.3			
12	24.3	24.8		
18	26.7	26.7		
21		23.0		
22			20.2	19.4
29			12.6	15.6
Oct. 2		27.9		
3		13.0*		
5	9.6*			
5	27.1			

*Value of averaged minimum air temperature

Table 6. Partial Summaries of Weather and Climatological Data Pertinent to Bolometric Flights. Value in parentheses are maximum wind speeds during the day.

Date 1967	Average Resultant Wind				Insolation (ly/day)	
	Madison		Minneapolis		Madison	La Crosse
	Direction	MPH	Direction	MPH		
Sept. 11	140	7.3 (15)			464.6	514.0
12	170	5.7 (16)			461.0	436.5
18	120	2.6 (14)			344.1	294.9
21	320	9.6 (22)			398.3	444.0
22	030	3.9 (9)	180	8.2 (17)	465.1	450.0
29	330	8.8 (15)	170	1.7 (7)	249.0	440.4
Oct. 2	200	9.9 (20)			414.9	397.3
3	200	5.6 (9)			347.0	342.6
5	020	7.8 (14)			398.4	389.9

Table 7. Precipitation totals (inches) are for: 1. Fort Atkinson, 2. Broadhead, 3. Platteville, 4. Prairie du Sac, 5. Richland Center, 6. Prairie due Chien, 7. Montello, 8. Hillsboro, 9. Genoa Dam 8, 10. Stanley, 11. Menomonie, 12. Ellsworth. No precipitation fell during September 1 - 8.

Date 1967	DAILY PRECIPITATION TOTALS											
	A			B			C			D		
	1	2	3	4	5	6	7	8	9	10	11	12
Sept. 9	.10											
12												T
13											.94	.42
14	.06	.14	2.36	1.65	1.48	1.42	.57	.58	.56	.94	.75	.38
15	.08	1.30	2.69	.63	2.40	1.14	1.90	2.15	.87	.37	.20	T
16	.16	.70	.02	T	.01	.05		.06				
17	.36	.03	T									
18			.01									
19		T	.11	T								
20		.10	.10	.21	.18	.08	.07	.18	.12	.46	.01	.03
21	.61	.06			.06	.30		.04		.05	.06	
23										.01		
26		.03	.35	.16	.08	.37	.06	T	.09		.01	.04
27	.67	.52							.10			T
Oct. 4			T				T					.03
5	.02		T		.02				.02			

Table 5 gives the average maxima air temperature of the same locations listed in Table 7. On a given day when the soil was wet, the mean surface temperature was relatively close to the average maximum air temperature of the nearest climatic stations. The mean surface temperature was found generally higher than the air temperature for fair skies and relatively dry soils. The two dawn flights (October 3 and 5) show mean surface temperatures higher than the average minimum station temperature. The variance was also found fairly high indicating that warmer ground inversions were probably being measured as part of the effective radiative surface. Temperature trends under variable conditions appear to substantiate Lambert's investigation of thermal response of a Sumac canopy (1967) to cloud shadows.

Table 6 shows lowest average windspeeds on the 18th (Madison) and 29th (Minneapolis) of September. The larger surface temperature variations on the 29th as opposed to the 22nd probably resulted from drier soils and low wind speeds. The 18th and 21st appear to have sufficiently identical soil and sky conditions that the large difference in average wind speed may in fact be the cause of the lower variance of the latter. It should be noted that the times of these two flights differed by about 3 hours. Obviously, the available information was insufficient to determine the full effect of air motion on surface temperature.

3.3.5 Influence of Land Use and Surface Types—Figures 5 and 6 provide a rather general description of the distribution of surface types along the strips. Farmland plots and irregular spaced forests will respond differently to solar heating. The selected interval (4940 ft) for plotting of the temperature profiles can only crudely express these effects. Considering that rainfall and cloudiness affected most of the samples taken along Strip A and B, this discussion will be primarily concerned with Strips C and D.

The relatively high surface temperatures west of the Mississippi River over Strips C and D are in areas of extended, harvested fields of brown color. High readings also occurred in other regions of dominantly open farmland. The lowest average mid-day temperatures generally appeared in the marshy and scrubby vegetated areas. Mixed areas both flat or hilly showed considerable variation but have on the average a mean temperature between that of farmland and marshy land. The relatively high surface temperatures observed near the Mississippi River along Strip A is over a region with some hills but is less forested than either B or C. In essence, these findings agree with the results reported by Lenschow and Dutton (1964) for central and southern Wisconsin.

The total amount of surface data was unfortunately too small to establish conclusively differences between tornado alleys and shunted strips. Several factors can be mentioned: First, the period studied did not coincide with the maximum tornado season, while the surface structure, both in open and forested areas, varies seasonally; for example, deciduous forests are leafless during April and early May, cornfields are bare in spring but not in late summer and fall, whereas for hay and wheatfields the reverse is true. A relatively warm strip of nearly 20 miles (Fig. 6) in Minnesota is interesting and will require further study, because this region is one of high tornado incidence in June; the high variance of strip D (Table 4) is probably connected with this warm area. Secondly, warm regions of smaller scale (several miles or less) appear rather frequently and might imply randomness of convection phenomena. Thirdly, a portion of the variances of several of the days were influenced significantly by cloudiness and soil moisture. More information is needed on surface temperature response under varying weather conditions before inferences on relationships between temperature structure and tornadoes is determined.

3.3.6 Computation of Variance Spectra—Spectral analysis was performed on the surface temperature data in the same manner for the topographic data. Smoothing of the terrain data was a natural result of the topographic maps. The effect of filtering on the measured surface temperature had to be considered in more detail. The Barnes bolometer has a 3° view and consequently averages over a circular area of 15.7 meter radius which may increase the exponent at the high frequency end of the spectrum. This form of smoothing of temperature and the contour smoothing of the terrain data probably eliminated some aliasing problems. Second, a 5-sec filter was used to help prevent aliasing also, but because it damped out important amplitude variations in intermediate wavelengths, the unfiltered spectral estimates had to be recovered, following a method described by Dutton (1962).

3.3.7 Conclusions from Temperature Spectra—A test was conducted to compare the red noise spectrum against the actual spectra. For a detailed discussion of "red noise spectra" see Gilman, et al. (1963). In particular, for a "null" hypothesis the "red noise" was considered the underlying continuum or actual population from which the direct estimates were just random samples. A plot of the "red noise" estimates corresponding to September 22 of Strip C is given in Fig. 11. Red noise spectra for the other dates were similar. To test this continuum against the sample plot, it is assumed that the ratio of the sample estimate to the continuum estimate is a chi-square variable divided by the number of degrees of freedom. In this way, a confidence (acceptance) region can be specified about each continuum value according to Tukey. The estimates of September 22 differed significantly from the red noise continuum at the 5% level

of significance. The sample curve appears to follow simple persistence in short (< 600 meters) and long wavelengths while the intermediate wavelengths show a white noise shift. Many of the other spectral graphs also show this tendency.

To test further, lines were placed by sight (regression lines would deviate little from this) through the short and intermediate period regimes. Figure 12 illustrates a pair of such lines as well as the confidence limits pertinent to Strip A of September 11. The regimes of simple persistence and near white noise are well contained inside these confidence limits. Numerous spikes and overall noisiness in the direct spectra appear to be statistically insignificant. However, more data would be needed to verify the validity of this statement. Recurring spikes over an individual terrain profile might indeed prove physically real.

The results above indicate that by and large, the intermediate "waves" of 0.5 to 5 km are made up of a random distribution of temperature oscillations. This seems reasonable considering that the arrangement of forests, lakes, towns and variable crop and pastureland are of the order of intermediate wavelengths and tend to be fairly irregular in nature. These are the dominant homogeneous features that man has divided the land into. As dominating features get smaller, the temperature response decreases rather rapidly.

One important exception was found on September 18 over Strip B where a gradual decrease with exponent less than 1 was suggested. Considering the wet soil and extensive cloudiness present on September 18, the damping of major randomness in intermediate wavelengths is not surprising.

For the terrain spectra previously discussed, a comparison was made with the red noise spectrum. Figure 13 illustrates the red noise spectrum corresponding to Strips A and C. The topography of A, B, and D all have a high degree of simple persistence while "white noise" in smaller wavelengths of C causes substantial deviation from red noise, although some persistence in long wavelengths may prevail. Most of these conclusions were substantiated in Section 3.2.4.

4. Concluding Remarks

The results of this study seem to pose more questions than answers. The qualitative picture of tornadoes shying from "rough" terrain does not explain how the terrain affects these storms. We must try to understand roughness on a quantitative scale. This has been attempted through

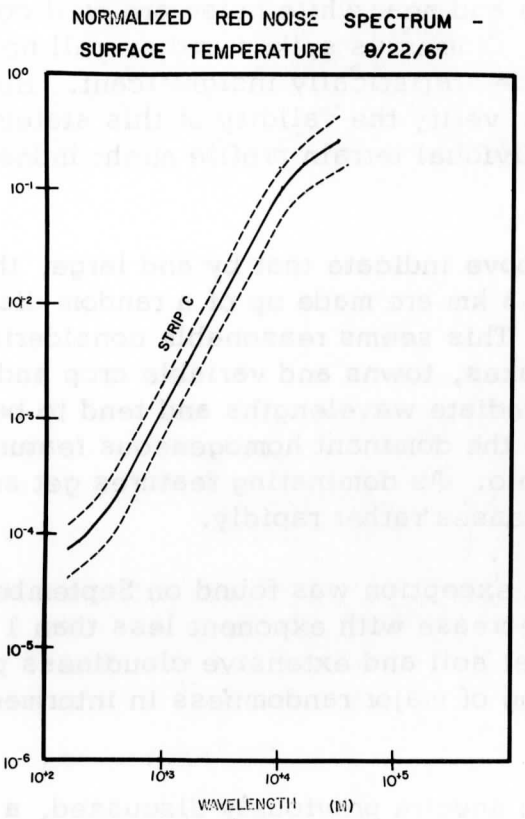

Fig. 11. Red noise spectrum of surface temperature corresponding to September 22, 1967, of Wisconsin Strip C ("shunted strip"). Estimates based on a sample one lag autocorrelation coefficient (r_1) equal to 0.9697. Chi-square confidence lines are given in dashed curves.

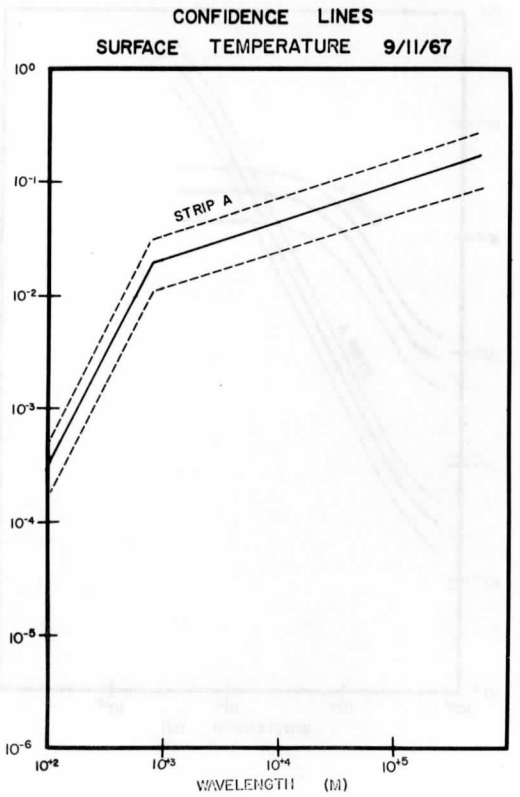

Fig. 12. Lines placed by sight, fitting spectral curve of a surface temperature for September 11, 1967, of Wisconsin Strip A ("tornado alley"). Confidence lines are also indicated.

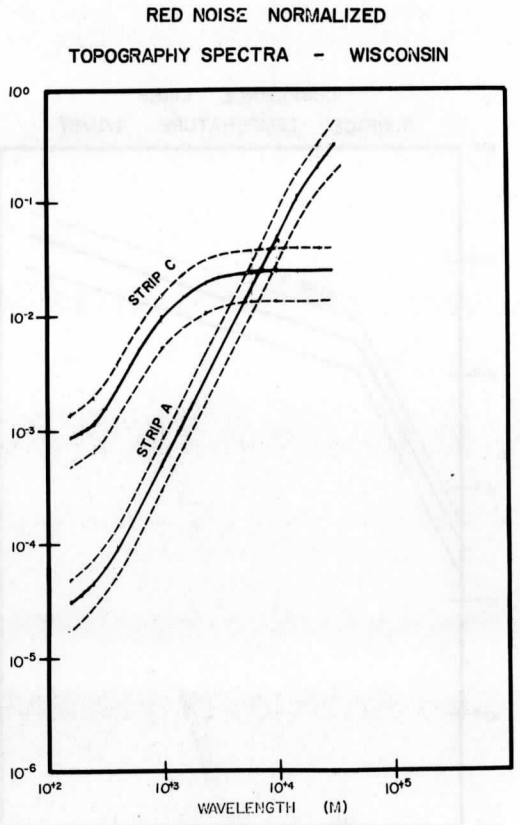

Fig. 13. Red noise spectra corresponding to terrain of Wisconsin Strips A ("tornado alley") and C ("shunt strip"). Estimates were based on one lag autocorrelation coefficients 0.9874 and 0.7078 respectively for Strips A and C. Chi-square confidence lines are also given.

the use of spectral analysis for selected terrain profiles. In order to measure roughness over a region, a two-dimensional approach will be needed to determine the full variability of surface structure.

Surface temperature is one measure of how a surface type responds to insolation, but the daily and hourly variation in the many factors governing thermal response makes it difficult to specify a tornado and non-tornado area in the mean. One possible approach would be to parameterize conditions for each "mosaic" element of a complex land/air interface like that in Wisconsin and develop a theoretical model of thermal response to radiative forcing functions, as that of "climatonomy" proposed by Lettau (to be published). Full parameterization of surface conditions must include a measure of aerodynamic roughness, of albedo and emissivity, of moisture availability—such as the Bowen ratio—and the thermal admittance of the submedium. This study provided new information on surface roughness and its effect on surface temperature variability. Considering that features smaller than 600 meters appear less significant to surface temperature variations, the task may not be overwhelming.

Very little is known about how local supplies of sensible and latent heat are utilized in severe convective storms. Mesoscale meteorology has not had the benefits of intensive research that larger scale studies have. Even less is known on the generation of hail and tornadoes. Further research of the basic dynamics and energetics of the mesoscale is certainly needed.

References

Asp, M. O., Geographical Distribution of Tornadoes in Arkansas, Monthly Weather Review, 84(4): 143-145, 1956.

Burley, M. W. and P.J. Waite, Wisconsin Tornadoes, Transactions of the Wisconsin Academy of Science, Arts and Letters, Madison, Wis., 1965.

Dutton, J. A., Space and Time Response of Airborne Radiation Sensors for the Measurement of Grand Variables, Journal of Geophysical Research 67(1): 195-204, 1962.

Flora, S., Tornadoes of the United States, University of Oklahoma Press, Norman, 1953.

Gilman, D. L., F. G. Fuglister and J. M. Mitchell, Jr., On the Power Spectrum of "Red Noise," Journal of Atmospheric Science 20: 182-184, 1963.

Holloway, J. L., Jr., Smoothing and Filtering of Time Series and Space Fields, Advances in Geophysics 4: 351-389, Academic Press, New York, 1958.

Kuhn, P. M., Darkow, G. L. and Suomi, V. E., A Mesoscale Investigation of Pre-tornado Thermal Environments, American Meteorological Society, Bulletin 39(4): 224-228, 1958.

Lambert, J. L., The Experimental Investigation of the Thermal Response of a Sumac Canopy, Master's Thesis (Meteorology), University of Wisconsin, 1967.

Lenschow, D. H., and J. A. Dutton, Surface Temperature Variations Measured from an Airplane over Several Surface Types, Journal of Appl. Meteorol., Vol. 3, pp. 65-69, 1964.

Lettau, H., Small to Large-Scale Features of Boundary Layer Structure over Mountain Slopes. Proc. Symposium on Mountain Meteorology, Fort Collins, Colorado, Colorado State University, Dept. Atmosph. Sci., 1967, Paper No. 122, pp. 1-74.

Lorenz, D., The Effect of the Long-wave Reflectivity of Natural Surfaces on Surface Temperature Measurements Using Radiometers, Journal of Appl. Meteorol., 5(4): 421-430, 1966.

Menon, V. K. and Ragotskie, R. A., Remote Sensing by Infrared and Microwave Radiometry, Technical Report No. 31, Task No. NR 387-022, prepared under ONR contract No.: 1202(07), University of Wisconsin, 1967.

Stout, G. E., Factors Influencing the Climatological Distribution of Hail in Flatlands, Nubila, V(1): 73-84, 1962.

Tanner, C. B. and M. Fuchs, Infrared Thermometry of Vegetation, Agronomy Journal 58: 597-601, 1966.

Wisconsin Statistical Reporting Service publication, Wisconsin Weather: Causes, Variations, and Effects, Madison, Wisconsin, 1967.

Wolford, L. V., Tornado Occurrences in the United States, U.S. Department of Commerce, Technical Paper No. 20, 1960.

Scanner's note:

This page is blank.

6

THE THEORY OF VARIANGULAR WIND SPIRALS

H. Lettau and W. F. Dabberdt
Department of Meteorology
University of Wisconsin at Madison

ABSTRACT:

A new concept in wind spiral theory—the variangular spiral—is introduced. A number of earlier solutions to the problem of mean air motion within the planetary boundary layer may be classified as belonging to the family of equiangular spirals. They have the common characteristic that the angle (ψ) formed by the vectors of shear (and subsequently, stress) and geostrophic departure is invariant with height. A drawback of this assumption is the resultant restrictive distribution of eddy diffusivity (K) with height; parabolic height dependency alone is permitted, including the asymptotic case of constant K. The famous Ekman and Rossby spirals are two prominent members of this family of equiangular spirals. The new variangular theory, as the name implies, permits variation of ψ with height and is seen to produce more versatile profiles of wind, stress and eddy diffusivity.

1. Introduction

Atmospheric motions of meso-to-large scale are significantly affected by the Coriolis force. Within the planetary boundary layer friction forces are also present. Flow resulting from a pressure gradient is characterized by increasing speed and changing direction with increasing distance from the lower boundary. Due to the earth's rotation the resultant velocity hodograph is of the spiral type; a corresponding hodograph also exists for the stress variation. The problem is similar to the time/depth distribution of temperature and heat flux in a semi-infinite conductor with harmonically time-varying boundary conditions. Comparison may be made with Lettau (1954, 1962a).

Lettau (1961, 1962b) has investigated semi-empirical and theoretical hodographs of spiral structure theory, respectively. The former

theory is usually restricted to cases of neutral thermal stability for given values of the Coriolis parameter, surface aerodynamic roughness and horizontal pressure gradient. The latter may be construed to incorporate implicitly variations in stability, but the resultant height variation of the eddy diffusivity often appears unrealistic. The objectives of current and future spiral research must be to overcome these limitations. As stated previously—see Lettau (1962b)—"there is...a need for a simple, but reasonably reliable, practical method for estimating certain derived flow parameters (such as eddy diffusivity, or shearing stress, at various levels) on the basis of directly observable parameters (such as shear and rate of veering) in atmospheric...boundary layers."

The concept of the variangular spiral was first conceived by the senior author around 1950 and was recently employed independently by the junior author in a numerical approach to the atmospheric boundary layer problem. The present approach parallels the earlier work.

2. Generalized Spiral Solution

The formulation is restricted to steady and horizontally uniform large scale motion within the planetary boundary layer. It is assumed that at any point in the flow there exists a perfect balance among the Coriolis, friction and pressure gradient forces; inertia forces and mean vertical components are thus excluded. By definition, the friction force goes to zero at the top of the boundary layer and the vector of motion $(\vec{V})$ approaches the geostrophic value. Barotropy is assumed; i.e., thermal winds are excluded and the vector of geostrophic wind $(\vec{V}_g)$ is independent of height. In practice, thermal wind contributions to the motion may be eliminated and the data then analyzed to determine the effects of stability on the wind and stress distribution. Vertical variations of density (ρ) are dismissed as negligibly small as the layer under consideration is relatively shallow in comparison with the thickness of the entire troposphere.

Under the imposed restrictions, the equation of motion reduces to

$$\rho f i(\vec{V} - \vec{V}_g) = \vec{\tau}', \qquad (1)$$

where complex vector notation is used ($i = \sqrt{-1}$), primes denote partial differentiation with respect to height (z), and the Coriolis parameter is given as f. The vector of shearing stress $(\vec{\tau})$ is assumed horizontal and proportional to the wind shear vector. The factor of proportionality defines the effective dynamic viscosity (ρK), or the eddy diffusivity (K). Upon recalling the constancy of $\vec{V}_g$, the shearing stress may be expressed in terms of the geostrophic departure $(\vec{V} - \vec{V}_g)$,

$$\vec{\tau} = \rho K \vec{V}' = \rho K(\vec{V} - \vec{V}_g)'. \tag{2}$$

Equations (1) and (2) express the basic nature of the problem and may be combined to yield an interdependent set of two second-order, nonlinear homogeneous differential equations of the form

$$fi(\vec{V} - \vec{V}_g) = K(\vec{V} - \vec{V}_g)'' + K'(\vec{V} - \vec{V}_g)', \tag{3}$$

$$fi\,\vec{\tau} = K\vec{\tau}''. \tag{4}$$

The nonlinearity of Eqs. (3) and (4) arises from the fact that the eddy diffusivity ($cm^2\,sec^{-1}$) is the product of a length and a velocity; while the length term may be some universal and explicit height function, the velocity term is known to depend on the value of the shearing stress. The latter, in turn, is a dependent variable in the basic equations and hence the problem is inherently nonlinear.

In view of the spiral nature of the velocity and stress profiles, it will be convenient to define various observable angular quantities and to express solutions to Eqs. (3) and (4) in such terms. With reference to Lettau (1962b), consider the following identities and resultant boundary conditions; see also Fig. 1.

$\alpha \equiv$ angle between $\vec{V}$ and $\vec{V}_g$, (5.1)

$\beta \equiv$ angle between $(\vec{V} - \vec{V}_g)$ and $(-\vec{V}_g)$, (5.2)

$\gamma \equiv$ angle between $\vec{\tau}_0$ and $\vec{\tau}$, (5.3)

$\psi \equiv$ angle between $(\vec{V} - \vec{V}_g)'$ and $(\vec{V}_g - \vec{V})$, (5.4)

$r \equiv \tan\psi$. (5.5)

Boundary conditions at the height $z = 0$ are

$$\vec{V} \equiv \vec{V}_0 = 0, \tag{6.1}$$

$$\vec{\tau} \equiv \vec{\tau}_0 > 0, \tag{6.2}$$

$$K \equiv K_0 > 0, \tag{6.3}$$

$$\gamma_0 = \beta_0 = 0, \text{ and} \tag{6.4}$$

$$\alpha_0 = \psi_0 > 0 \quad \therefore \; r \equiv r_0 > 0, \tag{6.5}$$

while at very large heights the angular quantities are indeterminate and

$$\vec{V} = \vec{V}_g, \quad \text{and} \tag{7.1}$$

$$\vec{\tau} = 0. \tag{7.2}$$

In view of the definitions (5), Eqs. (3) and (4) may formally, and without loss of generality, be solved, where

$$\vec{V} - \vec{V}_g = -\vec{V}_g \exp - \int_0^{\beta} (i + 1/r)d\beta, \tag{8}$$

$$\vec{\tau} = \vec{\tau}_0 \exp - \int_0^{\gamma} (1 + r)d\gamma. \tag{9}$$

Because of the interdependency of Eqs. (8) and (9), or (3) and (4), solution of one automatically determines the other. It is to be noted that the following solution for Eq. (8) or (9) will be more straightforward in terms of $\vec{\tau}$ and hence the corresponding development in $(\vec{V} - \vec{V}_g)$ will be ignored.

Successive differentiation of Eq. (9) yields

$$\vec{\tau}'' = \vec{\tau}[\gamma'^2(r^2-1) - \gamma''r - \gamma'r' + i(2r\gamma'^2 - \gamma'')]. \tag{10}$$

Substitution of Eq. (2) in (10) and separation of real and imaginary parts leads to an expression for γ in terms of r, where

$$\gamma'' = \gamma'^2(r - 1/r) - \gamma'r'/r, \tag{11.1}$$

and for K, given as

$$f/K = \gamma'^2(r + 1/r) + \gamma' r'/r. \tag{11.2}$$

This formulation for K is analogous to the expression for the thermal diffusivity of a conductor as presented by Lettau (1954, 1962a). Solution of Eq. (11.1) for γ' is of the form

$$\frac{1}{r\gamma'} = \int_0^z \frac{1-r^2}{r^2}\, dz. \tag{11.3}$$

The discussion is entirely general to this point and no simplifications of the basic equations (1) and (2) have been made. The basic assumption of equiangular spiral theory is that the parameter r —and hence ψ —is independent of height. Equation (11.3) is then readily solved (γ is seen

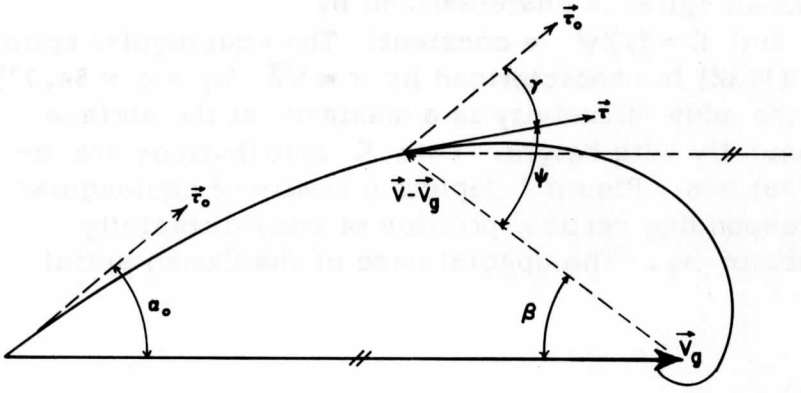

Fig. 1. Representative planetary boundary layer wind spiral depicting the vectors of shearing stress ($\vec{\tau}$), and the angular quantities α_0, β, γ and ψ.

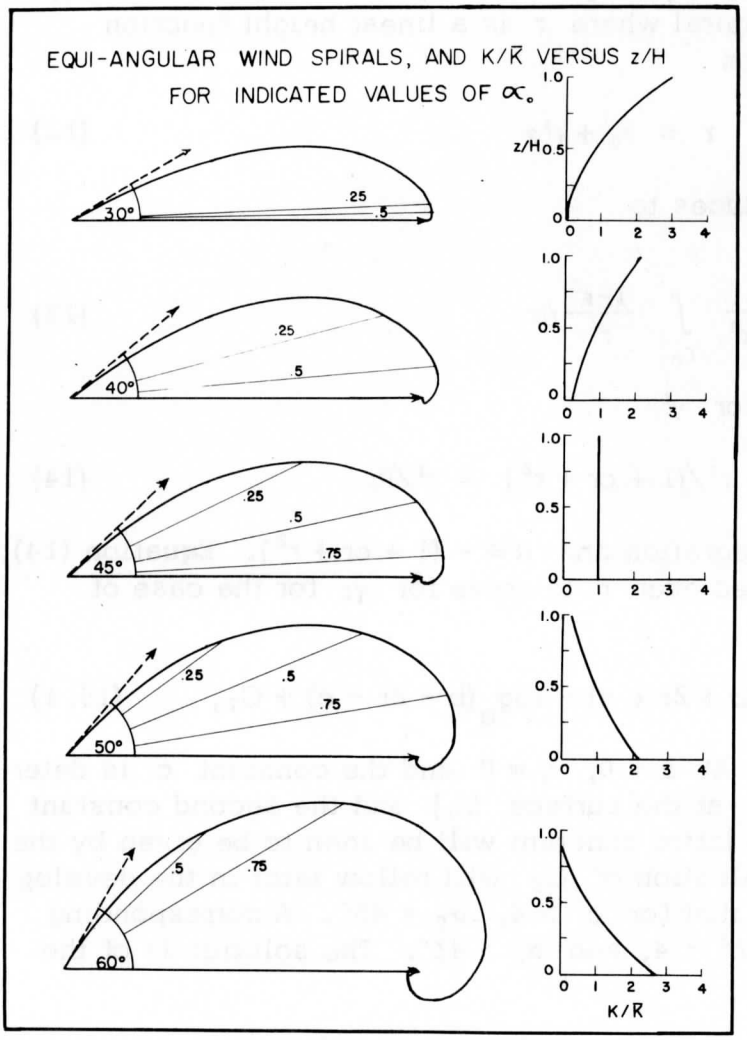

Fig. 2. A family of equiangular wind spirals and corresponding vertical profiles of eddy diffusivity (K relative to $\bar{K}$, versus z/H where H = geostrophic wind level), for five selected values of α_0 (angle between surface stress and ambient flow). The special case of the Ekman spiral is illustrated at the center.

to be a linear height function) and the stress spiral determined. The special case of the Ekman spiral is characterized by $r = 1$ ($\alpha_0 = \psi = 45°$) and $K = f/2\gamma' =$ constant. The equiangular spiral introduced by Rossby (1932) is characterized by $r = \sqrt{2}$ ($\alpha_0 = \psi = 54.7°$) and $K'/K = -2\gamma'/r_0$; the eddy diffusivity is a maximum at the surface and increases monotonically with height. Both K distributions are inconsistent with observations. Figure 2 depicts a family of equiangular wind spirals and corresponding vertical profiles of eddy diffusivity for five selected values of α_0. The special case of the Ekman spiral is included.

3. A Variangular Spiral

A special variangular solution to the problem of heat conduction in a semi-infinite medium was employed by Lettau (1962a). For this problem r was specified as the hyperbolic tangent of height (depth). As a new relaxation of the equiangular condition ($r = r_0 =$ constant), consider a variangular spiral where r is a linear height function ($r' =$ constant) of the form

$$r = r_0 + r'z \tag{12}$$

Equation (11.3) then reduces to

$$\frac{1}{r\gamma'} = \frac{1}{r'} \int_{r_0}^{r} \frac{1-r^2}{r^2}\, dr, \tag{13}$$

which is easily solved for γ':

$$\gamma' = -r'/(1 + cr + r^2) \equiv r'/R; \tag{14}$$

c is the constant of integration and $R \equiv -(1 + cr + r^2)$. Equation (14), in turn, may be integrated over r to solve for γ; for the case of $c^2 > 4$:

$$b\gamma = \log_e(b + 2r + c) - \log_e(b - 2r - c) + C_1, \tag{15.1}$$

where $b \equiv (c^2 - 4)^{1/2}$. At $z = 0$, $\gamma = 0$ and the constant c is determined by the value of r at the surface (r_0) and the second constant of integration C_1. The latter constant will be seen to be given by the product $b\alpha_0$; formal evaluation of C_1 will follow later in the development. It is to be noted that for $c^2 > 4$, $\alpha_0 < 45°$. A corresponding solution exists for $0 < c^2 < 4$, and $\alpha_0 > 45°$. The solution is of the form

$$b^* \gamma = 2 \tan^{-1} \frac{-2r - c}{b^*} + C_1^*, \tag{15.2}$$

where $b^* \equiv (4 - c^2)^{1/2}$.

Further discussion will tentatively be limited to those cases where $\alpha_0 < 45°$ and Eq. (15.1) applies. Although this encompasses the vast majority of observed conditions (α_0 values are known to be between 10 and 20° over water and between 20 and 35° over land), recent observations at Plateau Station, Antarctica, suggest that values two and three times the "norm" may not be infrequent.

Considering Eqs. (8), (9) and (13), (15.1) is sufficient to determine the spirals of both stress and geostrophic departure. Equations (3) and (4) can be reformulated as

$$\log_e \frac{S}{S_0} = - \int_0^\beta \frac{1}{r} \, d\beta, \tag{3.1}$$

$$\log_e \frac{T}{T_0} = - \int_0^\gamma r \, d\gamma, \tag{4.1}$$

where S and T are the absolute values of the vectors of geostrophic departure and shearing stress, respectively. Integration of Eq. (4.1) is then readily performed with the aid of (14), where

$$r \, d\gamma = \frac{r \, dr}{R} = \frac{1}{2} d \log_e R - \frac{c}{2} d\gamma.$$

With the proper boundary values the absolute value of the normalized shearing stress (T/T_0) is

$$\log_e \frac{T}{T_0} = - \frac{1}{2} \log_e \frac{R}{R_0} + \frac{c\gamma}{2} . \tag{4.2}$$

The spiral of geostrophic departure can similarly be determined, where

$$\log_e \frac{S}{S_0} = \log_e \frac{T}{T_0} + \frac{1}{2} \log_e \left[\frac{1+r^2}{1+r_0^2} \right]. \tag{3.2}$$

Necessary for the verification of the solution is the determination of the constant parameter r'. Recalling Eq. (11.2)

$$f/K = 2r\gamma'^2 - \gamma'',$$

and after substitution of Eq. (14):

$$K = -\frac{f R^2}{c r^{12}} \quad . \tag{16}$$

The integration constant c must assume the sign opposite that of the Coriolis parameter f in order to produce positive K. In contrast to the monotonical height functions for K (second-order polynomials) which result from the equiangular spiral solutions, the variangular theory produces a height distribution which corresponds to a fourth-order polynomial for K. Analysis of observed spirals indicates that the increase of order for the latter form appears to permit a more realistic representation. Figure 3 depicts profiles of K derived from data collected at Little America Station, Antarctica, and presented by B. Lettau (1967). Theoretical K profiles are given in Figure 5.

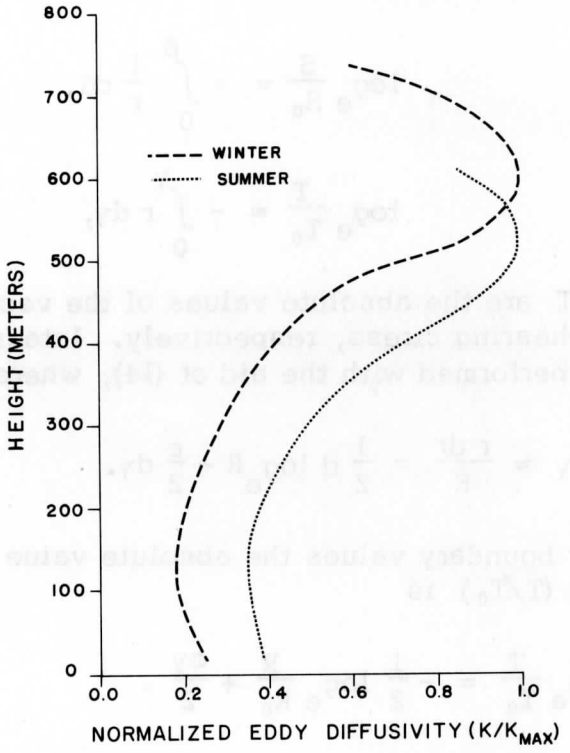

Fig. 3. Vertical profiles of normalized eddy diffusivity (K/K max) computed from data presented by B. Lettau (1967) for north winds at Little America Station, Antarctica.

Evaluation of Eq. (16) reveals that K can be zero-valued for two values of r. Define that height above the surface where $K = 0$ as $z = H$; then by (16)

$$r_H = -(c \pm b)/2. \tag{17.1}$$

Furthermore, for values of $c < -2$, $r_0 < 1$, and therefore $R_0 > 0$. Upon recalling Eq. (14), r' must be positive in order that γ' be positive. The correct expression for r_H is then

$$r_H = -(c - b)/2. \tag{17.2}$$

Having obtained an expression for K, it is now possible to evaluate the constant C_1 in Eq. (15.1). Paralleling Lettau (1961), the hypothesis is introduced that the level (Z) of maximum eddy diffusivity coincides with the level of maximum cross-isobaric flow. Then, from Eq. (16)

$$\left(\frac{K'}{K}\right)_Z = -\left(\frac{2(c+2r)r'}{R}\right)_Z = 0, \text{ and} \tag{16.1}$$

$$r_Z = -c/2. \tag{17.3}$$

Through purely geometric considerations γ is expressible in terms of the other angular quantities, where

$$\gamma = \beta - \psi + \alpha_0. \tag{18.1}$$

At the level Z

$$\gamma_Z = \alpha_0, \text{ and } \beta_Z = \psi_Z. \tag{18.2}$$

Recalling Eq. (15.1)

$$b\gamma = \log_e(b + 2r + c) - \log_e(b - 2r - c) + C_1$$

and evaluating at Z, $C_1 = b\alpha_0$.

Solution of the system of equations is now complete and stress and departure spirals may readily be computed.

4. Discussion

Sample theoretical profiles of wind and eddy diffusivity for values of α_0 of 33.8° and 41.3° are presented in Figs. 4 and 5. For both cases H = 200m and V_g = 12m sec^{-1}. A more refined sample might entail decreasing values for H and possibly V_g as α_0 increases. Significant is the quantitative agreement of K with observed data (see Fig. 3). Figure 6 depicts detailed characteristics of the flow structure near the surface over a range of α_0 values. A major advantage of the present model is well illustrated by these figures. Excluding other variations, α_0 can be expected to vary in proportion to changes in stability and hence surface wind characteristics must also reflect these variations. The variangular theory describes the gross features of profile curvature and slope which accompany stability variations. Figure 7 exemplifies the large wind directional changes which can occur near the surface under strong temperature inversions. The data were collected during the Antarctic winter of 1967 at Plateau Station by M. Kuhn for the U.S. Army Natick Laboratories.

Another advantage of the theory is the straightforward expression of K_0, τ_0 and the columnar total of boundary layer energy dissipation E_t, by external conditions.

$$K_0 = -\frac{fH^2R_0^2}{c(r_H-r_0)^2} \tag{19}$$

$$\tau_0 = \frac{\rho f V_g H R_0 \cos \alpha_0}{(r_h - r_0)} \tag{20}$$

$$E_t = \frac{\rho f V_g^2 H R_0 \cos^2 \alpha_0}{(r_H - r_0)} \tag{21}$$

Future work will seek to evaluate the model for the prediction of K_0, τ_0, and E_t, and as a tool for improved understandings of stability effects on boundary layer structure. The parameter $H/(r_H-r_0)$ may be a key toward such understanding.

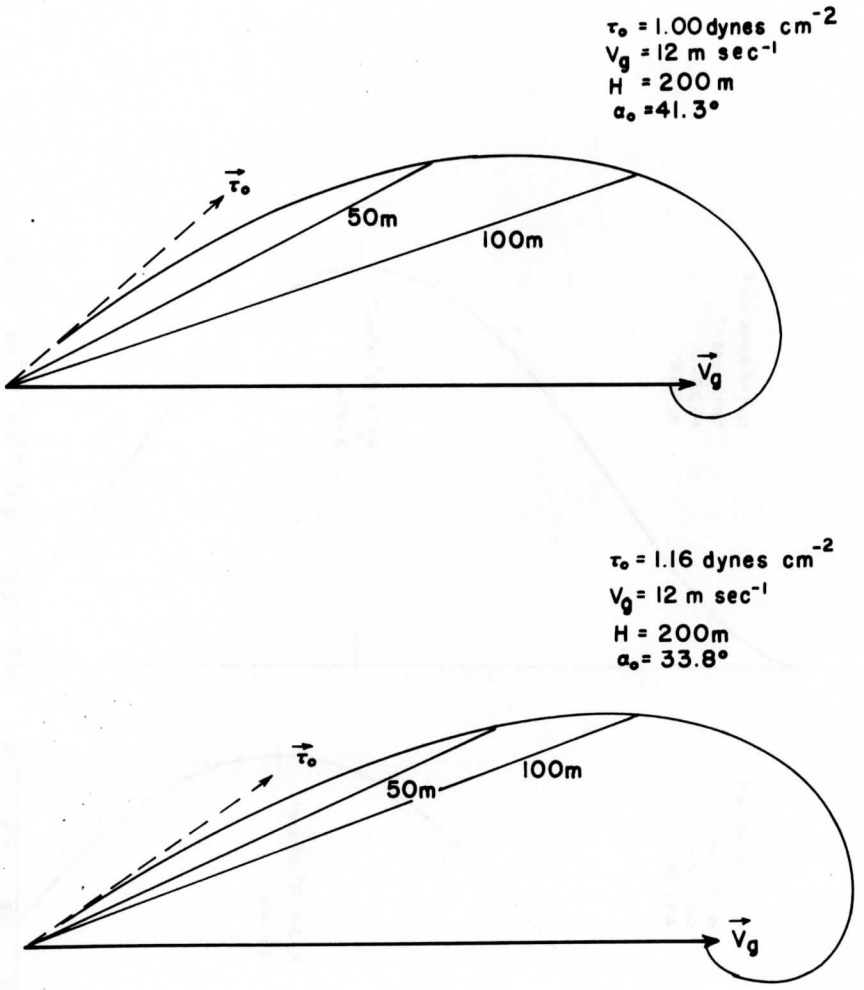

Fig. 4. A family of two variangular wind spirals for two selected values of α_0 (angle between surface stress and ambient flow). Also given are the values of the geostrophic wind ($\vec{V}_g$), boundary layer thickness (H), and surface stress ($\vec{\tau}_0$).

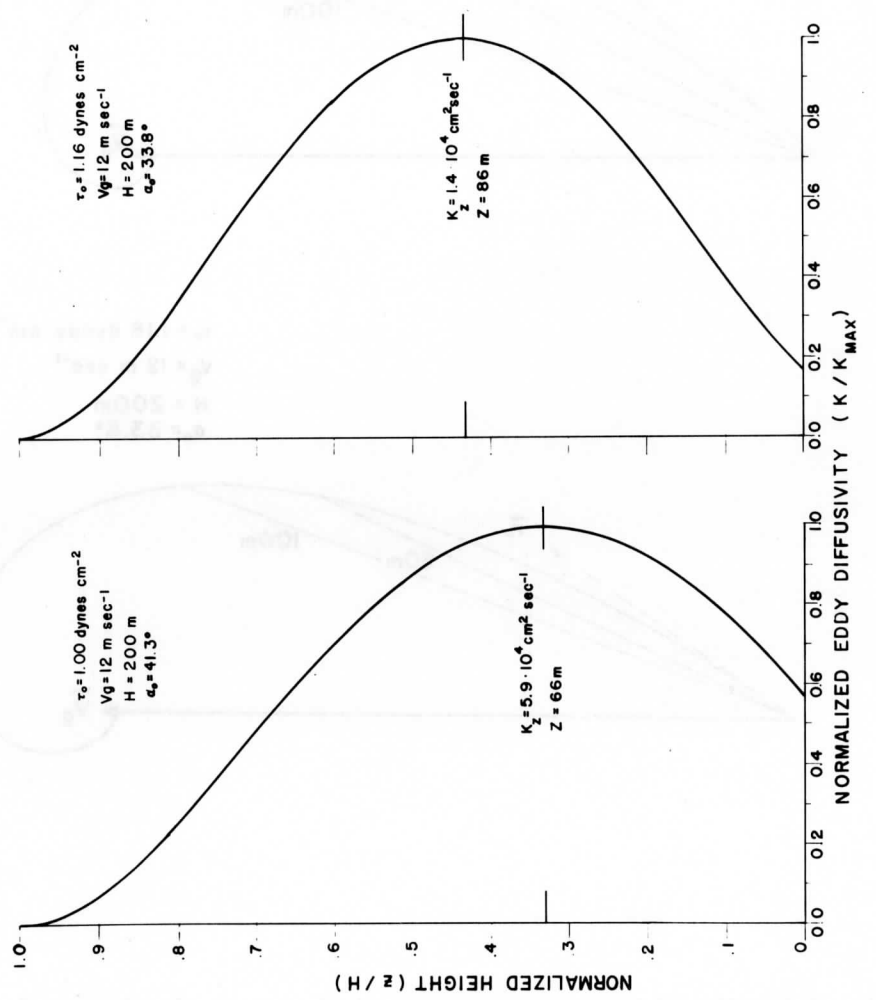

Fig. 5. A corresponding family of two vertical profiles of the normalized eddy diffusivity (K/K_{max}). Also given are the values of the geostrophic wind ($\vec{V}_g$), boundary layer thickness (H), and surface stress ($\vec{\tau}_0$).

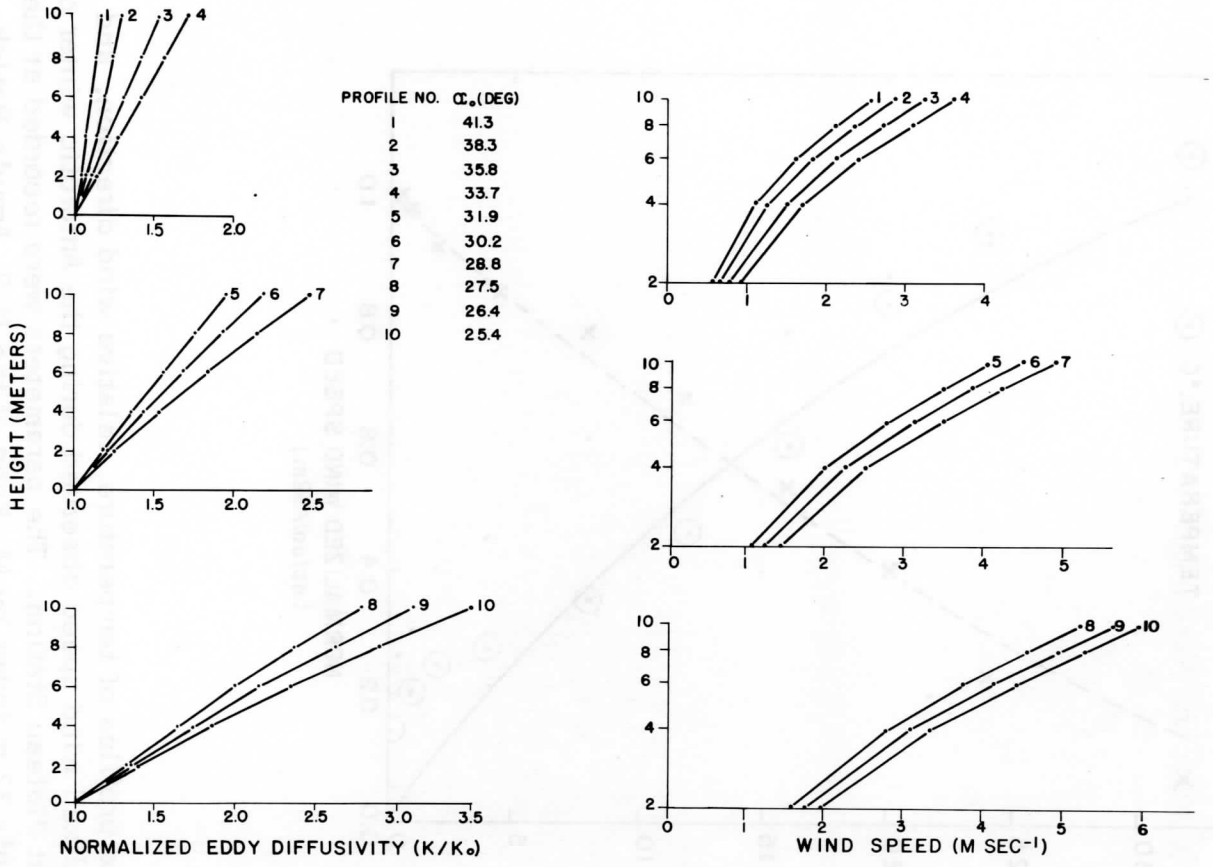

Fig. 6. Vertical profiles of normalized eddy diffusivity (K/K_0) and wind speed (m sec^{-1}) for ten values of α_0 (angle between surface stress and ambient flow) ranging from 41.3° to 25.4°. The geostrophic wind speed is 12 m sec^{-1} while the boundary layer thickness is 200 m.

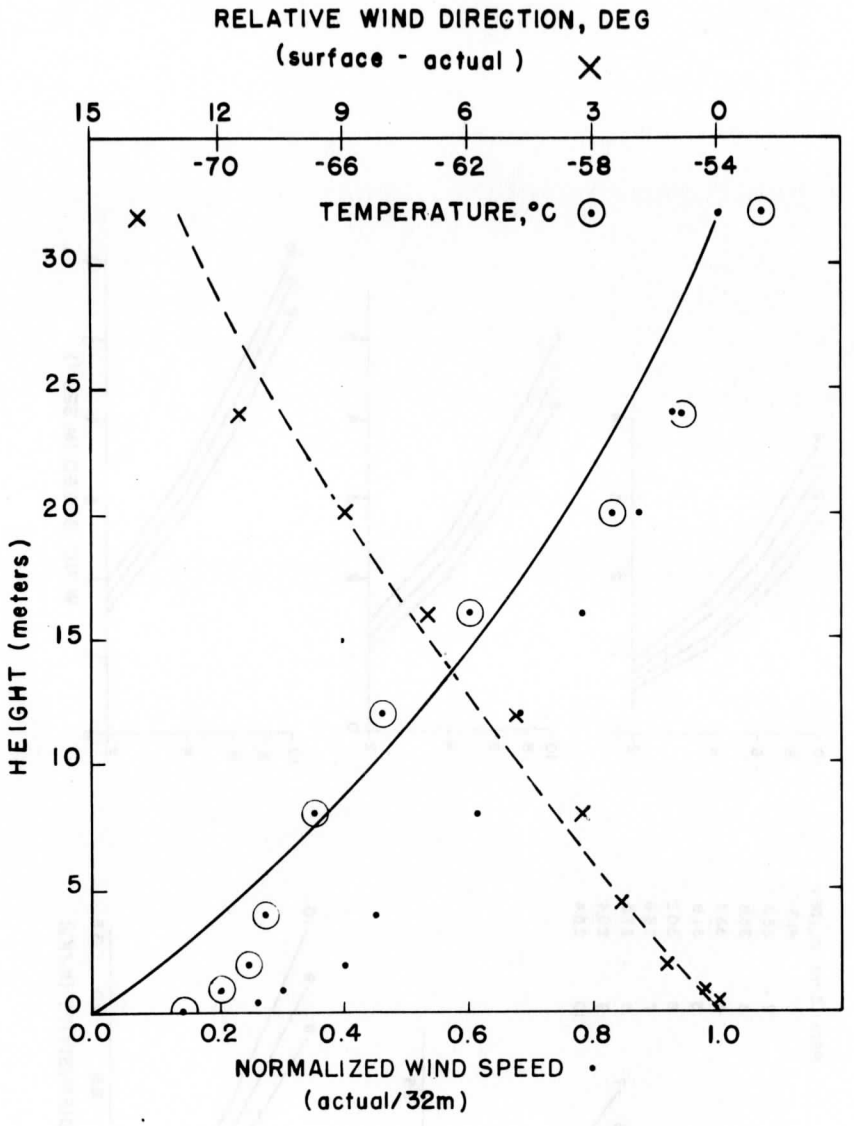

Fig. 7. Sample profiles of temperature, relative wind direction, and normalized wind speed observed during the Antarctic winter of 1967 at Plateau Station. The parameters were recorded at the station's 32 m tower by M. Kuhn of the U.S. Army's Natick Laboratories. The two curves are synthetic profiles of wind speed (——) and wind direction (---).

References

Ekman, V. W. (1902). Myt. Mag. Naturv., 40.

Lettau, B. (1967). "Thermally and Frictionally Produced Wind Shear in the Planetary Boundary Layer at Little America, Antarctica," Monthly Weather Review, 95, 9, pp. 627-634.

Lettau, H. (1954). "Improved Models of Thermal Diffusion in the Soil," Trans. Amer. Geophys. Union, 35, pp. 121-132.

Lettau, H. (1962a). "A Theoretical Model of Thermal Diffusion in a Non-Homogeneous Conductor," Gerland's Beitr. Geophys., 71, 257-271.

Lettau, H. (1962b). "Equiangular Wind and Current Spirals," Final Report, Contract DA-36-039-SC-80282 (USAEPG, Fort Huachuca, Arizona), pp. 159-172, University of Wisconsin, Madison.

Rossby, C. G. (1932). "A Generalization of the Theory of the Mixing Length with Applications to Atmospheric and Oceanic Turbulence," Mass. Inst. Tech. Meteor. Papers, 1, 4.

Scanner's note:

This page is blank.

THE DETERMINATION OF THE SURFACE ROUGHNESS FROM WIND SPEED AND AIR TEMPERATURE PROFILES IN THE SURFACE LAYER

C. R. Stearns
Department of Meteorology
University of Wisconsin at Madison

ABSTRACT:

The aerodynamic estimation of the flux densities of sensible heat, latent heat and momentum in the surface layer is dependent on the surface roughness and the displacement height for the wind speed and air temperature profile. Using surface layer profile theory the value of displacement height and surface roughness is selected which results in the minimum error squares between the observed and the theoretical wind speed profile. Two assumptions about the ratio of the eddy diffusivities of sensible heat and momentum result in negligible differences in d and z_0. The results are from 628 profiles using five measurement levels to 160 cm height.

1. Introduction

The generally accepted expression for the wind speed variation with height in the surface layer with an adiabatic lapse rate is

$$V(z) = V^* k^{-1} \ln[(z+z_0)/z_0] \qquad (1.1)$$

where $V(z)$ is the wind speed (cm sec^{-1}) at the height z(cm), $V^* = (\tau_0/\rho)^{1/2}$, τ_0 is the surface stress (dynes cm^{-2}), ρ is the air density (gm cm^{-3}), k the Karman constant, and z_0 is the surface roughness (cm). The locally measured height z may not be representative of the height of the upwind surface over which the wind is moving; therefore, it is convenient to introduce a displacement height d into (1.1) to allow for possible errors in the absolute height determination at the site and possible upwind variation in the terrain height. Then (1.1) becomes

$$V(z+d) = V^* k^{-1} \ln[(z + d + z_0)/z_0] \qquad (1.2)$$

discussed by Lettau (1957).

The solution to (1.2) now requires the determination of two parameters, d and z_0, where z_0 is a site parameter and d may vary with wind speed and direction in an unknown manner. The value of V^* will depend upon the selected values of z_0 and d. Solving (1.2) for V^* and differentiation with respect to d and z_0 yields,

$$\frac{\partial V^*}{\partial d} = -kV(z+d)\{\ln[(z+d+z_0)/z_0]\}^{-2}(z+d+z_0)^{-1} \qquad (1.3a)$$

$$\frac{\partial V^*}{\partial z_0} = -kV(z+d)\{\ln[(z+d+z_0)/z_0]\}^{-2}[(z+d+z_0)^{-1} - z_0^{-1}] \qquad (1.3b)$$

For example, given that $V^* = 30$ cm sec^{-1}, $z + d = 100$ cm, $k = 0.428$ and $z_0 = 1$ cm, then $V(z+d) = 322$ cm sec^{-1} and

$$\frac{\partial V^*}{\partial d} = -0.065, \qquad \frac{\partial V^*}{\partial z_0} = 6.45$$

A reasonable error in the sensor height measurement would be $\pm$ 1 cm and for z_0, $\pm$ 0.1 cm, which results in a 0.21% error in V^* due to the error in d and a 2.1% error in V^* due to the uncertainty in z_0. The surface roughness may be estimated from wind measurement at two levels in the adiabatic surface layer as

$$\ln z_0 = \ln(z+D) - d\ln(z+D)/d\ln V(z+d) \qquad (1.4)$$

where $D = d + z_0$. Using the previous conditions and selecting a second height of $z + d = 200$ cm where $V(z+d) = 371$ cm sec^{-1} and assuming a 1% error in the wind speed measurement at the 200 cm height, the error in the z_0 estimate is $\pm$ 0.5 cm, increasing the error in V^* to 10%. The point is that a reasonable error in wind speed of 1% at only one level results in an error of 0.5 cm in z_0 and thus an error of 10% in the determination of V^* from the wind profile. The corresponding error in τ_0 is about 20% which then influences the error in the aerodynamic estimates of the sensible and latent heat flux densities.

The relationships often used for estimating the aerodynamic heat flux densities, based on the exchange coefficient hypothesis (Sutton, 1953), are

$$Q_0 = -\rho c_p K_h \theta' \qquad (1.5a)$$

where Q_0 is the sensible heat flux density (ly sec^{-1}), c_p the heat capacity of the air (calories $gm^{-1}K^{-1}$), K_h the eddy diffusivity for heat ($cm^2 sec^{-1}$) and θ' the potential temperature gradient (K cm^{-1}),

$$E_0 = -\rho \mathcal{L} K_e q' \qquad (1.5b)$$

where E_0 is the latent heat flux density (ly sec^{-1}), $\mathcal{L}$ the latent heat of vaporization for water (cal gm^{-1}), K_e the eddy diffusivity for moisture (cm^2 sec^{-1}), and q' is the specific humidity gradient (gm H_2O per gm air cm^{-1}), and

$$\tau_0 = \rho K_m V' \tag{1.5c}$$

where τ_0 is the surface stress (dynes cm^{-2}) due to the wind, K_m is the eddy diffusivity for momentum (cm^2 sec^{-1}), and V' is the wind shear (sec^{-1}).

If V', θ' and Q' are determined at the same height above the surface layer and τ_0 is known then Q_0 can be determined as

$$Q_0 = - c_p \tau_0 \theta' V'^{-1} \tag{1.6a}$$

utilizing (1.5a) and (1.5c) and the assumption that $K_h K_m^{-1} = 1$. Assuming that $K_e K_m^{-1} = 1$, then E_0 can be determined as

$$E_0 = -L \tau_0 q' V'^{-1} \tag{1.6b}$$

The dependence of the aerodynamic method for determining Q_0 and E_0 on τ_0 means that the determination of τ_0 from wind speed and temperature profiles requires that the surface roughness and displacement height be determined as carefully as possible.

2. Theoretical Approach to Profile Structure

Utilizing wind speed measurements at several heights in the surface layer to determine z_0, the surface roughness, by (1.4), shows that the z_0 estimate decreases with height under lapse conditions and increases with height under inversion conditions (Lettau, 1966). The air temperature profile must be measured along with the wind profile when determining z_0 so that the influence of stability on the wind speed profile may be included to obtain a most nearly correct estimate of the surface roughness.

The theoretical approach to the profile structure used to determine z_0 and d is based on the Monin-Obukov (1954) definition of a non-dimensional wind shear or Lettau's (1962) diabatic influence function

$$\phi = k(z+z_0)V'V^{*-1}. \tag{2.1}$$

Integration of (2.1) with respect to height yields

$$\int_0^V dV = V^* k^{-1} \int_0^{z+d} \frac{\phi\, dz}{z + z_0 + d} . \qquad (2.2)$$

Letting $\phi = 1 + \phi - 1$, substitution in (2.2) and integration with respect to height gives

$$V(z+d) = V^* k^{-1} \{\ln[(z+d+z_0)/z_0] + \int_0^{z+d} (\phi-1)(z+d+z_0)^{-1} dz\}. \qquad (2.3)$$

An integral diabatic influence function Φ was introduced by Lettau (1962) as

$$\Phi = \int_0^{z+d} (\phi-1)(z+d+z_0)^{-1} dz \qquad (2.4)$$

which, by substitution in (2.3), yields

$$V(z+d) = V^* k^{-1} \{\ln[(z+d+z_0)/z_0] + \Phi\}. \qquad (2.5)$$

From the KEYPS model (Kazansky and Monin, 1956), (Ellison, 1957), (Yamamoto, 1959), (Panofsky, et al., 1960), (Sellers, 1962), for the atmospheric surface layer we have that

$$\underline{RI} = (1 - \phi^{-4})B^{-1} \qquad (2.6)$$

where $\underline{RI}$ is the flux Richardson number defined as

$$RI = K_h K_m^{-1} \underline{Ri} \qquad (2.7)$$

and the gradient Richardson number $\underline{Ri}$ is defined as

$$\underline{Ri} = g\, T_m^{-1}\, \theta' V'^{-2} \qquad (2.8)$$

where g is the acceleration of gravity (cm sec^{-2}) and T_m is the mean temperature (deg K) of the surface layer. The measurement of $\underline{Ri}$ does not involve height but only height differences between measurement levels.

Utilizing (1.5a), (1.5c), (2.7), (2.8) and the equation of state for air, $P = \rho R_d T_m$ where P = pressure, ρ = air density (gm cm^{-3}), and R_d = gas constant for dry air, one obtains

$$\phi \underline{RI} = - g k\, c_p^{-1} R_d P^{-1} Q_0 V^{*-3} (z+d+z_0). \qquad (2.9)$$

The definition of the surface layer is that Q_0 and V^* are constant with height above the surface, so the substitution of

$$L^{-1} = g\,k\,c_p^{-1}R_d P^{-1}Q_0 V^{*-3} \qquad (2.10)$$

may be made in Eq. (2.9) where L is the Lettau-Obukov-Monin (LOM) length scale of turbulence (Neumann, 1964), and considered constant with height in the surface layer.

Substituting (2.6) and (2.10) into (2.9), one obtains

$$\phi(1-\phi^{-4})B^{-1} = -(z+d+z_0)L^{-1}. \qquad (2.11)$$

$\underline{Ri}$ may be determined at the height $z + d + z_0$ from windspeed and air temperature profiles. Then

$$L^{-1} = \phi\,K_h K_m^{-1}\,\underline{Ri}(z+d+z_0)^{-1} \qquad (2.12)$$

may be determined assuming that either $K_h K_m^{-1}$ may be 1 or $\phi^{-1/2}$ (Stearns, 1967). In the first case

$$L^{-1} = \phi\,\underline{Ri}(z+d+z_0)^{-1} \qquad (2.13)$$

with $\underline{Ri} = (1-\phi^{-4})B^{-1}$, or for the second case

$$L^{-1} = \phi^{1/2}\,\underline{Ri}(z+d+z_0)^{-1} \qquad (2.14)$$

with $\underline{Ri} = \phi^{1/2}(1-\phi^{-4})B^{-1}$.

Solving (2.8) for θ' and utilizing (2.12) the potential temperature profile may be expressed as

$$\theta - \theta_0 = -T^*\{\ln[(z+d+z_0)/z_0] + \Phi_T\} \qquad (2.15)$$

where θ is the potential temperature (deg K) at the height $z + d$, and θ_0 is the potential temperature (deg K) at z_0 with $T^* = T_m k^{-1} c_p^{-1} R_d P^{-1} Q_0 V^{*-1}$ and constant in the surface layer. Φ_T is the integral diabatic influence function for the temperature profile. If $K_h K_m^{-1} = 1$, then $\Phi_T = \Phi$. If $K_h K_m^{-1} = \phi^{-1/2}$, then

$$\Phi_T = \int_0^{z+d} (\phi^{3/2} - 1)(z+d+z_0)^{-1}\,dz\,. \qquad (2.16)$$

Solving (2.11) for $(z+d+z_0)$, one obtains

$$z + d + z_0 = -\phi(1-\phi^{-4})B^{-1}L. \qquad (2.17)$$

Logarithmic differentiation of (2.17) with respect to height yields

$$\frac{dz}{z+d+z_0} = -\frac{(1+3\phi^{-4})}{\phi(1-\phi^{-4})}\,d\phi. \tag{2.18}$$

The substitution of (2.18) into (2.4) and along with the appropriate changes in the limits of integration ($\phi = 1$ at $z + d = 0$), gives

$$\Phi = \int_1^{\phi} \frac{(\phi-1)(1+3\phi^{-4})}{\phi(1-\phi^{-4})}\,d\phi \tag{2.19}$$

and if $K_h K_m^{-1} = \phi^{-1/2}$, then (2.16) becomes

$$\Phi_T = \int_1^{\phi} \frac{(\phi^{3/2}-1)(1+3\phi^{-4})}{\phi(1-\phi^{-4})}\,d\phi \tag{2.20}$$

which now relate Φ and Φ_T to only one parameter ϕ.

The nondimensional wind profile curvature may be expressed by the Deacon number DEU as

$$\underline{\text{DEU}} = -\,\partial \ln V'/\partial \ln(z+d+z_0). \tag{2.21}$$

Logarithmic differentiation of (2.1) and (2.11) with respect to the logarithm of height and substitution into (2.21) yields DEU as

$$\underline{\text{DEU}} = 4\phi^{-4}(1+3\phi^{-4})^{-1}. \tag{2.22}$$

Similarly, logarithmic differentiation of (2.8) with respect to the logarithm of height yields the nondimensional potential temperature profile curvature DET as

$$\underline{\text{DET}} = 2\,\underline{\text{DEU}} - \partial \ln \underline{\text{Ri}}/\partial \ln(z+d+z_0). \tag{2.23}$$

If $K_h K_m^{-1} = 1$ then from (2.6) and (2.7)

$$\underline{\text{DET}} = \underline{\text{DEU}}. \tag{2.24}$$

If $K_h K_m^{-1} = \phi^{-1/2}$, then

$$\underline{\text{DET}} = 1.5\ \text{DEU} - 0.5. \tag{2.25}$$

In summary, for any value of ϕ we can define $K_h K_m^{-1}$ as either 1 or $\phi^{-1/2}$. Then DEU, DET, RI, Ri, Φ, Φ_T and L^{-1} may be determined from ϕ and height where necessary, and are presented in Table 2.1 for several values of ϕ.

Table 2.1. Profile structure parameters for lapse and inversion conditions determined from $(z+z_0)\,L^{-1}$. The diabatic influence function ϕ is determined from $\phi(1-\phi^{-4})B^{-1} = -(z+z_0)L^{-1}$. The integral diabatic influence function for the wind profile Φ is determined from $\int_1^{\phi} (\phi-1)(1+3\phi^{-4})\phi^{-1}(1-\phi^{-4})d\phi$ and is independent of any assumption about $K_h K_m^{-1}$ as are the flux Richardson number $\underline{RI} = (1-\phi^{-4})B^{-1}$, and $\underline{DEU} = 4\phi^{-4}(1+3\phi^{-4})$. $\underline{RI} = \underline{Ri}$ and $\underline{DEU} = \underline{DET}$ only when $K_h K_m^{-1} = 1$. If $K_h K_m^{-1} = \phi^{-1/2}$, then the integral diabatic influence for the temperature profile is given by $\Phi = \int_1^{\phi} (\phi^{3/2}-1)(1+3\phi^{-4})\phi^{-1}(1-\phi^{-4})d\phi$, the curvature of the potential temperature profile by $\underline{DET} = 1.5\,\underline{DEU} - 0.5$, and $\underline{Ri} = \phi^{1/2}(1-\phi^{-4})\,B^{-1}$.

LAPSE CONDITIONS									INVERSION CONDITIONS								
$(z+z_0)L^{-1}$	ϕ	Φ	Φ_T	RI	DEU	Ri	DET	$K_h K_m^{-1}$	$(z+z_0)L^{-1}$	ϕ	Φ	Φ_T	RI	DEU	Ri	DET	$K_h K_m^{-1}$
0.0	1.0	0.0	0.0	0.0	1.0	0.0	1.0	1.0	0.0000	1.0	0.0	0.0	0.0	1.0	0.0	1.0	1.0
-0.009	0.961	-0.038	-0.056	-0.009	1.038	-0.009	1.057	1.020	0.0017	1.007	0.017	0.025	0.001	0.993	0.001	0.990	0.997
-0.013	0.948	-0.051	-0.076	-0.013	1.051	-0.013	1.076	1.027	0.0021	1.009	0.018	0.027	0.002	0.991	0.002	0.986	0.995
-0.017	0.929	-0.070	-0.104	-0.019	1.068	-0.018	1.102	1.037	0.0029	1.013	0.019	0.029	0.003	0.987	0.003	0.980	0.994
-0.025	0.905	-0.097	-0.144	-0.027	1.090	-0.026	1.134	1.051	0.0041	1.018	0.022	0.033	0.004	0.981	0.004	0.972	0.991
-0.035	0.874	-0.134	-0.198	-0.040	1.116	-0.037	1.174	1.070	0.0058	1.027	0.027	0.040	0.006	0.973	0.006	0.959	0.987
-0.049	0.836	-0.183	-0.269	-0.058	1.147	-0.053	1.220	1.094	0.0081	1.038	0.035	0.053	0.008	0.961	0.008	0.942	0.981
-0.068	0.791	-0.247	-0.360	-0.087	1.180	-0.077	1.270	1.125	0.0114	1.055	0.049	0.074	0.011	0.943	0.011	0.915	0.973
-0.097	0.739	-0.328	-0.474	-0.131	1.213	-0.112	1.319	1.163	0.016	1.081	0.071	0.107	0.015	0.917	0.015	0.875	0.962
-0.126	0.696	-0.403	-0.578	-0.181	1.237	-0.151	1.355	1.199	0.021	1.108	0.095	0.144	0.019	0.887	0.020	0.831	0.950
-0.176	0.640	-0.514	-0.730	-0.275	1.263	-0.220	1.394	1.250	0.029	1.161	0.139	0.212	0.025	0.831	0.027	0.746	0.928
-0.246	0.584	-0.644	-0.904	-0.421	1.283	-0.322	1.425	1.308	0.041	1.246	0.206	0.318	0.033	0.739	0.036	0.609	0.896
-0.346	0.529	-0.794	-1.103	-0.653	1.299	-0.475	1.449	1.375	0.058	1.386	0.307	0.480	0.040	0.598	0.048	0.397	0.849
-0.486	0.477	-0.965	-1.323	-1.021	1.311	-0.705	1.466	1.448	0.081	1.659	0.487	0.783	0.048	0.378	0.062	0.068	0.776
-0.684	0.428	-1.152	-1.561	-1.601	1.319	-1.048	1.478	1.529	0.114	2.132	0.787	1.322	0.053	0.169	0.077	-0.246	0.685
-0.966	0.383	-1.357	-1.816	-2.523	1.324	-1.562	1.486	1.616	0.161	2.894	1.293	2.321	0.055	0.055	0.093	-0.418	0.588

3. Theoretical Approach to the Minimizing Procedure

Surface roughness and displacement are determined such that the error squares on wind speed are a minimum. Using (2.5), let

$$\epsilon_i = V_i - V^* k^{-1} [\ln(z_i+d+z_0) - \ln z_0 + \Phi_i] \tag{3.1}$$

where ϵ_i is the error between the measured wind speed at the height $z + d$ indexed by i, and the theoretical wind speed at the same height using estimated values of d and z_0.

The least squares method (Lettau, 1957; Robinson, 1961) requires that $\sum_{i=1}^{n} \epsilon_i^2$ be a minimum where n is the number of measurement levels. The conditions for a minimum are that

$$\frac{\partial}{\partial z_0} \left(\sum_{i=1}^{n} \epsilon_i^2 \right) = 0 \tag{3.2}$$

and

$$\frac{\partial}{\partial d} \left(\sum_{i=1}^{n} \epsilon_i^2 \right) = 0. \tag{3.3}$$

Both conditions must be fulfilled and may be used as a criterion for determining successive approximations to d and z_0.

To facilitate the notation let

$$Z_i = \ln(z_i+d+z_0) - \ln z_0 + \Phi_i . \tag{3.4}$$

Then (3.3) becomes

$$V^* k^{-1} = n^{-1} \sum_{i=1}^{n} V_i Z_i^{-1} \tag{3.5}$$

and

$$\sum_{i=1}^{n} \epsilon_i^2 = \sum_{i=1}^{n} [V_i - V^* k^{-1} Z_i]^2 \tag{3.6}$$

The condition that $\sum_{i=1}^{n} \epsilon_i^2$ be a minimum with respect to z_0 is fulfilled when

$$GZ = \sum_{i=1}^{n} \left(-V^* k^{-1} V_i \frac{\partial Z_i}{\partial z_0} - k^{-1} \frac{\partial V^*}{\partial z_0} V_i Z_i + V^{*2} k^{-2} Z_i \frac{\partial Z_i}{\partial z_0} + V^* k^{-2} \frac{\partial V^*}{\partial z_0} Z_i^2 \right) = 0. \tag{3.7}$$

Similarly, $\sum_{i=1}^{n} \epsilon_i^2$ is a minimum with respect to d when

$$GD = \sum_{i=1}^{n} (-V^* k^{-1} V_i \frac{\partial Z_i}{\partial d} - k^{-1} \frac{\partial V^*}{\partial d} Z_i V_i + V^{*2} k^{-2} Z_i \frac{\partial Z_i}{\partial d} + V^* k^{-2} \frac{\partial V^*}{\partial d} Z_i^2) = 0 \tag{3.8}$$

From (3.4)

$$\frac{\partial Z_i}{\partial z_0} = \frac{\partial}{\partial z_0}[\ln(z_i+d+z_0) - \ln z_0 + \Phi_i] = (z_i+d+z_0)^{-1} - z_0^{-1} + \frac{\partial \Phi_i}{\partial z_0}. \tag{3.9}$$

From (2.19)

$$\frac{\partial \Phi_i}{\partial \phi_i} = (\phi_i - 1)(1 + 3\phi_i^{-4})\phi_i^{-1}(1-\phi_i^{-4})^{-1} \tag{3.10}$$

and from (2.11)

$$\frac{\partial \phi_i}{\partial z_0} = \phi_i(1 - \phi_i^{-4})(1 + 3\phi_i^{-4})^{-1}(z_i+d+z_0)^{-1}. \tag{3.11}$$

Substitution of (3.10), (3.11) and (2.11) in to (3.9) with cancellation of terms yields

$$\frac{\partial \Phi_i}{\partial z_0} = (\phi_i - 1)(z_i+d+z_0)^{-1} \tag{3.12}$$

(3.9) now becomes

$$\frac{\partial Z_i}{\partial z_0} = \phi_i(z_i+d+z_0)^{-1} - z_0^{-1}. \tag{3.13}$$

Similarly it may be shown that

$$\frac{\partial Z_i}{\partial d} = \phi_i(z_i+d+z_0)^{-1}. \tag{3.14}$$

Then, from (3.5), we have that

$$\frac{\partial V^*}{\partial z_0} = n^{-1} \sum_{i=1}^{n} V_i k Z_i^{-2} \frac{\partial Z_i}{\partial z_0} \tag{3.15}$$

and

$$\frac{\partial V^*}{\partial d} = n^{-1} \sum_{i=1}^{n} V_i k Z_i^{-2} \frac{\partial Z_i}{\partial d}. \tag{3.16}$$

GZ may be evaluated by substituting (3.13) and (3.15) into (3.7) and GD by substituting (3.14) and (3.16) into (3.8).

The method used for making successive approximations to z_0 and d is the rule of false position (Courant, 1937). If $\sum_{i=1}^{n} \epsilon_i^2$ has a minimum with respect to z_0 or d then $\frac{\partial}{\partial z_0} \sum_{i=1}^{n} \epsilon_i^2$ or $\frac{\partial}{\partial d} \sum_{i=1}^{n} \epsilon_i^2$ will pass through zero at the value of z_0 or d where $\sum_{i=1}^{n} \epsilon_i^2$ is a minimum. Given two initial guesses to z_0, $z_0(1)$ and $z_0(2)$, respectively then, according to the rule of false position, an approximation to z_0 would be

$$z_0(3) = \frac{z_0(1)GZ(2) - z_0(2)GZ(1)}{GZ(2) - GZ(1)} \tag{3.17}$$

where GZ(1) is evaluated by (3.7) utilizing $z_0(1)$ and d(1), the initial estimate of d. GZ(2) is evaluated similarly with $z_0(2)$, the next guess at z_0, and d(1). A tolerance check may be made by the difference $z_0(3) - z_0(2)$. If the difference is not small enough, then another approximation may be made to z_0 by replacing $z_0(1)$ with $z_0(2)$, GZ(1) with GZ(2), $z_0(2)$ with $z_0(3)$ and evaluating (3.7) to obtain GZ(2) still with the initial estimate of d, d(1). If the tolerance $z_0(3) - z_0(2)$ is acceptable, then $z_0(2)$ is a sufficiently accurate approximation to z_0. If not, then the cycle may be continued until the desired tolerance on z_0 is reached. For the greatest efficiency the two initial guesses at z_0 should be selected so that the value of z_0 which results in $\sum_{i=1}^{n} \epsilon_i^2$ being a minimum is between the two initial guesses.

The value of z_0 within the desired tolerance which results in $\sum_{i=1}^{n} \epsilon_i^2$ being a minimum for the value of d(1) selected on the first estimate of d is now used in (3.8) along with d(1) to determine GD(1). The second initial guess at d, d(2), is used above to determine another approximation of z_0 which is used in (3.8) to determine GD(2). Then a third estimate is made on d as

$$d(3) = \frac{d(1)GD(2) - d(2)GD(1)}{GD(2) - GD(1)} ; \tag{3.18}$$

A tolerance check is also made on d by d(3) - d(2) which, if it is as small as desired, gives a value of d, z_0, and V^* based on the condition that (3.6) is a minimum value. If the tolerance on d is not met then the cycle may be continued by replacement as was done in determining z_0 until the desired tolerance on the estimation of d is fulfilled.

The minimizing of the error squares on wind speed was programmed for computer solution. An example of the iterative steps required for the solution of one wind and temperature profile is given in Table 3.1. Figure 3.1 outlines the steps in the computer program for determining z_0 and d.

Figure 3.2 presents $\sum_{i=1}^{n} \epsilon_i^2$ and V^* as a function of d and z_0.

Table 3.1. Example of the iterative steps used in determining the values of the displacement height (d, cm) and surface roughness (z_0, cm) which give a minimum error squares fit on wind speed. GD is the slope of the error squares with respect to displacement height and GZ is the slope with respect to the surface roughness. The minimum error squares is when both GD and GZ are zero. The initial values of displacement height and surface roughness used to start the iterative process are not included.

d	GD	z_0	GZ
1.93	19.64	2.28	112.7
		2.32	10.7
		2.33	0.1
2.46	4.24	2.50	56.4
		2.52	7.9
		2.53	0.1
2.43	-0.28	2.55	9.32
		2.56	1.38
2.47	-1.30	2.57	4.4
		2.57	0.7
1.96	-1.42	2.49	-25.1
		2.48	-3.3
		2.48	0.1
2.14	0.80	2.49	0.6
2.24	0.28	2.51	6.3
		2.52	0.9
2.19	-0.27	2.51	-1.27
2.22	0.39	2.52	1.14
2.21	-0.33	2.51	-0.4

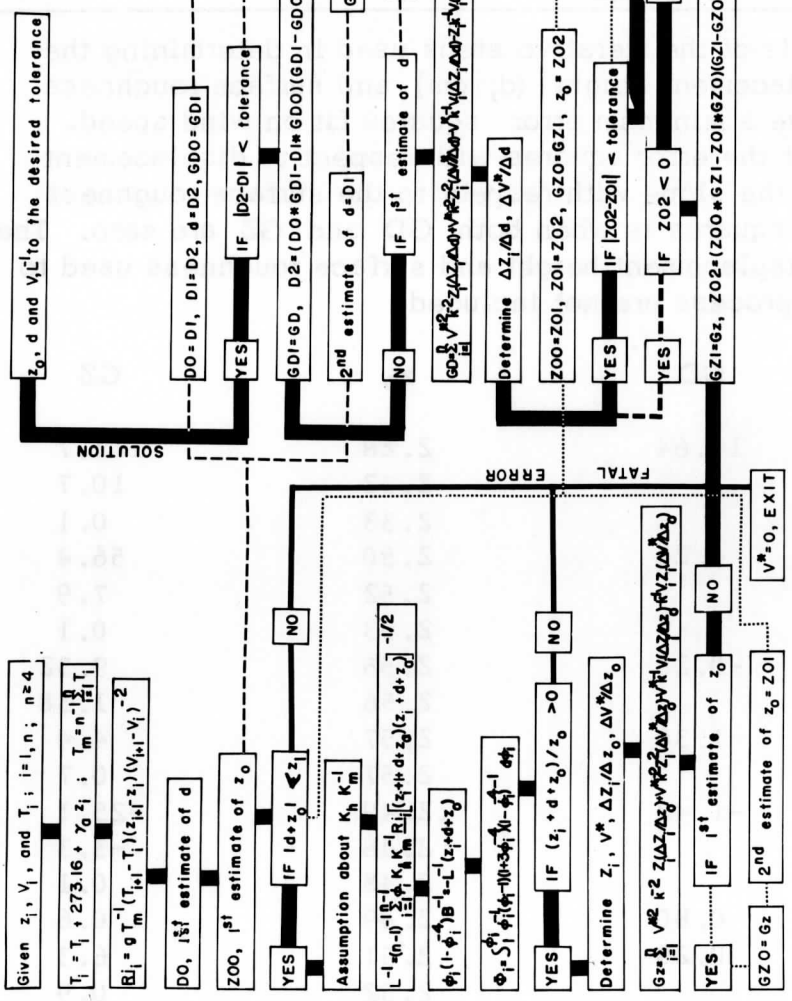

Fig. 3.1. Computer program paths for determining displacement height (d, cm), surface roughness (z_0, cm) and LOM (L, cm) length scale of turbulence from wind speed and air temperature profile data in the surface layer. The wide path starting at the upper left hand side is the path for a solution ending at the upper right hand side. A fatal error occurs if $|d+z_0| >$ height of the lowest level or if $(z_i+d+z_0)z_0^{-1} < 0$ and is indicated by the narrow path. The z_0 determination occurs in a loop indicated by the short dashed line for a given value of d. The loop for d is indicated by the long dashed line.

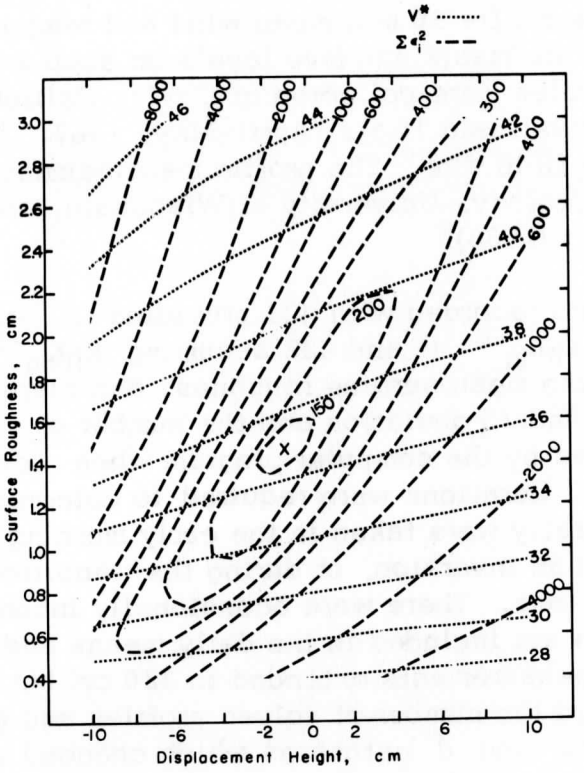

Fig. 3.2. Friction velocity (V^*, cm sec^{-1}) and the error squares on wind speed, $\sum_{i=1}^{n} \epsilon_i^2 = \sum_{i=1}^{n} \{V_i - V^* k^{-1}[\ln(z_i+d+z_0) - \ln z_0 + \Phi_i]\}^2$, as a function of displacement height (d, cm) and surface roughness (z_0, cm) illustrating the importance of a selected value for d and z_0 on the resulting value of V^*. The best value of d, z_0 and V^* is accepted by the computer program as the point where $\sum_{i=1}^{n} \epsilon_i^2$ is a minimum.

4. Results

The computer program was used to determine the surface roughness and displacement height for 30 min mean wind and temperature profiles utilizing three separate masts and five levels on each mast to a height of 160 cm. The profiles were collected at Davis, California during the U.S. Army Cooperative Field Trials, April-May, 1967. Jones, et al. (1965) describes the field site. The profile measurements made by the Department of Meteorology, University of Wisconsin, are described by Stearns and Dabberdt (1968).

628 profiles were recorded with 423 providing z_0 and d determination assuming $K_h K_m^{-1} = 1$ and 422 assuming $K_h K_m^{-1} = \phi^{-1/2}$. Table 4.1 presents the mean surface roughness and displacement height for each day, the standard deviation and the number of samples. The profiles were rejected by the computer program when $|d+z_0| >$ lowest level or more than 20 iterations were required to determine d. The rejected profiles generally were taken in the early morning before sunrise with light winds and an inversion, or during the transition between lapse and inversion conditions. There were occasionally inconsistent estimates of z_0 and d which are included in the daily means and standard deviations. The profile measurements extended to 320 cm but utilizing levels above 160 cm reduced the number of solved profiles and generally those solved resulted in z_0 and d estimates which changed with the number of levels used.

5. Conclusions

The inability to determine z_0 and d for all profiles, the occasional erratic estimates of z_0 and d, and the frequent dependence of z_0 and d on the number of measurement levels used raises doubts about both the vertical extent of the surface layer and the assumption that the profile structure is in equilibrium with the surface over which the air is moving. The study by Fredericks (Section 2, above) of the velocity divergence between the three masts indicates that at the 160 cm level and above divergences of the order of 10^{-3} sec^{-1} may be expected which implies that L is no longer constant with height. The interrelationship between the profile structure and the divergence of velocity should be pursued as a possible explanation for some of the discrepancies in the z_0 and d estimates.

The measurement levels used at Davis, California were 20, 40, 80, 120, 160, 200, 240, 280 and 320 cm. A more appropriate arrangement would have been 20, 40, 60, 80, 100, 120, 140, 160 and 180 cm which is as close together as the particular type of anemometer used could be

Table 4.1. Mean daily displacement heights (d, cm), standard deviation $\sigma(d)$, mean daily surface roughness (z_0, cm) and standard deviation $\sigma(z_0)$ for windspeed and air temperature profiles collected at Davis, California, for the U.S. Army, Electronics Command, Atmospheric Sciences Laboratory, Ft. Huachuca, Arizona, Cooperative Field Trials.

	Mast No.	Total Profiles Collected	$K_h K_m^{-1} = 1$					$K_h K_m^{-1} = \phi^{-1/2}$				
			No. of Profiles	d	$\sigma(d)$	z_0	$\sigma(z_0)$	No. of Profiles	d	$\sigma(d)$	z_0	$\sigma(z_0)$
4/26/67	1	18	18	0.0	0.0	1.02	0.14	18	0.0	0.0	1.04	0.12
	2	17	17	4.0	3.3	0.83	0.06	17	3.8	3.3	0.84	0.06
	3	2						2	0.8	1.1	0.96	0.21
4/27/67	1	25	16	1.2	1.9	1.51	0.36	15	0.9	1.1	1.58	0.35
	2	22	18	0.4	1.1	1.01	0.12	16	0.3	0.9	1.00	0.14
	3	26	15	-0.5	0.9	1.19	0.08	15	-0.7	0.9	1.19	0.09
4/28/67	1	33	21	0.4	1.3	0.84	0.11	22	0.1	0.7	1.11	0.99
	2	28	14	1.7	2.8	0.84	0.26	14	0.5	1.5	0.85	0.30
	3	28	16	2.0	2.7	0.75	0.07	17	1.5	2.4	0.73	0.05
5/2/67	1	31	19	0.6	1.2	0.84	0.17	25	1.3	2.5	0.87	0.18
	2	31	19	0.5	2.2	1.01	0.76	20	0.4	2.0	0.86	0.14
	3	29	14	2.4	1.6	0.84	0.13	17	2.7	3.2	1.00	0.74
5/3/67	1	47	31	0.5	1.1	0.94	0.18	33	0.7	2.6	0.96	0.16
	2	47	30	0.2	2.5	0.93	0.17	31	-0.0	2.0	0.96	0.17
	3	47	29	2.2	3.6	0.96	0.53	32	1.6	2.5	0.88	0.26
5/4/67	1	48	36	0.0	2.0	1.31	0.46	36	0.1	2.3	1.35	0.49
	2	47	35	-1.3	2.8	1.16	0.38	36	-1.8	2.8	1.13	0.39
	3	43	31	2.2	2.9	1.51	0.81	30	1.9	2.4	1.54	0.83
5/5/67	1	23	17	-2.0	2.1	1.25	0.28	18	-2.4	2.2	1.16	0.29
	2	23	9	-1.8	1.9	1.24	0.27	9	-2.4	2.3	1.17	0.29
	3	23	18	-1.3	2.1	1.87	0.53	19	1.2	2.2	1.87	0.52
Total		628	423					442				

placed. The reason for the closer spacing is that more anemometers could safely be assumed within the surface layer and thus more levels would be available for determining z_0 and d, and the desired measurement of the surface stress by the wind and temperature profile.

Those profiles should be selected for determining z_0 and d which do not show a dependence on the number of measurement levels and are not accompanied by large divergences. The values of z_0 and d obtained could then be used for all other profiles to determine the wind stress and the aerodynamic estimates of sensible and latent heat flux densities.

A criterion needs to be established for determining the height of the surface layer within a desired tolerance on surface stress so that theories on the diabatic surface layer structure are not applied to heights above the surface where the theory will be invalid. Many discrepancies in data and variance in theories may be due to using profile data which is not in the surface layer or not in equilibrium with the surface.

References

Courant, R. (1937), Differential and Integral Calculus, Vol. 1, pp. 357-358, Interscience Publishers, Inc., New York.

Ellison, T. H. (1957). "Turbulent transfer of heat and momentum from an infinite rough plate," J. Fluid Mech., Vol. 2, pp. 456.

Fredericks, G. (1960). "Estimates of vorticity, divergence and vertical velocity in a surface layer," Masters Thesis, Department of Meteorology, University of Wisconsin, Madison, Wisconsin.

Jones, F.V., D. L. Morgan and D. A. Orr(1960), "Appendix B, Site description and data management," Final Report, 1965, Grant No. DA-AMC-28-043-65-G12 (USAEC, Fort Huachuca, Arizona), University of California, Davis, pp. 205-224.

Kazansky, A. B. and A. S. Monin (1956). "Turbulence in the inversion layer near the surface," Acad. Nauk, SSSR. Ser. Geophys. No. 1.

Lettau, H. H. (1957), "Computation of Richardson's numbers, classification of wind profiles and determination of roughness parameters," Exploring the Atmosphere's First Mile, Vol. I (Lettau and Davidson, Eds.), Pergamon Press, Inc., New York and London, pp. 337-372.

Lettau, H. H. (1962). "Notes on theoretical models of profile structure in the diabatic surface layer," Final Report, Contract DA-36-039-SC-80282 (USAEPG, Fort Huachuca, Arizona), University of Wisconsin, pp. 195-226.

Lettau, H. H. (1966), "Problems of micrometeorological measurements," The Collecting and Processing of Field Data (Bradley and Denmead, Eds.), Interscience Publishers, New York, London, Sydney, pp. 3-40.

Monin, A. S., and A. M. Obukhov (1954). "Dimensionless characteristics of turbulence in the surface layer," Akad. Nauk. SSR. Geofis. Trudy, No. 24, pp. 151-163.

Neumann, J. (1964). "Turbulent convection of turbulent kinetic energy in stratified shear flows," Sixth Annual Conference on Aviation and Astronautics, Feb. 1964, Tel Aviv and Haifa, Israel, pp. 47-49.

Panofsky, H., A. K. Blackadar, and G. E. McVehil (1960). "The diabatic wind profile," Quart. J. Roy. Meteor. Soc. (London), 86, 390.

Robinson, S. M. (1961). "A method for machine computation of wind profile parameters," Annual Report, Contract DA-36-035-SC-80282 (USAEPG, Fort Huachuca, Arizona), Univ. of Wisconsin, pp. 63-70.

Sellers, W. D. (1962). "Simplified derivation of the diabatic wind profile," J. of the Atmos. Sci., Vol. 19, No. 2, pp. 180-181.

Stearns, C. R. (1967), "Micrometeorological studies in the coastal desert of Southern Peru," Ph.D. thesis, Department of Meteorology, University ofWisconsin, Madison, Wisconsin, 179 pp.

Stearns, C. R. and W. F. Dabberdt (1968), "Collecting and processing of micrometeorological data for the Spring, 1967, Cooperative Field Experiment at Davis, California, "Final Report, Contract No. DAA DOH-67-C-0117, (USAEC, Fort Huachuca, Arizona), University of Wisconsin.

Stearns, C. R. (1969), "Computer Program for Determining Surface Roughness and Displacement Height from Wind Speed and Air Temperature Profiles in the Surface Layer," Department of Meteorology, University of Wisconsin, Madison, Wisconsin, 48 pp.

Sutton, C.B.E. (1953). Micrometeorology, McGraw-Hill, New York.

Yamamoto, G. (1959), "Theory of turbulent transfer in non-neutral conditions," J. Meteor. Soc. Japan, Vol. 37, No. 2.

8

THERMO-TIDAL WINDS IN AN EQUIVALENT BAROTROPIC BOUNDARY LAYER

Kenneth P. MacKay, Jr.

ABSTRACT:

Two models of the diurnal wind oscillation in an equivalent barotropic boundary layer over large-scale terrain slope are extended. Comparison of the wind response in Lettau's thermo-tidal model with analysis of data from the Great Plains Turbulence Field Program suggests that, as a first approximation, the geostrophic forcing function can be described as having a first harmonic amplitude which decreases exponentially with height and a phase hour which decreases linearly with height.

Holton's thermal forcing model is extended to include the effects of latitude variation. Comparison of observed and computed wind response indicate that Holton's extended model does not duplicate the observed first harmonic phase relationships adequately. It is suggested that Holton's model can also be described as a thermo-tidal model.

Possible avenues of further investigation are suggested.

1. Introduction

Lettau (1964, 1968) and Holton (1967) have attempted to explain the low-level jet, which has been documented over the Great Plains in connection with a diurnal wind oscillation providing a super-geostrophic maximum at a height of about 500 m above ground, sometime between midnight and sunrise. Both models describe the oscillation as being caused by the diurnal heating cycle over the large-scale terrain slope from the Rockies to the Mississippi River.

Lettau (1964) has introduced the term "thermo-tidal" wind. He reasons that the solar heating cycle over sloping terrain will produce harmonic variations in the thermal wind. The form of the variations is assumed known and used as a forcing function in the equations of motion.

Holton attempts a slightly more general model. He incorporates, in addition to the equations of motion, the thermodynamic energy equation. In a coordinate system with one axis tangent to the sloping ground surface these equations are coupled. He then prescribes the form of the oscillating heating function and employs this as his forcing function.

This report will investigate extensions of both of these models. The response of the wind to forms of the geostrophic forcing function in an equivalent barotropic atmosphere not considered by Lettau will be given. Holton's model, which as presented in his 1967 paper is strictly applicable only at 30° latitude, will be extended to other latitudes.

2. Wind Response to Diurnally Oscillating Pressure Gradient Forcing

Lettau (1964), (1968) has introduced the term thermo-tidal wind to describe wind oscillations caused by the solar forcing function and of large enough scale so that the Coriolis acceleration is significant. In his 1964 paper, Lettau solved the equations of motion for the component parallel to the geostrophic wind in an equivalent barotropic boundary layer. The solution was later supplemented by MacKay to the cross-isobaric component of the real wind (see Lettau, 1968). In the following, the structure of the pressure gradient force will be described in terms of the geostrophic wind, and the thermo-tidal model will be extended to include diverse mathematical forms of the geostrophic forcing function.

It is assumed that: (a) the eddy viscosity K is constant with height and time, (b) inertial accelerations of the wind are neglibible, and (c) that conditions for an equivalent barotropic boundary layer hold at all times during the cycle, or geostrophic motion has the same direction at all heights and times. With these assumptions, the equation of horizontal motion in complex vector notation is:

$$\dot{Q} + ifQ - KQ'' = -f V_g \qquad (2.1)$$

where $Q = u + iv$, and the v component of the wind is parallel to the geostrophic wind while the u component is 90° to the right. A raised dot indicates partial differentiation with respect to time, a prime differentiation with respect to height, and $i = \sqrt{-1}$. The geostrophic wind $V_g = \bar{V}(z) + V_1(z)(e^{i\omega t} + e^{-i\omega t})$, and the form of Q is assumed to be

$Q = \bar{Q}(z) + Q_1(z)e^{i\omega t} + Q_2(z)e^{-i\omega t}$, where ω is the angular rotation rate of the earth. Substitution of the expansions of V_g and Q into (2.1) results in three ordinary differential equations for $\bar{Q}$, Q_1 and Q_2:

$$\begin{aligned} K\bar{Q}'' - if\bar{Q} &= f\bar{V} \\ KQ_1'' - i(f+\omega)Q_1 &= fV_1 \\ KQ_2'' - i(f-\omega)Q_2 &= fV_1 \quad . \end{aligned} \tag{2.2}$$

The boundary conditions are $\bar{Q}(0) = Q_1(0) = Q_2(0) = 0$ and $\bar{Q}(\infty) = \bar{V}(\infty)$, $Q_1(\infty) = V_1(\infty)$ and $Q_2(\infty) = V_1(\infty)$.

If now the real velocities u and v are to be written as

$$\begin{aligned} u &= \bar{u} + u_1 \cos\omega t + u_2 \sin\omega t \\ v &= \bar{v} + v_1 \cos\omega t + v_2 \sin\omega t, \end{aligned} \tag{2.3a}$$

it follows that

$$\begin{aligned} \bar{u} &= RE(\bar{Q}) & \bar{v} &= IM(\bar{Q}) \\ u_1 &= RE(Q_1+Q_2) & v_1 &= IM(Q_1+Q_2) \\ u_2 &= -IM(Q_1-Q_2) & v_2 &= RE(Q_1-Q_2) \quad . \end{aligned} \tag{2.3b}$$

All that remains is to define the vertical structure of the components of the daily-mean geostrophic wind $\bar{V}$ and its diurnal amplitude V_1.

Figure 2.1a illustrates the response of the mean wind to a constant geostrophic wind, corresponding to the classic Ekman solution for a barotropic boundary layer. Figure 2.1b presents the response to a mean geostrophic wind decreasing linearly with height, a depiction of the Sverdrup-Hesselberg (1915) solution in an equivalent barotropic boundary layer. Figure 2.1c shows the response to a mean geostrophic wind decreasing exponentially with height (L. Mahrt, 1969, unpublished master's thesis, University of Wisconsin). The results of harmonic analysis of data taken during the Sixth General Observation Period of the Great Plains Turbulence Field Program (Lettau and Davidson, 1957), is depicted in Fig. 2.1c.

In Fig. 2.2 the responses of the diurnally oscillating component of the real wind to diverse forms of the periodic component of the geostrophic wind are shown. Figures 2.2a, b present the Lettau-MacKay solution for a geostrophic wind constant (2.2a) or decreasing linearly (2.2b) with height. With $V_1 = Vg_1 + zVt_1$ the components can be described analytically as

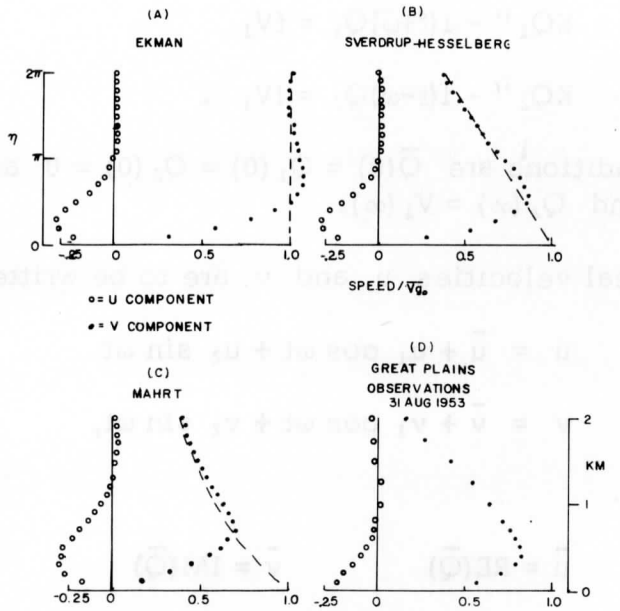

Fig. 2.1. Comparison of three steady-state boundary layer wind models for latitude 42.5° N with data from the Great Plains Turbulence Field Program. Coordinates aligned with V-component of wind parallel to mean geostrophic wind direction. Dashed lines indicate mean geostrophic wind profile.

$$u_1 = -Vg_1\left[\frac{e^{-\eta\alpha}\sin\eta\alpha}{\alpha^2} + \frac{e^{-\eta\beta}\sin\eta\beta}{\beta^2}\right] \tag{2.4}$$

$$u_2 = Vg_1\left[\pm\frac{2(\alpha^2-1)}{\alpha^2\beta^2}\left(1 - z\frac{Vt_1}{Vg_1}\right) + \frac{e^{-\eta\alpha}\cos\eta\alpha}{\alpha^2} \mp \frac{e^{-\eta\beta}\cos\eta\beta}{\beta^2}\right]$$

$$v_1 = Vg_1\left[\pm\frac{2}{\alpha^2\beta^2}\left(1 - z\frac{Vt_1}{Vg_1}\right) - \frac{e^{-\eta\alpha}\cos\eta\alpha}{\alpha^2} \mp \frac{e^{-\eta\beta}\cos\eta\beta}{\beta^2}\right]$$

$$v_2 = -Vg_1\left[\frac{e^{-\eta\alpha}\sin\eta\alpha}{\alpha^2} - \frac{e^{-\eta\beta}\sin\eta\beta}{\beta^2}\right].$$

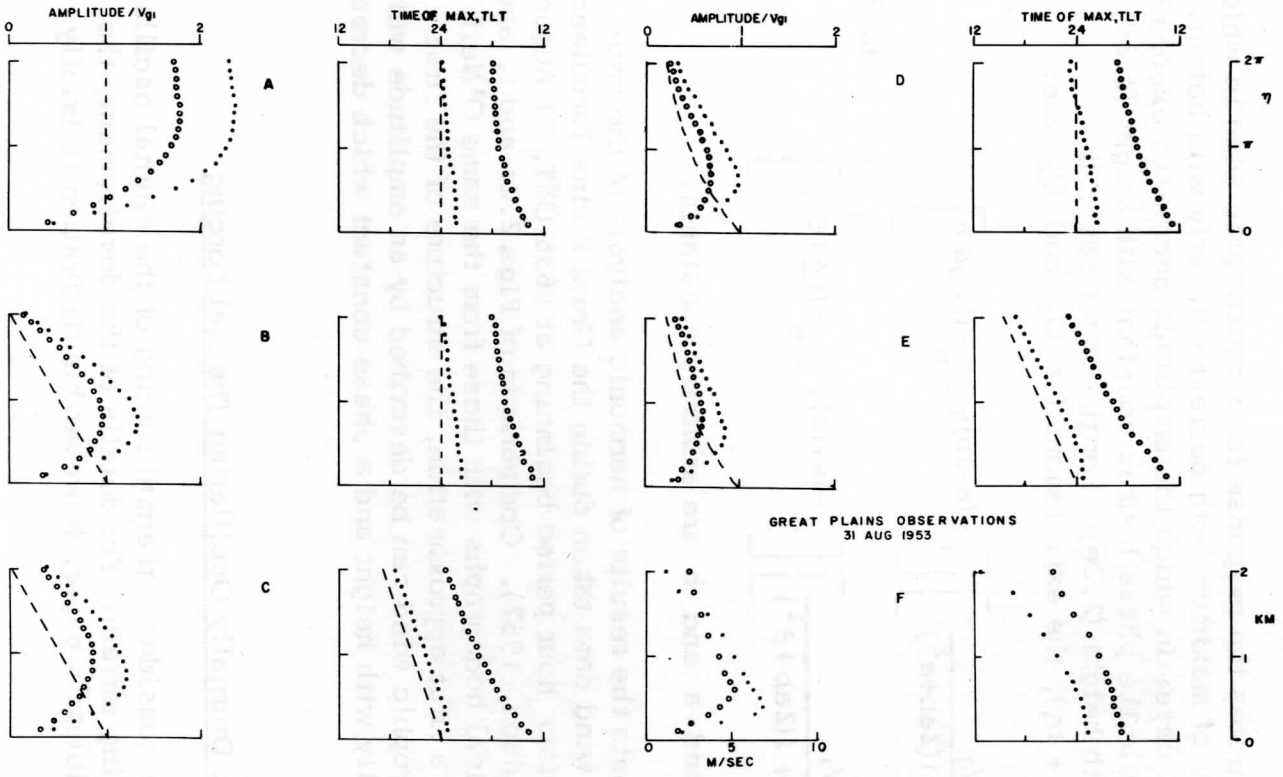

Fig. 2.2. First harmonic thermo-tidal wind response in various types of equivalent barotropic boundary layers at 42.5° N compared with data derived from the Great Plains Turbulence Field Program. Open circles are U-components, closed circles are V-components and dashed lines indicate first harmonic geostrophic components.

The upper sign applies for latitudes poleward of 30°, the lower sign for latitudes equatorward. For a geostrophic wind constant with height, $Vt_1 = 0$. The parameters are $\eta = \sqrt{f/2K}\, z$, $\alpha^2 = 1 + \omega/f$ and $\beta^2 = |1-\omega/f|$.

Figure 2.2c illustrates the response for a geostrophic wind in which the amplitude and hour of maximum both decrease linearly with height. Figure 2.2d, e present cases in which the amplitude decreases exponentially with height, while the phase hour is constant with height (2.2d) or decreases linearly with height (2.2e). For the latter case, if $Vg_1 = 2V_1 e^{-a\gamma} \cos(\omega t + b\gamma)$, the expressions for Q_1 and Q_2 are:

$$Q_1 = \left[\frac{V_1}{(a^2-b^2)-i(2ab+\alpha^2)}\right]\left[e^{-(a-ib)\gamma} - e^{-(1+i)\alpha\eta}\right]$$

$$Q_2 = \left[\frac{V_1}{(a^2-b^2)+i(2ab+\beta^2)}\right]\left[e^{-(a+ib)\gamma} - e^{-(1\pm i)\beta\eta}\right], \qquad (2.5)$$

where $\gamma = \eta\sqrt{2}$ and a and b are arbitrary constants.

Figure 2.2f presents the results of harmonic analysis of the two-hourly representative wind data taken during the Great Plains Turbulence Field Program twenty-four hour period beginning at 0636 CST, 31 August 1953 (Lettau and Davidson, 1957). Comparison of Figs. 2.2e and f, and comparison of theoretical hodographs with those from the same O'Neill data, suggest that as a first approximation, the structure of the first harmonic of the geostrophic wind can be described by an amplitude which decreases exponentially with height and a phase constant which decreases linearly with height.

3. Wind Response to Diurnally Oscillating Thermal Forcing

Holton (1967) has considered thermal forcing of the diurnal oscillation of wind over sloping terrain. For details of the development, the reader is referred to Holton's paper, however his derivation is briefly summarized below.

The conventional coordinate system in which x increases eastward, y northward and z increases vertically is replaced by an (χ, y, ζ) system in which χ is tangent to the ground surface and ζ is normal to the ground. The thermodynamic energy equation incorporates a heating function which is the sum of an eddy diffusion term and a radiation term. The three equations of motion, the continuity equation and a defining equation for potential temperature complete the set of equations.

The six equations are then nondimensionalized so that the dependent variables are of the order unity. The dependent variables are the three nondimensional wind components and nondimensional perturbation pressure, density and potential temperature. The vertical equation of motion, the equation of continuity and the defining equation for potential temperature are used to eliminate pressure, density and vertical velocity, reducing the equations to the two horizontal equations of motion and the thermodynamic energy equations:

$$\frac{\partial u}{\partial t} - v = -\left(vg - \frac{\theta \sin\phi}{\delta}\right) + \frac{\partial^2 u}{\partial \zeta^2}, \tag{3.1}$$

$$\frac{\partial v}{\partial t} + u = \frac{\partial^2 v}{\partial \zeta^2}, \tag{3.2}$$

$$\frac{\partial \theta}{\partial t} + \frac{u \sin\phi}{\epsilon\,\delta} = \frac{\partial^2 \theta}{\partial \zeta^2} + H(\theta_r - \theta). \tag{3.3}$$

The boundary conditions are:

$$\begin{aligned} &u = v = 0 \text{ and } \theta = \theta_r \text{ at } \zeta = 0 \text{ and} \\ &u, \theta \rightarrow 0 \text{ and } v \rightarrow vg \text{ as } \zeta \rightarrow \infty. \end{aligned} \tag{3.4}$$

The heating cycle is approximated by that of the radiation temperature

$$\theta_r = \theta_r(0)e^{-\zeta}(\cos \omega t^*)$$

Up to this point, the above analysis does not deviate from Holton's. However, Holton then states, "Now $t^* = t/f$ where $f = 2\omega s$ in (latitude) so that if we evaluate f at 30° N latitude we may write

$$\theta_r = \theta_r(0)e^{-\zeta} \cos t \quad \ldots$$"

This simplification restricts the validity of Holton's further development to 30° N latitude. If, however, we introduce the nondimensional parameter $\beta = \omega/f$ we may with more generality write

$$\theta_r = \theta_r(0)e^{-\zeta} \cos \beta t \tag{3.6}$$

While Holton considers solutions of the form $u = \bar{u} + RE[u_1(\zeta)e^{it}]$ and similar forms for v and θ, the corresponding forms of the solutions are now:

$$u = \bar{u}(h) + RE[u_1(\zeta)e^{i\beta t}]$$
$$v = \bar{v}(h) + RE[v_1(\zeta)e^{i\beta t}] \qquad (3.7)$$
$$\theta = \bar{\theta}(h) + RE[\theta_1(\zeta)e^{i\beta t}].$$

Substituting (3.7) into (3.1), (3.2) and (3.3), combining to eliminate u and θ, and separating the mean and time varying parts of the equations, we obtain two equations in $\bar{v}$ and v_1 of sixth order. The differential equation for $\bar{v}$ and its solution are given by Holton. We can write the equation in v_1 as follows:

$$f(0)v_1 = [D^6 + a_4D^4 + a_2D^2 + a_0]v_1 = \frac{H \sin\phi}{\delta}\theta_r(0)e^{-h},$$

where $D^n = \dfrac{\partial^n}{\partial\zeta^n}$.

The expression for v_1 is then,

$$v_1 = P_0 \sum_{j=1}^{4} D_j e^{-s_j\zeta}, \qquad (3.8)$$

where

$$P_0 = \frac{H \sin\phi}{\delta} \frac{\theta_r(0)}{f(1)},$$

and

$$D_1 = 1$$
$$D_j = -\left[\frac{f(1)H + (1-S_k^2)(1-S_\ell^2)}{(S_j^2-S_k^2)(S_j^2-S_\ell^2)}\right], \qquad j \neq k \neq \ell, \quad 2 \leq j,k,\ell \leq 4$$

In Table 1, the constants in (3.8) and the expressions for u_1 and θ_1 are compared for the two derivations. Holton notes that the amplitudes of the diurnally varying components depend only on α, δ, H and $\sin\phi, \theta_r(0)/\delta$; in this analysis the additional parameter β is important.

The expressions for u_1, v_1 and θ_1 are quite complicated and therefore graphical presentations of the results may be preferable. Figures 3.1 and 3.2 show the amplitude and phase relationships of the harmonically varying component of the forcing function $(-\theta_1 \sin\phi/\delta)$ for ten-degree increments of latitude from 10° N to 60° N. For direct comparison, the parameters other than β have been given the same values as in

TABLE 1

A. Definition of parameters common to both derivations.

ϕ = slope of ground = $\tan^{-1}\left(\frac{dh}{dx}\right)$

δ = ratio of scale height of atmosphere to horizontal scale of motion = $\frac{D}{L}$

ϵ = stability parameter

H = heating parameter

$\alpha = \frac{\sin^2\phi}{\epsilon\delta^2}$

$a = (3\alpha + 3 - H^2)/3$

$b = (-2H^3 + 9H\alpha - 18H)/27$

$A, B = \left(-\frac{b}{2} \pm \sqrt{\frac{b^2}{4} + \frac{a^3}{27}}\right)^{1/3}$

$x_2 = A + B$

$x_{3,4} = \frac{1}{2}[-(A+B) \pm \sqrt{-3}(A-B)]$

B. Comparison of expressions differing in the two derivations

	Holton	MacKay
u_1	$P_0 \sum_{j=1}^{4} (S_j^2 - i)D_j e^{-S_j\zeta}$	$P_0 \sum_{j=1}^{4} (S_j^2 - i\beta)D_j e^{S_j\zeta}$
θ_1	$-\frac{\delta}{\sin\phi} P_0 \sum_{j=1}^{4} [(S_j^2 - i)^2 + 1]D_j e^{-S_j\zeta}$	$-\frac{\delta}{\sin\phi} P_0 \sum_{j=1}^{4} [(S_j^2 - i\beta)^2 + 1]D_j e^{-S_j\zeta}$
a_0	$-\alpha i$	$(H+i\beta)(\beta^2 - 1) - \beta\alpha i$
a_2	$\alpha - 2H + 2Hi$	$\alpha - 3\beta^2 + 1 + 2H\beta i$
a_4	$-(H+3i)$	$-(H + 3\beta i)$
$f(1)$	$(\alpha - H + 1) + i(2H - 3 - \alpha)$	$(\alpha - H - 3\beta^2 + 2 + H(\beta^2 - 1)$ $+ i\beta[2H - 3 - \alpha + (\beta^2 - 1)]$
S_1	1	1
$S_j 2 \le j \le 4$	$[x_j + H/3 + i]^{1/2}$	$[x_j + H/3 + i\beta]^{1/2}$

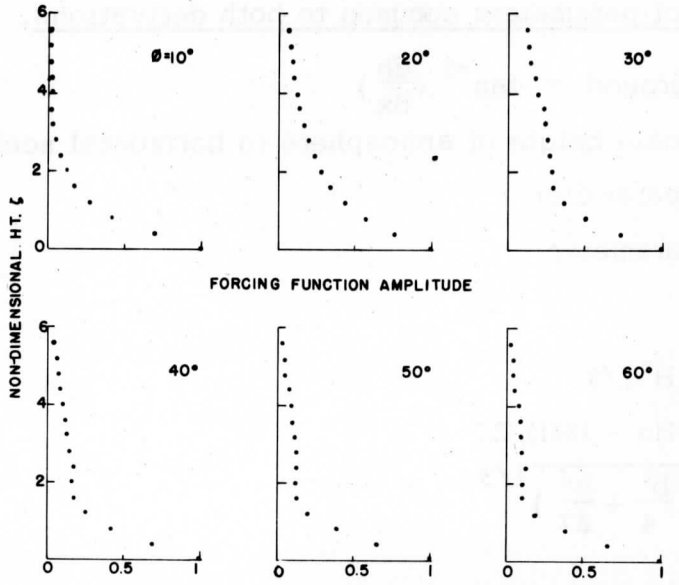

Fig. 3.1. Profiles of forcing function amplitude for ten-degree latitude increments. Nondimensional height $\zeta = \sqrt{f/K}\, Z$.

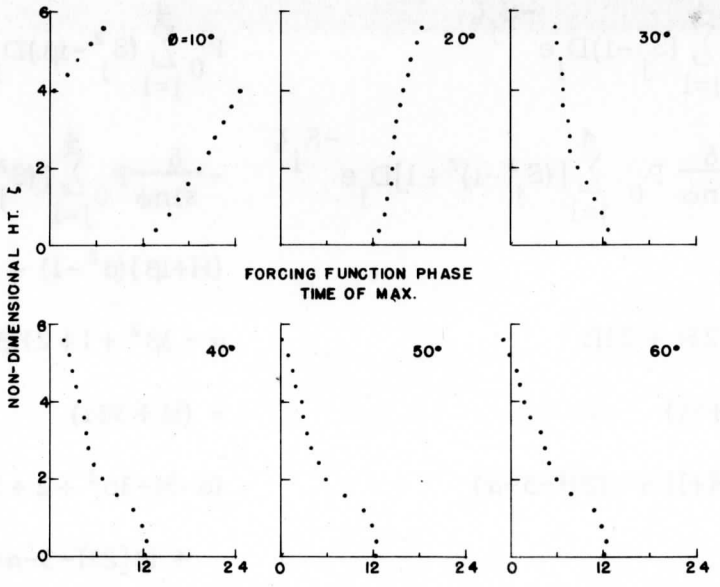

Fig. 3.2. Profiles of forcing function phase for ten-degree latitude increments. Abscissa is in hours after maximum surface temperature.

Holton's presentation. Thus $H = 1$; $\alpha = 0.5$ corresponding to an isothermal atmosphere over a terrain slope of 1/400 and $\frac{\sin\phi\,\theta_r(0)}{\delta} = 1$ corresponding to a radiation temperature amplitude of 8.5° C and a scale velocity of 10 m sec^{-1}.

Equatorward of 30° it appears that the forcing function can be roughly described as having an amplitude that decreases exponentially with height, with the time of maximum increasing linearly with height and at the surface lagging by twelve hours the time of maximum temperature. At latitudes 30° and poleward, the amplitude seems to decrease exponentially up to about $\zeta = 1.6$, to remain constant to about $\zeta = 4.0$ and to decrease linearly thereafter. At the surface, the time of maximum lags by 12 hrs the time of maximum temperature and remains constant to about $\zeta = 0.8$, and decreases with height thereafter, more quickly in the lower layers than the upper. Poleward of 30° the slope of the phase hour with height is greater than equatorward of 30° .

Figures 3.3 and 3.4 present the calculated response of the wind to the forcing function depicted in Figs. 3.1 and 3.2. The amplitude profiles are of a jet type, comparing favorably with those observed during the night of August 31 at O'Neill, Nebraska, with one important exception: the maximum of cross isobaric wind component, u, is larger than observed and occurs at a lower level than the component of the real wind parallel to the geostrophic wind. The phase relationships predicted by Fig. 3.4 do not conform with observations at O'Neill in two important respects: the time of maximum v component is predicted to occur only 4 hrs after the time of maximum surface temperature, or approximately near sunset, and the phase constant of the oscillation is nearly constant with height. Observations at O'Neill suggest that the maximum v component at 100 m lags the surface temperature by about 10.5 hrs and that the winds in the upper layers lead those near the surface.

4. Discussion

At first it appears that there is a conflict between the development in Section 2 and Holton's development outlined in Section 3. Holton states, "We note that the amplitudes U, V, and θ' (u_1, v_1 and θ_1) of the diurnally periodic component...are independent of the geostrophic wind speed." The development of Section 2 on the other hand specifies the geostrophic wind as the driving force for the oscillations. A closer comparison of the two derivations resolves some of the apparent conflict.

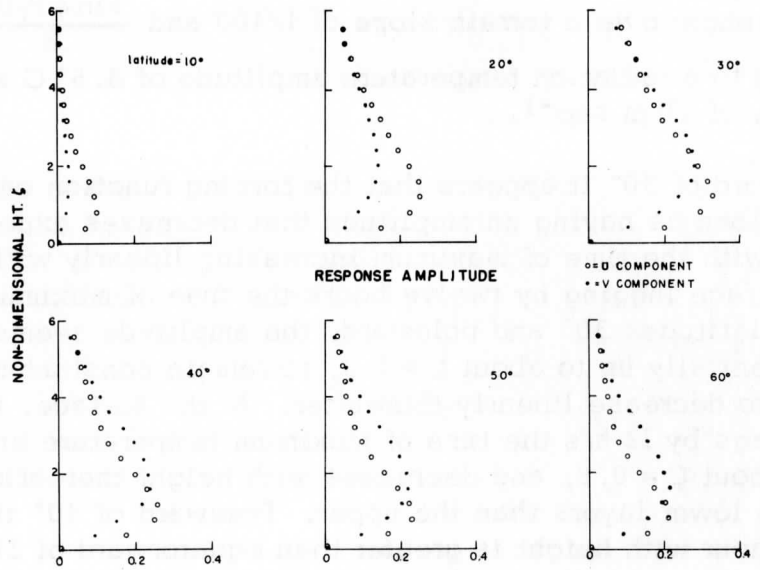

Fig. 3.3. Profiles of amplitude of first harmonic of wind response for ten-degree latitude increments.

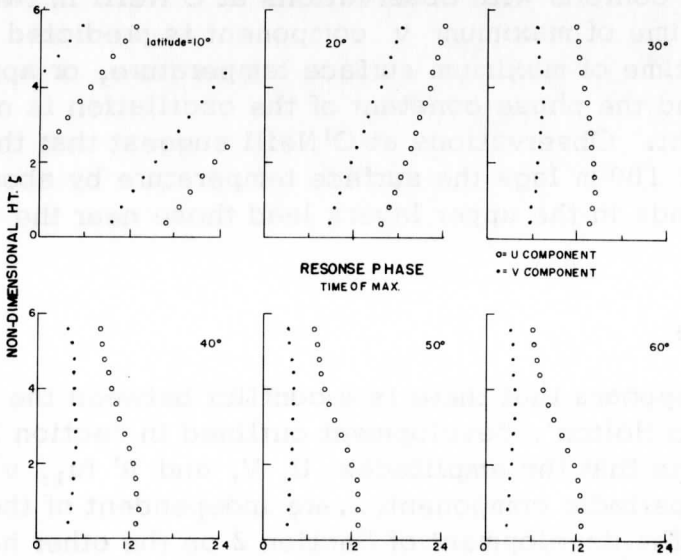

Fig. 3.4. Profiles of phase hour of first harmonic wind response for ten-degree latitude increments. Abscissa is in hours after maximum surface temperature.

The terms which act as the forcing functions in the two models are $-fV_g$ (Eq. (2.1)), in the thermo-tidal model and $-(v_g - \theta \sin\phi/\delta)$ (Eq. (3.1)) in Holton's model. In expanded form, the forcing functions are respectively

$$V_g = \bar{V}_g(z) + V_{g_1}(z) \cos[\omega t + b(z)],$$

and

$$V_g - \theta \sin\phi/\delta = [v_g - \bar{\theta}(\zeta)\frac{\sin\phi}{\delta}] - \frac{\sin\phi}{\delta} |\theta_1| \cos[\beta t + \xi(\zeta)]$$

where

$$\theta_1 = \theta_{1R} + i\theta_{1i}$$

$$|\theta_1|^2 = \theta_{1R}^2 + \theta_{1i}^2$$

$$\tan \xi = \theta_{1i}/\theta_{1R}.$$

The term $(\theta \sin\phi/\delta)$ enters through the nondimensionalization of the pressure gradient term in the equation of motion, and expresses the influence of the ground slope on the oscillation of the pressure gradient force. The form of the forcing function in Holton's model is related to the geostrophic wind through the thermal wind equation. Thus it is suggested that both derivations discussed here can be described as thermo-tidal models.

Both models assume that conditions hold for an equivalent barotropic atmosphere and that the eddy viscosity is a constant in time and height.

Bonner (1965) shows that many cases of low-level jet stream development in the Central United States occur with pressure patterns such that the mean geostrophic wind is from a southwesterly direction. The thermo-tidal model suggests that the diurnal heating cycle will produce north-south oscillations of the thermal wind vector, indicating a baroclinic boundary layer. Closed solutions have been found extending the model developed in Section 2 to such a baroclinic atmosphere and will be reported later.

In order to generalize the models to the case of eddy viscosity varying in time and height, it may be useful to attempt modeling on an analog-digital hybrid computer. In this manner, complicated forms of eddy viscosity which would be awkward to handle mathematically could be employed.

Each model as presented here leaves something to be desired. It would be more satisfying if the forcing function in Lettau's model (Sec. 2) were derived from some form of the thermodynamic energy equation.

However, in Holdon's derivation, which is somewhat more general, the phase relationships predicted for the wind response differ in important respects from those observed. Perhaps if a more exact heating function were used, the predicted and observed phase relationships would conform more closely.

Further extensions of the thermo-tidal model might include attempting to include change of terrain slope in the east-west direction. It is possible that this extension would help explain the velocity concentration near the middle of the slope from the Rockies to the Mississippi (see Hoecker, 1963).

References

Bonner, W., 1965: Statistical and Kinematical Properties of the Low-level Jet Stream. Mesometeorology Research Paper 38, University of Chicago, 38 pp.

Hesselberg, T., and H. U. Sverdrup, 1915: Die reibung in der atmosphere, Veroeff. Geophys. Inst., Univ. Leipzig, 2nd Series, 1.

Hoecker, W. H., 1963: Three southerly low-level jet systems delineated by the weather bureau special pibal network of 1961. Mon. Wea. Rev. 91, 573-582.

Holton, J. R., 1967: The diurnal boundary layer wind oscillation over sloping terrain. Tellus, XIX, 199-205.

Lettau, H.H., 1964: Preliminary note on the effects of terrain slope on low-level jets and thermal winds in the planetary boundary layer. Section 4 of Studies of the Effects of Variations in Boundary Conditions on the Atmospheric Boundary Layer, Department of Meteorology, University of Wisconsin. Annual Report, Contract DA-36-039-AMC-00878, USAERDA, Fort Huachuca, Arizona.

----------, 1967: Small to large-scale features of boundary layer structure over mountain slopes, Proc. Symposium on Mountain Meteorology, Atmos. Sci. Paper 122, Colorado State Univ., Fort Collins, Colorado.

---------- and Ben Davidson, 1957: Exploring the Atmosphere's First Mile. Two Vol. Pergamon Press, New York and London.

9

NOTE ON AERODYNAMIC ROUGHNESS-PARAMETER ESTIMATION ON THE BASIS OF ROUGHNESS-ELEMENT DESCRIPTION

H. Lettau
Department of Meteorology
University of Wisconsin at Madison

ABSTRACT:

Independent of wind profile analysis, the estimation of the aerodynamic roughness parameter (z_0) of the land/air interface (or, of a micrometeorological site) has previously been based on formulas which relate z_0 empirically to only one descriptive characteristic such as average vertical extent (h*) of the individual roughness element. It is demonstrated that more realistic estimates are obtained by consideration of two additional characteristics of the average obstacle; namely, one scaling factor for the average individual form drag (that is, the silhouette area, s) and another scaling factor for the area distribution (that is, the lot area, S). The simple formula, $z_0 = 0.5\ h^*s/S$, is proposed which is derived essentially from results of systematic out-of-doors wind profile modification experiments (under control of surface roughness, along the fetch upwind of an anemometer mast, by distributing, at various area density, several hundred easily handled obstacles, such as commercial bushel baskets, on the originally very smooth ice surface of Lake Mendota). The above "bushel basket formula" for z_0 is applied in an estimate of natural and man-made constituents of aerodynamic roughness at the test site near Davis, California, for the two weeks period of a cooperative micrometeorological field experiment (sponsored in Spring of 1967, by the U.S. Army Activity at Fort Huachuca, Arizona), during which there were forty pieces of equipment (including towers, masts, instrument stands, etc.) distributed over about 4000 m^2 of a short-grass field. It is shown that the equipment contributed probably a significant fraction to the "natural" z_0-value.

1. Introductory Remarks

It is not difficult to estimate fairly accurately, without detailed numerical analysis the aerodynamic roughness parameter (z_0, cm) at a new micrometeorological site, after an anemometer mast has been installed and the first wind-profile data plot on semilogarithmic graphs can be inspected. More challenging is the problem to estimate a z_0-value strictly based on a visual site survey and exclusively using a yardstick and metric measurements to describe the characteristic roughness elements. Recently I found myself challenged in this respect after having responded to an invitation for a brief visit at Davis, California during one day of the two-weeks period in Spring of 1967, when the U.S. Army sponsored micrometeorological cooperative field experiment was in progress. The real challenge was that the well known experimental field site surrounding the unique subterranean Davis lysimeter at that time was dotted by an unusual number of instrument stands, masts, and towers brought to the site by the various participating groups. It occurred to me to ask if it would be possible to separate a z_0-value due to the original grass cover from that due to the various pieces of equipment at the site. It appeared that during the days of the experiment the effective overall aerodynamic roughness parameter of the field might have been larger than before and after. To answer this question some results of systematic micrometeorological research conducted previously at the University of Wisconsin, in the form of controlled roughness modification experiments on the ice of Lake Mendota, proved useful, as shall be shown below.

The determination of the roughness parameter with the aid of measured wind profile data is also not without problems even when all instrumental errors are properly eliminated by anemometer matching and calibration. The problem arises from the fact that the true reference level of a logarithmic law (or its supplemented form for diabatic surface layers), is not a priori known, so that the determination of a "zero-plane displacement" is required in addition to z_0. Occasionally there appears some confusion in the literature concerning these two lengths. To clarify the difference let it again be stated that z_0 is, ideally, an absolutely fixed surface characteristic of the site, whereas the zero-plane displacement is the corrective height increment between the mathematically defined zero level of a mathematical model of the wind profile and the arbitrary datum level from which anemometer heights are measured (usually the physical ground surface at the arbitrary point just beneath the vertical array of anemometers, without consideration of ground structure upwind of this point). An objective method for the simultaneous derivation of the two length parameters was developed and applied by Lettau (1957), later adapted by Robinson (1962) for machine computation, and more recently extended by Stearns (unpublished)

to include the consideration of diabatic effects. The Lake Mendota experiments in Wisconsin, however, served readily to clarify the fundamental difference between the two length parameters experimentally. While z_0 could be artificially increased by obstacle layouts, the displacement length could be controlled independently by raising the entire mast array of anemometers vertically by a known height increment. It follows that z_0 must be invariant with respect to vertical mast positions, while the zero plane displacement must vary by exactly the same amount as the mast assembly was moved.

2. Roughness Parameter Formulas

For a recent summary of pertinent University of Wisconsin work, see Lettau (1967a), which is a reference article dealing with general problems of micrometeorological control in out-of-doors experiments, including a discussion of Kutzbach's (1961) experiments on wind profile modification by fields of bushel baskets (several hundreds of them) laid out, and withdrawn systematically, on the ice of Lake Mendota. With such deliberate roughness modification upwind of an anemometer mast, the roughness parameter along about 50 m wind fetch was made to vary in a controlled fashion between limits of about 0.01 and nearly 10 cm. The results of these experiments were combined with conventional wind tunnel data concerning the aerodynamic drag properties of air foils due to rivet heads, etc.; see Schlichting (1965), or corresponding fluid dynamics texts. In a slight simplification of Kutzbach's results, I proposed the following version of the relationship:

$$z_0 = 0.5\, h^* s/S \qquad (1)$$

where h^* = average vertical extent, or effective obstacle height (cm), s = silhouette area (cm^2) of the average obstacle, or area (measured in the vertical-crosswind-lateral plane) "seen" by the wind in the approach towards one characteristic individual obstacle, and S = specific area, or lot area (cm^2) measured in the horizontal plane or, on the plane described by the local average earth/air interface; if n = total number of roughness elements (or obstacles) on a site of total area A (cm^2), it follows that $S = A/n$. It can be suggested that the numerical factor of 0.5 in Eq. (1) corresponds to the average drag coefficient of the characteristic individual obstacle of silhouette area s. For a relatively large variety of S-values, with an additional relatively small and supplementary control of h^* and s, Kutzbach's "bushel basket" experiments demonstrated that Eq. (1) produces z_0-estimates which agree normally within about $\pm$ 25% with the results of detailed analysis of measured wind profiles.

Equation (1) differs significantly from formulas employed previously in the meteorological literature; reference may be made to the summary in Sellers (1965, p. 150) showing that various authors employed relationships of the form

$$\log z_0 = \log a + b \log h^*; \quad \text{or,} \quad z_0 = a\, h^{*b} \qquad (2)$$

where a and b are empirical constants (of which b is a number). Sellers (1965, p. 151) states that Tanner, Pelton, Kung and others have suggested b-values between 0.99 and 1.42. If h^* is plant height in a field, the relationship (2) is claimed to express z_0 quite adequately.

Obviously, the appearance of only one metric parameter (h^*) is restrictive. To exemplify the practical verification of the two different z_0-formulas, let us first consider Eq. (2); Table 1 summarizes z_0-predictions, including the ratio h^*/z_0, if the results of a regression equation derived by E. Kung (1963) is used, as referenced by Sellers (1965, p. 151).

Table 1. Estimated roughness length z_0, for a systematic variation of h^* in Eq. (2) (corresponding approximately to heights of listed types of obstacles), and resulting ratio h^*/z_0 if $z_0 = 0.058\, h^{*1.19}$.

h^* (cm)	Obstacle Type	z_0 (cm)	h^*/z_0
1000	Forest trees, houses	214	5
100	Field crops, tall grasses	13.8	7
10	Lower grasses, weeds	0.80	11
1	Bare soils	0.058	17
0.1	Sand flats	0.0036	27

Obviously, Eq. (2) fails to predict any differences in z_0 if one compares two sites on which roughness elements of the same h^*-value occur in significantly different spatial distribution. For example, consider a uniform class of sizable roughness elements and two reference areas, of 600 m each, on the same ice-covered lake, and assume that one is dotted by 500 roughness elements (which means relatively close spacing, or a lot area of $S = 1.2\ m^2$) while there are only 50 roughness elements of the same type on the other (which means a more generous lot area of $S = 12\ m^2$). According to Eq. (1), the area where $S = 1.2$ m will have a z_0-value ten times as large as the area where $S = 12\ m^2$. However, Eq. (2) would predict the same z_0-value as long as h^* remains the same, unless there is independent justification for a change in the constants a or b. In another example, let us think of two, three or more distinct types or classes of roughness elements which coexist randomly on one site, each class having their characteristic but different h^*-values but also different shape as well as lot area adjusted just so that each produces the same z_0-value when

considered separately. Here again, Eq. (2) would produce different and probably wrong results. Table 2 summarizes two examples of the first type, and one example of the second type.

Table 2. Estimates of roughness length z_0 employing Eq. (1) for two cases of equal obstacle type with different lot areas, and one case of coexisting three different obstacle classes as well as lot areas, but distributed such that the aerodynamic roughness length is the same.

Obstacle Type, Class	h^* (cm)	s (m^2)	S (m^2)	z_0 (cm)	h^*/z_0
Bushel baskets on Lake Ice	30	0.12	12	0.15	200
			1.2	1.5	20
Houses of city, "slum" versus "suburban"	500	50	100	125	4
			1000	12.5	40
Sand grains	0.1	1.10^{-6}	$2 \cdot 10^{-6}$	0.025	4
Rocks and pebbles	10	0.01	2.0	0.025	40
Barchan dunes	250	20	$1 \cdot 10^5$	0.025	10^4

The first case described in Table 2 corresponds closely to some of Kutzbach's Lake Mendota experiments mentioned before. The z_0-value of the undisturbed ice surface was slightly less than 0.015 cm. Hence, Eq. (1) in combination with the data shown in Table 2 would suggest that for less than about five bushel baskets per 600 m^2, or a lot area in excess of 120 m^2, the micro-structure of the ice would be the dominating roughness. This is a very natural limit condition which demonstrates that beyond a certain lower threshold value of area density we cannot speak any more of the statistical action of roughness elements but must consider the individual air flow around each obstacle separately. The condition is comparable with the statistical statement, that one tree per square mile is not a forest, but with more than about 1000 trees per square mile we certainly can speak of a forest.

The second case in Table 2 is a self-suggestive extrapolation of the bushel basket experiment, contrasting geometrically similar large roughness elements as houses in residential areas of the older type with the ampler suburban spread due to larger lot areas, thus explaining the "slum" as the rougher neighborhood. The third case illustrates an application of Eq. (1) to conditions that correspond rather realistically to those which Professor Stearns and myself encountered in the Peruvian desert during a University of Wisconsin expedition devoted to micro- and mesometeorological studies of wind erosion; reference is made to Lettau (1967b, p. 12). It can be added that the wind profile structure

in this desert suggested an "observed" z_0-value of 0.02 cm; see Lettau (1967a, p. 12). The highly intriguing results of equal z_0-contribution by obstacles ranging from grains to massive dunes (that is, a range of h^* over four powers of ten) may be possible due to the fact that this desert is certainly wind-formed as evidenced by the perfect crescent shape of the barchans, which range in crest height from about 0.5 m to 5 m; reference can be made to Hastenrath (1967). The silhouette area of these dunes was described by K. and H. Lettau (1969).

An independent testing of Eq. (1) was recently reported by Weller (1968, p. 68) concerning the aerodynamic roughness parameter at a micrometeorological site on an antarctic inland-ice plateau near Mawson. According to Weller, the typical cusped blue ice surface was characterized by obstacle heights, silhouette areas, and lot areas as follows:

$$h^* = 2 \text{ cm}; \qquad s = 5 \text{ cm}^2; \qquad S = 25 \text{ cm}^2,$$

whereupon Eq. (1) predicts $z_0 = 0.2$ cm. Weller evaluated wind profile data at this station and found a "measured" value of $z_0 = 0.23$ cm, which seems to be in fair agreement with the prediction.

3. Site Roughness Increase Due to Micrometeorological Equipment

Let us return now to the specific problem of the aerodynamic roughness length for the site of the micrometeorological cooperative field experiment at Davis, California. On the day of my visit (29 April, 1967), I estimated for the grass cover the following characteristics:

$$h^* = 10 \text{ cm}; \qquad s = 4 \text{ cm}^2; \qquad S = 16 \text{ cm}^2,$$

whereupon Eq. (1) predicts $z_0 = 1.25$ cm. Incidentally, if mowing of the grass would reduce h^* by, let's say, about 30%, the silhouette area would be reduced by the same amount or less, while the lot area remains unaltered; the effect would be an approximate reduction of z_0 by about 50%.

A visual impression was that perhaps the assembled instrument masts and stands contributed just as much to the effective aerodynamical roughness of the site as the difference between the unmowed and mown grass. In the area of about $A = 4000 \text{ m}^2$, I counted a total number of forty ($n = 40$) distinct "obstacles"; in other words, each individual instrument mast, stand, tower, etc., occupied on the average a lot area of about $A/n = S = 100 \text{ m}^2$. According to the results of bushel basket experiments discussed in connection with Table 2, this S-value could be critical, depending on the other two characteristics h^* and s. Since there was no measurement activity on that day, I walked from instrument stand to

instrument stand and estimated, with the aid of a yardstick, each height (h^*) as well as silhouette area (s). The latter estimate was problematic, since the metric evaluation should have been weighted by the aerodynamic quality of the instrument stand, or its form-drag coefficient. This was seen to be especially important for those profile masts which were reasonably slender but supported by an intricate system of guy wires. The results, summarized in Table 3, can be taken only as indicating orders of magnitude; a deliberate attempt was made to remain on the conservative side in the judgment of individual silhouette areas.

Table 3. Results of estimates of characteristic height (h^*) and silhouette area (s) of the total of 40 instrument masts and stands on the area (about 4000 m^2) of the micrometeorological field experiment at Davis, California, on 29 April 1967.

Range of h^*(cm)	Number	Class Average of h^* (cm)	Class Average of s (m^2)
< 16	5	10	0.008
16 - 50	8	40	0.070
51 - 200	10	120	0.140
201 - 400	11	300	0.350
401 - 800	5	600	0.600
> 800	1	1500	1.500
Weighted Mean:		240	0.25

According to Table 3 and the size of the area (A = 4000 m^2), the following data set characterizes the aerodynamic roughness properties of the site instrumentation during the cooperative field experiments at Davis:

$$h^* = 240 \text{ cm}; \quad s = 0.25 \text{ m}^2; \quad S = 100 \text{ m}^2,$$

whereupon Eq. (1) yields $z_0 = 0.3$ cm. This may represent an underestimate because guy wire resistances were not considered as factors in determining the effective silhouette area for wind drag. If Eq. (2) would be applied with the numerical coefficients as specified in the caption of Table 1, the result would be $z_0 = 41$ cm for $h^* = 240$ cm which obviously is an entirely unrealistic value.

Before I departed from California on 30 April 1967, I wrote down the results and some brief comments including those presented in this section. It was very much appreciated that the field coordinator took good care of the manuscript and its immediate distribution in mimeographed form among the participants under the title "Essay on the aerodynamic

roughness of the site of the 'MiMeEx' at Davis, California, 1967." Comprehensive analyses of the large amount of profile data in connection with detailed measurements of boundary fluxes are still in progress. But it can be mentioned that Professor C. Stearns (who was at Davis in charge of the University of Wisconsin group responsible for wind profile measurements, which had been achieved with the aid of three identical anemometer masts forming a site-circumscribing triangle) informed me that "measured" z_0-values varied within the limits of 0.8 to 1.4 cm during the duration of the experiment. This "a posteriori" overall result appears to be in satisfactory agreement with the "a priori" estimate made without the benefit of profile analysis. More detail will be reported by Professor Stearns in a forthcoming paper.

4. Conclusions

Equation (1) can only be used when the obstacle field is of sufficient extent in the upwind direction of an anemometer mast. This condition is, of course, not satisfied in the above particular application where the anemometer mast itself is assumed to act as a roughness element, while other masts will be in an upwind position only for certain wind directions. At distances beyond a few hundred meters, the Davis site is surrounded by substantial obstacles to air flow, like lines of trees; a consideration of their effects should be incorporated in a more detailed study. The question remains whether the z_0-value due to the supplementary equipment on the site should be algebraically added to the original z_0 of the natural grass cover, or should the composite z_0 value be calculated as a weighted mean between the two individual contributions. This question could perhaps be clarified by a new set of controlled micrometeorological out-of-doors experiments employing two distinct classes of roughness elements, at varying absolute and relative area densities, on the same field. Recalling that in the US system of dry measures, 1 bushel (equivalent to 35.2 liters) equals 64 pints, the proposed new experiments could consist of intermingling "bushel baskets" with "pint baskets." It may be concluded that a combined "bushel and pint basket formula" for aerodynamical roughness may be useful for expressing the quality of a site as a micrometeorological test area. Furthermore, roughness parameter estimates could be made more securely than before, for any continental area for which topography and land use are defined. Knowledge of the z_0 value, in combination with a given over-all horizontal pressure gradient, would yield the surface-Rossby number and, subsequently, as shown by Lettau (1962), via the geostrophic drag coefficient an estimate of the surface shearing stress as well as energy dissipation in the atmospheric boundary layer.

References

Hastenrath, S. (1967): "The Barchans of the Arequipa Region, Southern Peru," pp. 301-331. Z.f. Geomorphol., Vol. 11.

Kung, E. (1963): "Climatology of Aerodynamic Roughness Parameter and Energy Dissipation in the Planetary Boundary Layer of the Northern Hemisphere," pp. 37-96, in Studies of the Effects of Variations in Boundary Conditions on the Atmospheric Boundary Layer, Annual Report 1963, Dept. of Meteorology, University of Wisconsin, Madison.

Kutzbach, J. (1961): "Investigations of the Modification of Wind Profiles by Artificially Controlled Surface Roughness," pp. 71-113, in Studies of the Three Dimensional Structure of the Planetary Boundary Layer, Annual Report 1961, Dept. of Meteorology, University of Wisconsin, Madison.

Lettau, H. (1957): "Computation of Richardson Numbers, Classification of Wind Profiles, and Determination of Roughness Parameters," pp. 328-336, in Exploring the Atmosphere's First Mile, Vol. I, (H. Lettau and B. Davidson, eds.), Pergamon Press, London and New York, 376 pp.

Lettau, H. (1962): "Theoretical Windspirals in the Boundary Layer of a Barotropic Atmosphere," pp. 195-212, Beitr. Phys. Atmosph., Vol. 35.

Lettau, H. (1967a): "Problems of Micrometeorological Measurements," pp. 3-40, in The Collection and Processing of Field Data (Proceeding of a CSIRO Symposium, edited by E. F. Bradley and O. T. Denmead), Interscience Publishers, J. Wiley and Sons, Inc., New York.

Lettau, H. (1967b): "Small to Large-Scale Features of Boundary Layer Structure over Mountain Slopes," pp. 1-70, in "Symposium on Mountain Meteorology" (Proceedings edited by E. R. Reiter and J. L. Rasmussen), Atmospheric Science Paper No. 122, Dept. of Atmosph. Science, Colorado State University, Fort Collins.

Lettau, K., and H. (1969): "Bulk Transport of Sand by the Barchans of the Pampa de La Joya in Southern Peru," pp. 111-121, Z.f. Geomorphol., Vol. 13.

Robinson, S. (1962): "Computing Wind Profile Parameters," pp. 189-190, Journal Atmosph. Sciences, Vol. 19.

Schlichting, H. (1965): Boundary Layer Theory, 647 pp. Pergamon Press, New York.

Sellers, W. (1965): Physical Climatology, 272 pp., University of Chicago Press, Chicago and London.

Weller, G. (1968): "The Heat Budget and Heat Transfer Processes in Antarctic Plateau Ice and Sea Ice," 155 pp. ANARE Scientific Reports, Series A (IV), Glaciology, Publication No. 102, Melbourne, Australia.

THE SURFACE HEAT BUDGET OF THE PAMPA DE LA JOYA, PERU

Charles R. Stearns
Department of Meteorology
The University of Wisconsin at Madison

ABSTRACT:

The surface heat budget for the absolutely dry soil of the Pampa de La Joya, Peru, a portion of the Altacama Desert, was determined for three round-the-clock periods in July, 1964. The diurnal variations are described by the mean value, and amplitude and phase angle of the first three harmonics. The measurements include global insolation, net radiation, soil heat flux density, sensible heat flux density, surface temperature and air temperature at 20, 40, 80, 160 and 320 cm. The instruments used are described, and an estimate of the errors in measurement is made for each.

1. Introduction

During July 1964, a micrometeorological field program in the Pampa de La Joya, Peru, was inaugurated by H. H. Lettau and supported by the Center for Climatic Research, Department of Meteorology, University of Wisconsin. The primary purpose of the expedition was to study the dynamics of the air flow which cause the migration of the crescentic sand dunes, commonly called barchans, present on the Pampa de La Joya. Finkel [1], Hastenrath [2], and H. and K. Lettau [3] have described the barchans in detail. Lettau [4] has discussed certain aspects of the local circulation and dune migration.

The western coast of South America, about 5 deg S to 30 deg S latitude between the Pacific Ocean and the Andes Mountains, is the Altacama desert, one of the world's most arid regions. La Joya is located at 16 deg 44 min S latitude and 71 deg 51 min W longitude between Mollendo and Arequipa as shown in Figure 1. The area shown in Fig. 2 is part of the Pampa de La Joya indicating the barchan field and the location of the barchan "Finkel 26" which was the camp site for the expedition. The character of the desert area where the measure ments were made may be seen in Fig. 3.

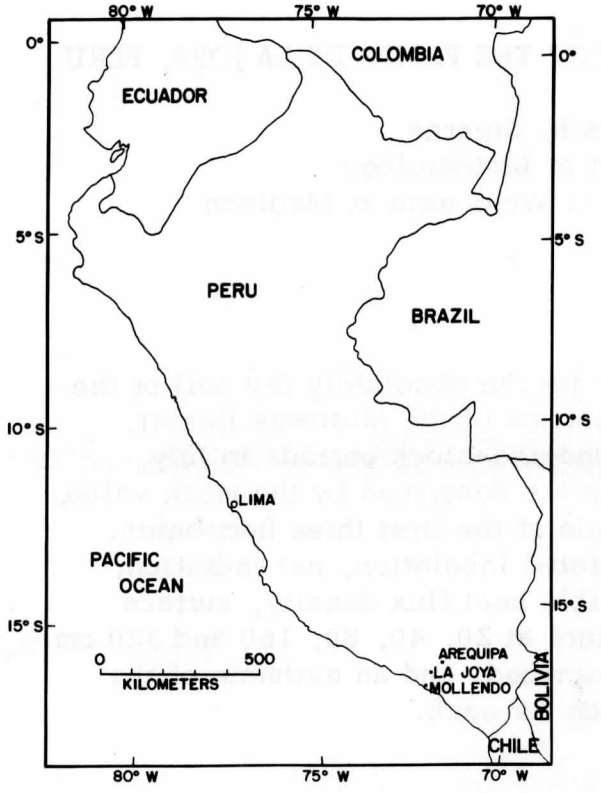

Fig. 1. Map of Peru indicating the location of Arequipa, La Joya and Mollendo.

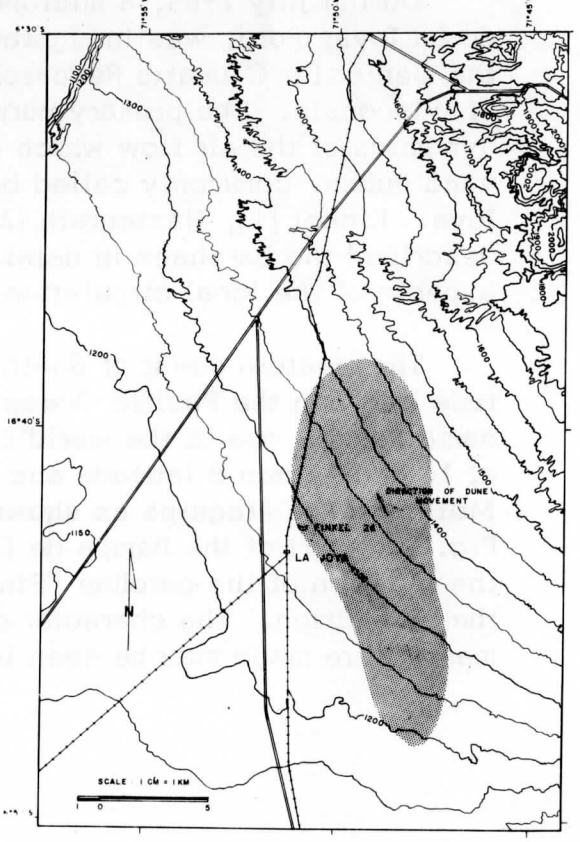

Fig. 2. Topographic map of the Pampa de La Joya, Peru. The shaded area indicates the barchan field and the location of the barchan "Finkel 26" near which the heat budget measurements were made.

Fig. 3. Barchan in the area of "Finkel 26" showing the general character of the desert surface.

The purpose of this paper is to analyze the diurnal variation of heat budget constituents and related measurements in an absolutely dry climate, thus to increase the available surface heat budget data in a meteorologically neglected but interesting area.

2. Theory of the Surface Heat Budget

The heat budget at the air-soil interface may be represented by the equation

$$R_0 = S_0 + Q_0 + E_0 + P_0$$

where R_0 = net radiative heat flux density (ly/min), S_0 = soil heat flux density (ly/min), Q_0 = sensible heat flux density to the air (ly/min), E_0 = latent heat flux density to the air (ly/min), and P_0 = heat flux density required for photo chemical reactions. The subscript 0 refers to the surface. The lack of soil moisture, rainfall and condensation on the Pampa de La Joya, apparent in the absence of plant growth, allows the assumption that $P_0 = 0$ and $E_0 = 0$. The heat budget equation then reduces to the extreme desert-type heat budget in the form

$$R_0 = S_0 + Q_0. \qquad (2)$$

The three terms are generally positive during the daytime and negative during nighttime.

The sensible heat flux density to the air may be related to the gradient of potential temperature θ' and an eddy diffusivity for heat K_h in the following form:

$$Q_0 = -\rho c_p K_h \theta' \qquad (3)$$

where ρ is the air density (gm cm^{-3}), c_p is the specific heat per unit mass for air (cal gm^{-1} K^{-1}), K_h is the eddy diffusivity for heat ($cm^2 sec^{-1}$) and θ' is the vertical potential temperature gradient in the air (K cm^{-1}). The assumptions made are that the flux of sensible heat is directly proportional to the potential temperature gradient in the air, and that there is no divergence of sensible heat in and below the air layer where the potential temperature gradient is measured.

3. Measurements and Instrumentation

The micrometeorological measurements made on the Pampa de La Joya, Peru, included the soil heat flux density at -0.5 cm, extrapolated

surface temperature at -0.1 cm, net radiation, and air temperature at five levels. A detailed description of the measurements system is given by Stearns [5].

The soil heat flux density was measured by a microscope slide "flux plate" with 100 thermocouple junctions across the plate. The flux plate was calibrated "in situ" by the soil temperature integral method assuming a volumetric heat capacity of 0.286 cal cm^{-3} deg C^{-1} for the desert sand (Stearns [6]).

Net radiation was measured by a modified Suomi-Kuhn [7] shielded net radiometer (Fig. 4) and a Suomi [8] ventilated net radiometer. The ventilated radiometer was calibrated by shading, against an Eppley pyranometer, but the ventilated radiometer was not operating properly prior to July 12, 1964, so only the shielded radiometer data were available from July 8 to July 12, 1964. Figure 5 is a comparison between the two radiometers. For the heat budget calculations, the shielded radiometer was corrected to the ventilated radiometer according to Figure 5 in order to have radiation data for the period July 8 to July 12, 1964 (Stearns [5]).

An estimate of the soil surface temperature was made by extrapolating the -0.5, -2.0, and -5.0 cm temperature to -0.1 cm using Lagrange's method of fitting a parabola through three points in order to predict the fourth. The actual equation used was

$$T_{-0.1} = 1.48\, T_{-0.5} - 0.555\, T_{-2.0} + 0.74\, T_{-5.0} \qquad (4)$$

where T is temperature (deg C) and the subscript indicates the depth of the temperature used or estimated. Commencing July 12, 1964, an independent estimate of the soil surface temperature was obtained by a nickel-wire resistance thermometer resting on the soil surface. A comparison between the resistance thermometer temperature and the extrapolated soil temperature is shown in Fig. 6. When the surface temperature was changing rapidly, the extrapolated surface temperature lagged about two deg C behind the resistance thermometer temperature (Stearns [5]).

The air temperature profile differences were measured by 10 junction thermopiles between height intervals of 20 to 40, 40 to 80, 80 to 160, and 160 to 320 cm. The thermopiles were ventilated at about 5 mps and shielded from solar radiation. The absolute reference temperature was measured by a 1N-2326 diode thermometer checked occasionally during recording against a mercury-in-glass thermometer (Stearns [5]).

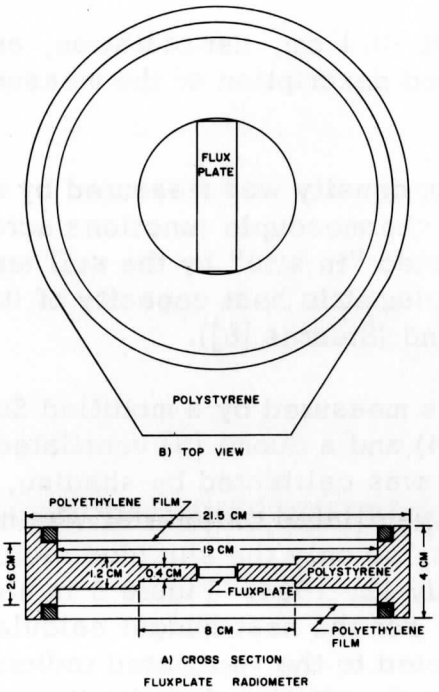

Fig. 5. Comparison between the ventilated net radiometer and the uncorrected shielded radiometer and a shading calibration of the two instruments. The calibration factor for the ventilated radiometer was the mean obtained from several shadings using an Eppley pyranometer as the radiation standard.

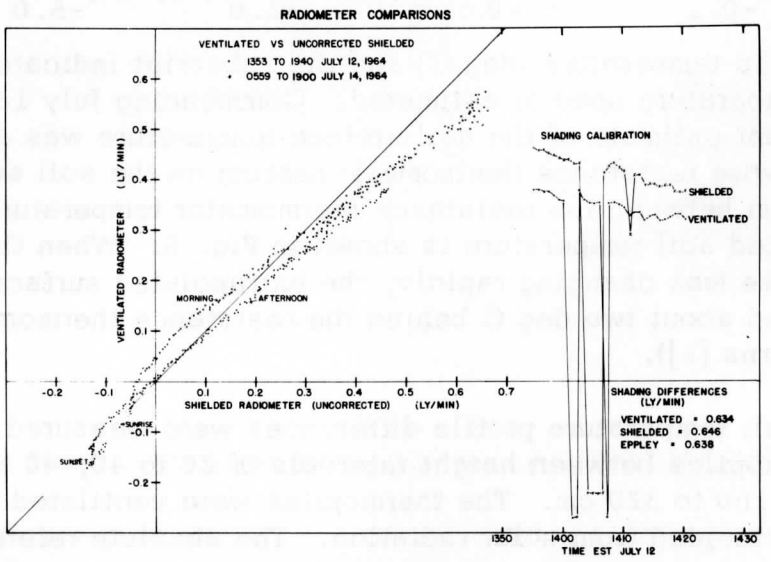

Fig. 4. Construction details of the shielded radiometer used for measuring net radiation on the Pampa de La Joya, Peru. The radiation detector is a blackened flux plate with two layers of 0.5 mil polyethylene film on each side to shield the flux plate from ventilation.

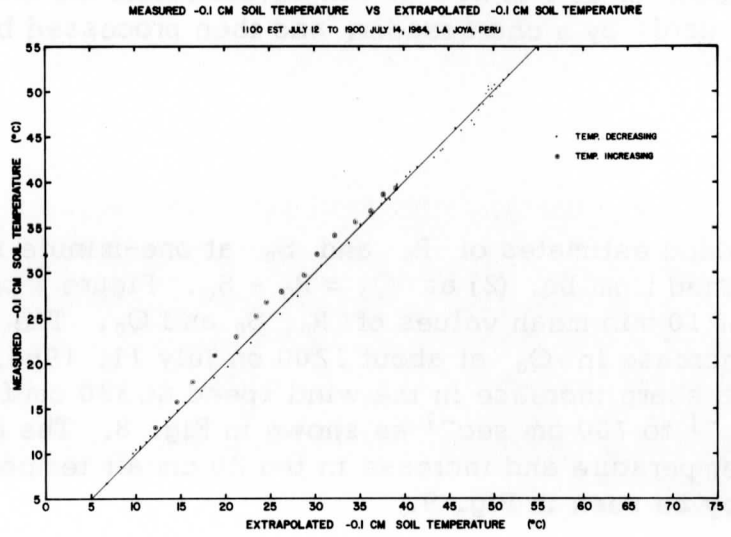

Fig. 6. Ten min mean soil temperature at the nominal depth of -0.1 cm as measured by an 0.001 mil nickel wire resistance thermometer versus the temperature determined by the extrapoliation of one minute sub-soil temperatures to -0.1 cm and then averaged for 10 min periods. Allowance was not made for phase lags in the extrapolated sub-soil temperatures.

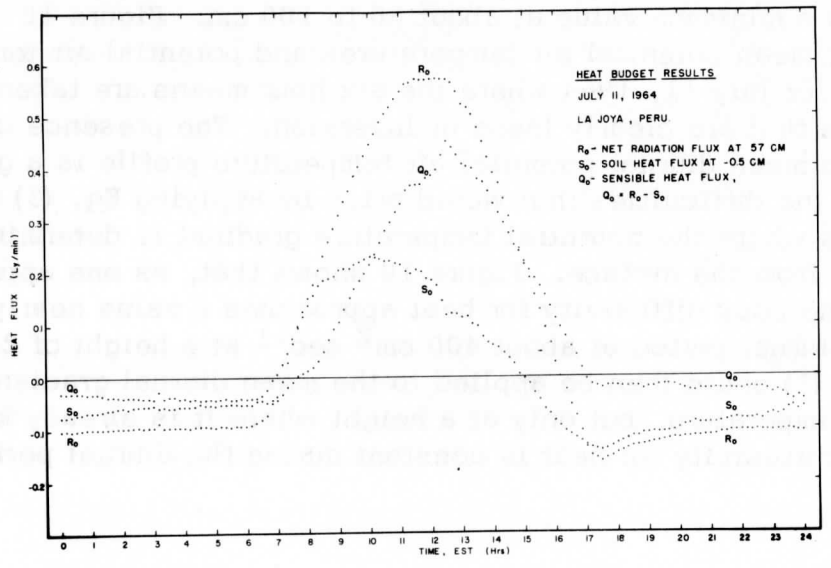

Fig. 7. The heat budget on the Pampa de La Joya, Peru, for the diurnal period of July 11, 1964.

The data were recorded at one-minute intervals on a 24 point Honeywell Electronic Recorder of 0 to 2.5 mv range, read from the charts directly to punch cards by a chart reader, and then processed by electronic computer.

4. Results

The data yielded estimates of R_0 and S_0 at one-minute intervals with Q_0 determined from Eq. (2) as $Q_0 = R_0 - S_0$. Figure 7 presents a diurnal cycle of 10 min mean values of R_0, S_0 and Q_0. The slight dip in S_0 and increase in Q_0 at about 1200 on July 11, 1964, was associated with a sharp increase in the wind speed at 320 cm from about 400 cm sec^{-1} to 700 cm sec^{-1} as shown in Fig. 8. The decrease in soil surface temperature and increase in the 20 cm air temperature at the same time may be seen in Fig. 9.

The air temperature at 5 levels, heat budget and surface temperature were analyzed harmonically and the results are given in Table 1 for three diurnal periods on the Pampa de La Joya, Peru. Periods were selected so that the available data was nearly continuous with some interpolation necessary during the nighttime. The differences between the three diurnal periods for the mean values, and amplitudes and phase angles of the first and second harmonics are negligible. The sky remained free of clouds.

An examination of the diurnal period means of the air temperature profile reveals a minimum value at about 80 to 100 cm. Figure 10 illustrates six hour mean potential air temperatures and potential air temperature gradients for July 11, 1964 where the six hour means are taken over periods of time that are clearly lapse or inversion. The presence of the minimum in the mean diurnal potential air temperature profile is a good illustration of the difficulties that would arise by applying Eq. (3) to diurnal periods where the potential temperature gradient is determined at some distance from the surface. Figure 10 shows that, as one approaches the surface, the eddy diffusivity for heat approaches a value nearly constant for the diurnal period at about 400 cm^2 sec^{-1} at a height of 28.2 cm. Equation (3) could then be applied to the mean diurnal gradient of potential air temperature, but only at a height where it is already known that the eddy diffusivity for heat is constant during the diurnal period.

5. Accuracy

The use of only one set of instruments makes it difficult to estimate the accuracy of the measurements. Figure 4 shows that the two net radiation instruments were not in the same plane and it could be that

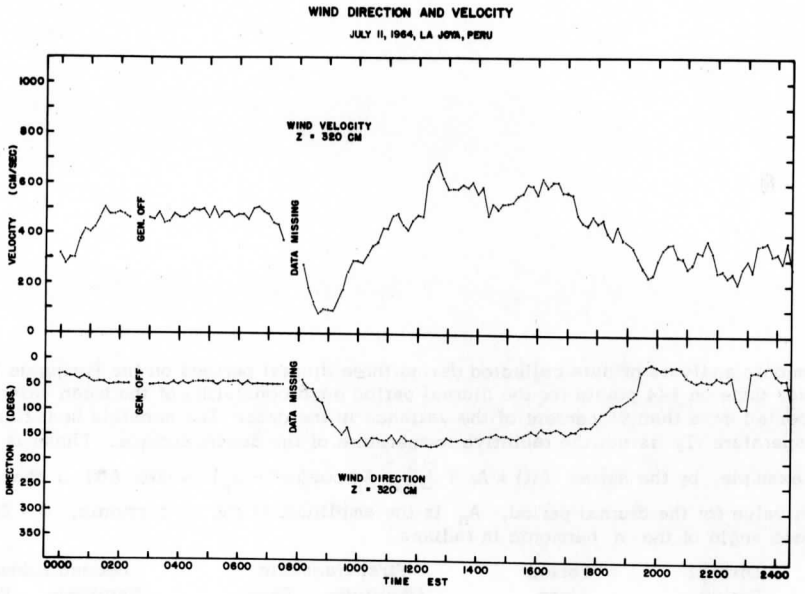

Fig. 8. Wind direction and speed at 320 cm height above the surface of the Pampa de La Joya, Peru. The increase in wind speed at 1200 EST was associated with an increase in Q_0 and a drop in surface temperature at the same time.

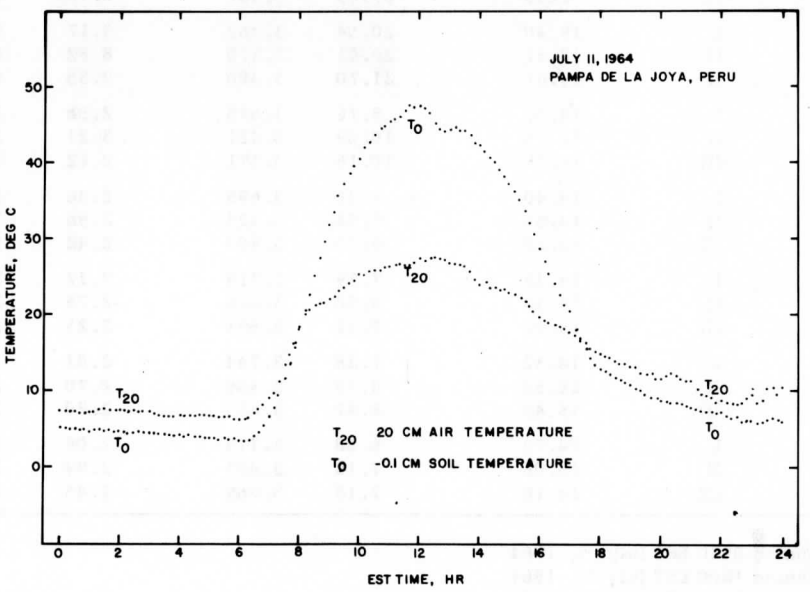

Fig. 9. Soil temperature at -0.1 cm estimated by extrapolation from below and the 20 cm air temperature for the diurnal period of July 11, 1964 on the Pampa de La Joya, Peru. The drop in the -0.1 cm soil temperature at 1200 EST is associated with an increase in wind speed.

Table 1. The results of the harmonic analysis of data collected during three diurnal periods on the Pampa de La Joya, Peru during July, 1964. The harmonic analysis was done on 144 points for the diurnal period each consisting of the mean value of 10 one minute samples. The first three harmonics represented more than 98 percent of the variance in the data. The sensible heat flux density Q_0 is determined as $R_0 - S_0$ and the surface temperature T_0 is not the radiative temperature of the desert surface. Phase is given in radians and the data may be reconstructed, for example, by the series $A(t) = A_0 + \sum_{n=1}^{3} A_n \cos(n\omega t - \alpha_n)$ where $A(t)$ is the value at time t in hrs from local midnight, A_0 is the mean value for the diurnal period, A_n is the amplitude of the n harmonic, $\omega = 2\pi/24$ is the angular velocity (radians/hr) and α_n is the phase angle of the n harmonic in radians.

		Diurnal Period	Period Mean	First Harmonic Amplitude	First Harmonic Phase	Second Harmonic Amplitude	Second Harmonic Phase	Third Harmonic Amplitude	Third Harmonic Phase
RS	Solar Radiation	I	0.339	0.560	3.142	0.292	0.099	0.054	2.940
	(ly min^{-1})	II	0.339	0.557	3.142	0.289	6.268	0.055	3.044
		III	0.332	0.543	3.142	0.279	0.099	0.053	3.215
R_0	Net Radiation	I	0.066	0.303	3.050	0.182	6.235	0.057	3.065
	(ly min^{-1})	II	0.069	0.299	3.052	0.179	6.232	0.052	3.220
		III	01061	0.288	3.055	0.176	6.236	0.053	3.241
S_0	-0.5 cm	I	0.001	0.139	2.700	0.087	5.857	0.014	2.671
	Soil heat flux density	II	-0.004	0.138	2.658	0.082	5.772	0.019	2.050
	(ly min^{-1})	III	0.002	0.140	2.724	0.082	5.839	0.022	2.169
Q_0	Sensible heat flux density	I	0.065	0.175	3.286	0.106	0.320	0.046	3.226
	(ly min^{-1})	II	0.073	0.180	3.350	0.112	0.277	0.048	3.595
		III	0.059	0.163	3.337	0.105	0.259	0.047	3.667
T_0	-0.1	I	19.40	20.54	3.462	9.17	0.276	0.78	3.365
	Soil temperature	II	18.57	20.53	3.370	8.82	0.153	1.69	2.436
	(deg C)	III	19.67	21.70	3.400	9.55	0.266	1.83	2.874
T_{20}	20 cm	I	14.56	8.76	3.675	2.58	3.180	0.96	0.432
	Air temperature	II	14.79	10.69	3.421	3.21	3.100	1.19	1.611
	(deg C)	III	15.39	10.18	3.571	2.62	3.506	1.08	1.020
T_{40}	40 cm	I	14.40	8.30	3.695	2.36	3.152	1.03	0.424
	Air temperature	II	14.60	9.54	3.423	2.96	3.060	1.24	1.553
	(deg C)	III	15.29	9.70	3.580	2.42	3.480	1.12	1.035
T_{80}	80 cm	I	14.33	7.79	3.714	2.17	3.055	1.09	0.446
	Air temperature	II	14.48	8.92	3.426	2.75	2.990	1.26	1.513
	(deg C)	III	15.27	9.11	3.591	2.23	3.437	1.12	1.028
T_{160}	160 cm	I	14.32	7.28	3.744	2.03	3.151	1.09	0.412
	Air temperature	II	14.54	8.30	3.436	2.70	2.910	1.21	1.486
	(deg C)	III	15.44	8.47	3.613	2.20	3.372	1.10	0.990
T_{320}	320 cm	I	14.72	6.38	3.775	2.09	3.012	1.09	0.589
	Air temperature	II	15.05	7.16	3.493	2.99	2.800	1.00	1.385
	(deg C)	III	16.16	7.18	3.669	2.45	2.994	1.08	0.820

I Diurnal period beginning 0940 EST July 9, 1964
II Diurnal period beginning 1800 EST July 10, 1964
III Diurnal period beginning 1800 EST July 11, 1964

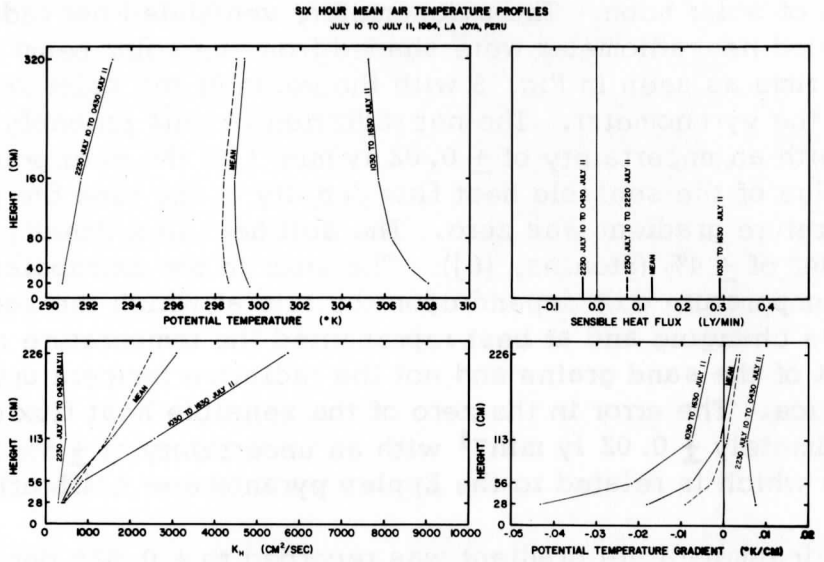

Fig. 10. Height profile of potential air temperature, potential air temperature gradient and eddy diffusivity for heat (K_h) for 1030 July 11 to 1030 July 12, 1964 on the Pampa de La Joya, Peru. The dashed lines are for the 24-hr. mean which contains the two 6-hr. periods of lapse and inversion conditions and "mean" refers to the average of the two 6-hr. periods which are clearly lapse or inversion.

neither instrument was truly horizontal. The use of an Eppley pyranometer as the radiation standard immediately introduces an uncertainty of ± 5% in the calibration of the instrument. The cosine response of the pyranometer is poor at sun elevation angles of less than 30 deg, so calibrations of the net radiometers were done within two hours of solar noon. The pyranometer, ventilated net radiometer and shielded net radiometer were shaded from the solar beam at nearly the same time as seen in Fig. 5 with the value of the solar beam determined by the pyranometer. The net radiation is thus probably known to ± 5% with an uncertainty of ± 0.02 ly min^{-1} in the zero point based on the value of the sensible heat flux density at the time the potential air temperature gradient was zero. The soil heat flux density error is of the order of ± 4% (Stearns, [6]). The error in the extrapolated -0.1 cm soil temperature will depend upon the rate at which the soil temperature is changing and at best represented the temperature of the lower part of the sand grains and not the radiative temperature of the sand surface. The error in the zero of the sensible heat flux density is approximately ± 0.02 ly min^{-1} with an uncertainty of ± 5% in the amplitude which is related to the Eppley pyranometer calibration.

The air temperature gradient was recorded to ± 0.025 deg C, but the standard deviation of a 10 min sample was often of the order of 0.1 deg C. The differences from one level to the next should be within ± 0.025 deg C, but as to whether this represents the air temperature at the nominal height, is open to question. The 80 cm air temperature seems occasionally to be in error relative to 40 and 160 cm, but it was not possible to correct the data and the discrepancy is of the order of ± 0.10 deg C.

6. Conclusions and Future Plans

The excessive dryness and low thermal admittance of the soil (Stearns [6]), result in relatively extreme sensible heat flux density to the air with peak values of 0.4 ly min^{-1}. The small surface roughness of about 0.02 cm (Stearns [5]) contributes to large air-to-surface temperature differences of as much as 20 deg C. Large flux densities of sensible heat to the air coupled with the smooth surface leads to extremes in the vertical gradients of air temperature and wind speed near the surface. The resulting negatively large Richardson numbers permit conclusions on the ratio of the eddy diffusivity for heat to the eddy diffusivity for momentum and thus on profile structure in the surface layer. These results will be presented in the future.

The reliability of the diurnal wind variation in the surface layers combined with the regularity of the diurnal heat budget and the low surface roughness makes the area ideal for the study of diabatic wind and temperature profile structure in the surface layer.

The Peruvian Government plans to irrigate parts of the Pampa de La Joya. It will be of interest to determine how the heat budget and associated parameters reported above may be changed by the proposed modification of the desert surface.

References

1. Finkel, H.J., The Barchans of Southern Peru, J. Geol., 67, 614-647, 1959.

2. Hastenrath, S. L., The Barchans of the Arequipa Region, Southern Peru, Ann. Geomorph.,11, 300-331, 1967.

3. Lettau, K., and H., Bulk transport of sand by the barchans of the Pampa de La Joya in Southern Peru, Z. F. Geomorph., vol. 13, pp. 111-121, 1969.

4. Lettau, H. H., "Small- to large-scale features of boundary layer structure over mountain slopes," Proceedings of the Symposium on Mountain Meteorology, Colorado State University, Fort Collins, Colorado, pp. 1-74, June, 1967.

5. Stearns, C. R., Micrometeorological studies in the coastal desert of southern Peru, Ph.D. thesis, Department of Meteorology, University of Wisconsin, Madison, Wisconsin, 179 pp., 1967.

6. Stearns, C. R., Application of Lettau's theoretical model of thermal diffusion to soil profiles of temperature and heat flux, Journal of Geophysical Research, Vol. 74, No. 2, pp. 532-541, 1969.

7. Suomi, V. E. and P. M. Kuhn, An economical net radiometer, Tellus, X, 1, pp. 160-163, 1958.

8. Suomi, V. E., Matti Franssila, and N. F. Islitzer, An improved net-radiation instrument, J. of Meteor., Vol. 11, pp. 276-282, 1954.

Scanner's note:

This page is blank.

DISTRIBUTION LIST

cys

Department of Defense

(30) Defense Documentation Center
ATTN: DDC-IRS
Cameron Station (Bldg 5)
Alexandria, Virginia 22314

Technical Library
Dir of Defense Research & Engr
Room 3E-1039, The Pentagon
Washington, D.C. 20301

Director, Defense Atomic Sup Agcy
ATTN: Document Library Branch
Washington, D.C. 20305

Department of Defense
Defense Intelligence Agency
ATTN: DIAAP-IES
Washington, D.C. 20301

Spec Asst for Environmental Svcs
Joint Chiefs of Staff
ATTN: Lt Col Hampton
Washington, D.C. 20301

Department of the Navy

Chief of Naval Operations
ATTN: Code 427
Department of the Navy
Washington, D.C. 20325

Naval Ships Systems Command
ATTN: Code 20526 (Tech Library)
Main Navy Bldg, Room 1528
Washington, D.C. 20325

(2) Director
U.S. Naval Research Laboratory
ATTN: Code 2027
Washington, D.C. 20390

AFSC STLO (RTSND)
Naval Air Dev Center
Johnsville, Warminster, Pa. 18974

Office of Naval Weather Svc (Code 80)
Washington Navy Yard (Bldg 200)
Washington, D.C. 20390

Commanding Officer & Director
U.S. Navy Electronics Laboratory
ATTN: Library
San Diego, California 92152

Commander
U.S. Naval Ordnance Laboratory
ATTN: Technical Library
White Oak, Silver Spring, Md. 20910

Officer in Charge
U.S. Navy Weather Research Facility
Bldg. R-48, U.S. Naval Air Station
Norfolk, Virginia 23511

Commandant, Marine Corps (Code A04C)
Headquarters, U.S. Marine Corps
Washington, D.C. 20380

Development Cen, ATTN: C-E Div
Marine Corps Dev & Educ Comd
Quantico, Virginia 22134

Commandant, U.S. Marine Corps
(Code A02F)
Headquarters, U.S. Marine Corps
Washington, D.C. 20380

Commander
U.S. Naval Weapons Laboratory
ATTN: KXR
Dahlgren, Virginia 22448

Ch, Bureau of Naval Weapons
ATTN: Code FASS
Department of the Navy
Washington, D.C. 20315

Ofc of U.S. Naval Weather Svc
U.S. Naval Air Station
Washington, D.C. 20390

Officer in Charge
U.S. Naval Weather Res Facility
U.S. Naval Air Station, Bldg R-28
Norfolk, Virginia 23511

Department of the Air Force

(2) Electronic Systems Division (ESTI)
L. G. Hanscom Field
Bedford, Mass. 01730

(3) AFCRL (CREW-CREU-CRER)
L. G. Hanscom Field
Bedford, Mass. 01730

Hqs, Air Weather Service
ATTN: AWVAE/SIPB
Scott Air Force Base, Ill. 62225

U.S. Air Force Security Service
ATTN: TSG, Vice ATTN: ESD
San Antonio, Texas 78241

Air Proving Ground CTR (PGBPS-12)
ATTN: PGAPI
Eglin Air Force Base, Fla. 32542

Headquarters, AFSC
ATTN: SCTSE
Bolling AFB, D.C. 20332

Commander
29th Weather Squadron (MAC)
ATTN: 29WSOP (CWO Schissler/727)
Richards-Begzur AFB, Mo. 64030

Commander
USAF Air Weather Service (MATS)
ATTN: AWSSS/TIPD
Scott Air Force Base, Ill. 62225

Commander
Air Force Cambridge Res Labs
ATTN: CRZW, 1065 Main Street
Waltham, Mass. 02154

Department of the Army

(2) Chief of Research & Development
Department of the Army
Washington, D.C. 20315

Commanding General
U.S. Army Materiel Command
ATTN: AMCRD-TV
Washington, D.C. 20315

Commanding General
U.S. Army Missile Command
ATTN: AMSMI-RRA, Bldg 5429
Redstone Arsenal, Alabama 35809

(3) Redstone Scientific Info Cen
ATTN: Ch, Document Section
U.S. Army Missile Command
Redstone Arsenal, Alabama 35809

(2) Commanding Officer
Aberdeen Proving Ground
ATTN: Tech Library, Bldg. 313
Aberdeen Proving Ground, Md. 21005

(2) Headquarters
U.S. Continental Army Command
ATTN: AMCMA-RM/3
Washington, D.C. 20315

Commanding General
U.S. Army Combat Dev Command
ATTN: CDCMR-E
Fort Belvoir, Virginia 22060

Chief of Research & Development
ATTN: CRD/M
Department of the Army
Washington, D.C. 20310

Commanding Officer
U.S. Army Combat Dev Command
Communications-Electronics Agency
Fort Monmouth, N.J. 07703

Commander
U.S. Army Research Office (Durham)
Box CM - Duke Station
Durham, N.C. 27706

Commanding Officer
U.S. Army Sec Agcy Comb Dev Actv
Arlington Hall Station
Arlington, Virginia 22212

U.S. Army Security Agency
ATTN: OAC of S, Dev
Arlington Hall Station
Arlington, Virginia 22212

U.S. Army Security Agcy Proc Cen
ATTN: IAVAPC-R&D
Vint Hill Farms Station
Warrenton, Virginia 22186

Technical Support Directorate
ATTN: Technical Library
Bldg 3330, Edgewood Arsenal
Maryland 21010

(2) Commanding Officer
U.S. Army Nuclear Defense Lab
ATTN: Library
Edgewood Arsenal, Md. 21010

Harry Diamond Laboratories
ATTN: Library
Connecticut Ave & Van Ness St
Washington, D.C. 20438

Commandant
U.S. Army Air Defense School
ATTN: C&S Dept, MSL Sci Div
Fort Bliss, Texas 79916

Commander, U.S. Army Garrison
ATTN: Technical Reference Div
Fort Huachuca, Arizona 85613

Commanding General
U.S. Army Munitions Command
ATTN: AMSMU-RE-R
Dover, N.J. 07801

(3) Commanding General
U.S. Army Test & Eval Command
ATTN: AMSTE-EL, -FA, -NBC
Aberdeen Proving Ground, Md. 21005

Commanding Officer
U.S. Army Terrestrial Sciences Center
ATTN: Library
Hanover, New Hampshire 03755

Commanding General
U.S. Army Natick Laboratories
ATTN: AMXRE-EG
Natick, Mass. 01760

(2) Commanding Officer
U.S. Army Ballistic Research Labs
ATTN: AMXBR-B & AMXBR-IA
Aberdeen Proving Ground, Md. 21005

(2) Director
U.S. Army Engr Waterways Exp Sta
ATTN: Research Center Library
Vicksburg, Miss. 39180

Director
U.S. Army Munitions Command
Operations Research Group
Edgewood Arsenal, Md. 21010

Commanding Officer
Frankford Arsenal, Bldg. 201-1
ATTN: SMUFA-N3200
Philadelphia, Pa. 19137

Commanding Officer
U.S. Army Picatinny Arsenal
ATTN: SMUPA-TVI
Dover, N.J. 07801

Commanding Officer
U.S. Army Dugway Proving Ground
ATTN: Meteorology Division
Dugway, Utah 84022

President
U.S. Army Artillery Board
Fort Sill, Oklahoma 73503

Commanding Officer
U.S. Army Combat Dev Comd
Artillery Agency
Fort Sill, Oklahoma 73503

Commandant
U.S. Army Artillery & Missile School
ATTN: Target Acquisition Dept
Fort Sill, Oklahoma 73504

Chief, AM & EW Division
ATTN: USALPG-STEEP-TD
Fort Huachuca, Arizona 85613

Commandant
U.S. Army Chemical Cen & School
Micrometeorological Section
Fort McClellan, Alabama 36201

Commandant
U.S. Army Signal School
ATTN: Meteorological Dept
Fort Monmouth, N.J. 07703

Asst Ch of Staff for Force Dev
CBR Nuclear Operations Dir
Department of the Army
Washington, D.C. 20310

Asst Secretary of the Army (R&D)
Department of the Army
ATTN: Deputy Asst for Army R&D
Washington, D.C. 20315

Commanding Officer
U.S. Army Limited Warfare Lab
Aberdeen Proving Ground, Md. 21005

Ch, Special Techniques Div
Unconventional Warfare Dept
U.S. Army Special Warfare School
Fort Bragg, N.C. 28307

Commanding Officer
U.S. Army Biological Labs
ATTN: CB Cloud Research Office
Fort Detrick, Frederick, Md. 21701

Commanding Officer
U.S. Army Biological Labs
ATTN: Tech Library, SMUFD-12 TL
Fort Detrick, Frederick, Md. 21701

Commanding Officer
U.S. Army CBR Oper Research Grp
Army Chemical Center, Md. 21401

Commanding Officer
U.S. Army Chemical R&D Labs
ATTN: Dir, Development Support
Army Chemical Center, Md. 21401

Commanding General
U.S. Army Materiel Command
ATTN:AMCRD-RS-ES-A
Washington, D.C. 20315

Commanding General
U.S. Army Materiel Command
ATTN: AMCRD-DE-MI
Washington, D.C. 20315

Commanding Officer
U.S. Army Transportation Res Cmd
Fort Eustis, Virginia 23604

President
U.S. Army Arctic Test Board
Ft Greely, Delta Junction, Alaska
99737

Headquarters
U.S. Army Supply & Maintenancd Cmd
Dover, N.J. 07801

Commanding General
U.S. Army CDC
Combined Arms Group
Fort Leavenworth, Kansas 66027

Commanding General
U.S. Army Combat Developments Cmd
Combat Support Group
Fort Belvoir, Virginia 22060

Commanding General
U.S. Army Munitions Command
ATTN: AMSMU-RE-4
Dover, N.J. 07801

Commanding General
U.S. Army Test & Eval Comd
ATTN: NBC Directorate
Aberdeen Proving Ground, Md. 21005

Commanding General
U.S. Army Natick Labs
ATTN: Earth Sciences Div
Natick, Mass. 01762

Commanding General
Deseret Test Center
ATTN: Design & Analysis Div
Fort Douglas, Utah 84113

Commanding General
Fort Detrick
ATTN: Environmental Analysis Ofc
Frederick, Md. 21701

CG, U.S. Army Electronics Cmd
ATTN: AMSEL-MR
225 South 18th St
Philadelphia, Pa. 19103

Headquarters
U.S. Army Combat Dev Comd
ATTN: CDCLN-EL
Fort Belvoir, Virginia 22060

USAECOM Liaison Officer
MIT, Bldg 26, Room 131
77 Massachusetts Ave
Cambridge, Mass. 02139

USAECOM Liaison Officer
Aeronautical Systems Div
ATTN: ASDL-9
Wright-Patterson AFB, O 45433

(20) Ch, Atmos Sci Tech Area
ASL, USAECOM, ATTN: AMSEL-BL-RD
Fort Huachuca, Arizona 85613

Ch, Atmos Sci Office
Atmos Sci Lab
U.S. Army Electronics Command
White Sands Msl Range, N.M. 88002

(14) Commanding General
U.S. Army Electronics Cmd
Fort Monmouth, N.J. 07703

ATTN: AMSEL-EW
AMSEL-PP
AMSEL-10-T
AMSEL-RD-MAT
AMSEL-RD-LNA
AMSEL-XL-D
AMSEL-WL-D
AMSEL-NL-D
AMSEL-KL-D
AMSEL-VL-D
(3) AMSEL-HL-CT-D
AMSEL-SC
AMSEL-RD-D
AMSEL-RD-LNF

(2) NASA Scientific & Tech Info Fac
ATTN: Acquisitions Br (S-AK/DL)
P.O. Box 33
College Park, Md 20740

(2) DASA Info & Analysis Center
General Electric - Tempo
816 State St
Santa Barbara, Calif. 93102

Institute of Science & Technology
University of Michigan
P.O. Box 618 (IRIA Library)
Ann Arbor, Mich. 48107

Vela Seismic Info Center
University of Michigan
P.O. Box 618
Ann Arbor, Mich. 48107

Battelle - Defender Info Center
Battelle Memorial Institute
505 King Ave
Columbus, O. 43201

Library of Congress
ATTN: Exchange & Gift Div
Washington, D.C. 20540

Head, Atmos Sciences Section
National Science Foundation
1800 G Street, N.W.
Washington, D.C. 20550

Director
Bureau of Research & Development
Federal Aviation Agency
Washington, D.C. 20553

Chief, Fallout Studies Branch
Division of Biology & Medicine
Atomic Energy Commission
Washington, D.C. 20545

NASA Headquarters
Meteorology & Soundings Br (Code SAM)
Atmospheric Sciences Library
Environmental Sci Svsc Admin
Silver Springs, Md. 20910

Air Resources Field Research Office
& National Center Air Pollution Con
4676 Columbia Parkway
Cincinnati, O. 45226

Director
Atmos Physics & Chemistry Lab R31
ESSA - Dept of Commerce
Boulder, Colorado 80302

Natl Cen for Atmos Research
NCAR Library, Acquisitions - Reports
Boulder, Colorado 80302

OCE, Bureau of Reclamation
ATTN: D755 Bldg. 67
Denver, Colorado 80225

Dir of Meteorological Systems
Office of Applications (FM)
Natl Aero & Space Admin
Washington, D.C. 20546

Director
U.S. Weather Bureau - ESSA
ATTN: Librarian
Washington, D.C. 20235

Director, Meteorology Dept
University of Arizona
Tucson, Arizona 85717

Dept of Water Science & Engr
ATTN: Mr. W. O. Pruitt
University of California
Davis, California 95616

Dept. of Agr Engr
ATTN: Mr. W. B. Goddard
University of California
Davis, California 95616

Meteorology Department
San Jose State College
San Jose, California 95113

Chief, Radio Prop Lab
National Bureau of Standards
Boulder, Colorado 80301

Dept of Civil Engineering
ATTN: Dr. J. E. Cernak
Colorado State University
Fort Collins, Colorado 80521

Forest Service Exp Sta
ATTN: Mr. M. Martineili
Rm 221 Forestry Bldg, CSU
Fort Collins, Colorado 80521

Director, Meteorology Dept
Florida State University
Tallahassee, Florida 32301

Meteorology Dept
University of Hawaii
Honolulu, Hawaii 96822

Rosenwald Library
Meteorology Collection
University of Chicago
1101 E 58th St
Chicago, Ill 60637

Dept of Agronomy
ATTN: Dr. R. H. Shaw
Iowa State University
Ames, Iowa 50010

Director, Soil & Water Cons
Res Div, ARS-USDA
Beltsville, Md. 20705

Director
Dept of Civil Engr
Johns Hopkins University
Baltimore, Md 21233

Director, Meteorology Dept
Massachusetts Inst of Technology
Cambridge, Mass. 02138

ESSA - Weather Bureau
Techniques Development Lab
Silver Spring, Md. 20910

Director, Meteorology Dept
St. Louis University
St. Louis, Missouri 63120

Dept of Soils
University of Missouri
Columbia, Missouri 62501

Dept. of Geophysics
Washington University
St. Louis, Missouri 63120

Director, Meteorology Dept
New York University
University Heights
New York, N.Y. 10001

Microclimate Investigations
SWC-ARS-USDA
Bradfield Hall, Cornell Univ
Ithaca, N.Y. 14850

Director
Meteorology Department
Pennsylvania State University
University Park, Pa 16802

Dept of Oceanography & Meteorology
Texas A&M University
College Station, Tex. 77840

Dept of Meteorology
University of Utah
Salt Lake City, Utah 84116

Director, National Research Council
National Academy of Sciences
2101 Constitution Ave.
Washington, D.C. 20315

Dr. J. A. Businger
Meteorology Department
University of Washington
Seattle, Wash. 99703

Director
Meteorology Department
University of Wisconsin
Madison, Wis. 53705

Officer-in-Charge
Meteorology Curriculum
US Naval Postgraduate School
Monterey, Calif. 92801

Department of Soils
University of Wisconsin
ATTN: Cϵ Bϵ Tanner
Madison, Wis 53705

Director, Geophysical Res
USAF Cambridge Res Center
ATTN: CRZHB (Hanscom Field)
Bedford, Mass. 01730

Asst Sec for Defense
Office of Sec Defense
ATTN: Geophysical Sciences
Washington, D.C. 20315

USAF Environmental Tech Appl Cen
Bldg 159, Navy Yard Annex
ATTN: IPB
Washington, D.C. 20333

Forestry Library
260 Walter Mulford Hall
University of California
Berkeley, Calif. 94704

Commander
AF Cambridge Research Lab
ATTN: Ch. Boundary Layer Br
Bedford, Mass. 01730

Argonne National Lab
ATTN: Mr. Harry Moses, Met Bldg
9700 S. Cass Ave
Argonne, Ill 60440

Prof. J E Pearson
Gen Engr Dept, Atmos Sci Lab
University of Illinois
Urbana, Ill 61801

Brookhaven National Lab
ATTN: Meteorology Group
Upton, L.I., N.Y. 11973

Director
National Security Agency
ATTN: C3/TDL
Ft George G. Meade, Md 20755

US Naval Ordnance Test Station
CODE 40306
ATTN: Dr. Richard Jackson
China Lake, Calif. 93555

Dr. Kenneth R. Knoerr
School of Forestry
Duke University
Durham, North Carolina 27706

Commander
US Naval Ordnance Test Station
ATTN: CODE 164, Lt Col Clark
China Lake, Calif. 93555

Mr. H. J. Spiegel
So. Connecticut St College
Dept of Sciences
501 Crescent St
New Haven, Conn 06515

Prof. W. E. Reifsnyder
School of Forestry
Marsh Hall, 360 Prospect St
Yale University
New Haven, Conn 06511

Dr. Leo J. Fritschen
College of Forestry
University of Washington
Seattle, Wash. 98105

ARS, Snake River Cons Res Cen
ATTN: Dr. J. L. Wright
Rt 1, Box 186
Kimberly, Idaho 83341

Dr. C. H. M. van Bavel
Institute of Life Sciences
Texas A&M University
College Station, Texas 77843

Dr. Winton Covey
417 State Street
Athens, W.Va. 27412

Dr. Raymond E. Leonard
Northeastern Forest Exp. Sta.
SUNY College of Forestry
Syracuse, N.Y. 13210

Institute for Storm Research
The University of St. Thomas
3812 Montrose
Houston, Texas 77006

Commanding Officer
US Army Biological Lab
ATTN: CB Cloud Res Office
Fort Detrick,Md. 21701

Commanding Officer
US Army CBR Oper Res Gp
Army Chemical Center, Md. 21401

Commanding Officer
US Army Chem R&D Lab
ATTN: Dir of Dev Sup
Army Chemical Center, Md. 21401

Ch, Bureau of Naval Weapons
Code FASS
Dept of the Navy
Washington, D.C. 20315

Commanding Officer
US Army Trans Res Cmd
Fort Eustis, Va. 23604

Commanding General
US Army Materiel Command
ATTN: AMCRD-DE-MI
Washington, D.C. 20315

Commanding General
US Army Materiel Command
ATTN: AMCRD-RS-ES-A
Washington, D.C. 20315

President
US Army Arctic Test Board
Fort Greely, Delta Junction
Alaska 99737

Headquarters
US Army Supply & Maint Cmd
Dover, N.J. 07801

Director
Defense Intelligence Agency
ATTN: DJAAT-IES, DOD
Washington, D.C. 20301

Commanding General, USACDC
Combat Support Group
Fort Belvoir, Va. 22060

Commanding General
US Army CDC
Combined Arms Group
Fort Leavenworth, Kansas 66027

Dr. Craig Crenshaw
USAMC Headquarters
ATTN: AMCSAS
Washington, D.C. 20315

Commanding Officer
US Army Biological Lab
ATTN: Technical Library, SMUFD-12 TL
Fort Detrick, Md. 21701

Fresno State College
Atmospheric Water Resources Research
ATTN: Mr. Merlin C. Williams
5302 N. Fresno St.
Fresno, Calif. 93726

Dr. E. P. Van Arsdel
College of Agriculture — Plant Sci Dept
Texas A&M University
College Station, Texas 77843

Director, Meteorology Dept
University of California
Los Angeles, Calif. 90052

Commanding Officer
U.S. Army Biological Lab
ATTN: K. L. Calder
Fort Detrick, Frederick, Md. 21701

Director
Environmental Biology Program
National Science Foundation
Washington, D.C. 20550

Commanding General
CDC Experimental Center
Fort Ord, California 93941

Director
U.S. Water Conservation Lab
4331 E. Broadway
Phoenix, Arizona 85040

Director
Pacific SW Forest & Range Exp Sta
Box 245
Berkeley, California 94701

Scientific Research Institute
Oregon State University
ATTN: Atmospheric Science Br
Corvallis, Oregon 97330